SnO_2 thick film sensors at ultimate limits: Performance at low O_2 and H_2O concentrations; Size reduction by CMOS technology

An den Grenzen von SnO_2 Dickschichtsensoren: Leistungsfähigkeit in geringen O_2 und H_2O Konzentrationen; Miniaturisierung durch CMOS-Technologie

DISSERTATION

der Fakultät für Chemie und Pharmazie der Eberhard-Karls-Universität Tübingen

zur Erlangung des Grades eines Doktors der Naturwissenschaften

2002

vorgelegt von
SIMONE HAHN

Tag der mündlichen Prüfung: 1. August 2002-08-12

Dekan: Prof. Dr. H. Probst

1. Berichterstatter: PD. Dr. U. Weimar

2. Berichterstatter: Prof. Dr. G. Gauglitz

Meinen Eltern

„Ducunt volentem fata, nolentem trahunt."

Den Willigen führt das Geschick, den Störrischen schleift es mit.

4. Jh. v. Chr., in Anlehnung an Kleanthes

Table of contents

Symbols

α	number of ionised forms
β	=1 atomic form, > 1 molecular form
ε	dielectrical constant
μ	chemical potential
μ_B	(hall) mobility of bulk electrones
λ_D	debeye length
σ	conductivity
σ_b	bulk conductivity
$[x]$	concentration of a atom/molecule
A	area
abs.h.	absolute humidity
d	thickness
e	vapour pressure
e^-	electron
E_C	energy of conduction band
E_D	energy of donor levels
E_F	energy of fermi level
E_G	energy of the band gab
E_S	saturation pressure
E_{SS}	energy of surface state
eV	electron volt, 1 eV = $1.6022 \cdot 10^{-19}$J
E_w	partial pressure of water
E_{ws}	saturation water pressure
G	conductance
k	Boltzmann constant
k_x	rate constant of reaction
l	length
n	number of moles
nd	optical thickness
n_S	number of electrodes in the surface layer
$O^{-\alpha}$	chemisorped oxygen species

p	absolute pressure
p_a	partial pressure of component a
ppm	parts per million (10^{-6})
ppm_V	parts per million by volume
P_{tot}	total pressure of a mixture
p_x	partial pressure
R	radius
R	universal gas constant
R	resistance
R_C	contact resistance
r.h.	relative humidity
S	unoccupied chemisorption site
T	(absolute) temperature
U	voltage
V	volume
V_S	surface band bending
w.t.	weight
X^{ad}	adsorbed gas atom/molecule
X^{gas}	atom/molecule in gaseous phase
z_o	thickness of depletion layer

Abbreviations

AC	Alternating Current
AMS	Austria Mikro Systeme, Unterpremstatten, Austria
ANN	Artificial Neural Network
CEM	Controlled Evaporation and Mixing
CMOS	Complementary Metal Oxide Semiconductor
CP	Conductive Polymer
CVD	Chemical Vapour Deposition
DC	Direct Current
DOS	Density of States
DRIE	Deep Reactive Ion Etching
DRIFT	Diffuse Reflectance Infrared Fourier Transform Spectroscopy
EMF	ElectroMotive Force
EPR	Electron Paramagnetic Resonance spectroscopy
ESR	Electron Spin Resonance spectroscopy
FIS	Fuzzy Inference Systems
FTIR	Fourier Transformed Infrared spectroscopy
FWHM	Full Width Half Maximum
GC	Gas Chromatography
HC	Hdrocarbon
IC	Integrated Circuitry
IMT	Institute for Microtechnology
IPC	Institute of Physical Chemistry at the University of Tübingen
IR	Infrared Spectroscopy
ISFET	Ion-Conduction
LEL	Low Explotation Limit
LMFC	Liquid Mass Flow Controler
LPCVD	Low Pressure Chemical Vapour Deposition
MAK	Maximale Arbeitsplatz Konzentration
MEMS	Micro Electrical Mechanical Structure
MFC	Mass Flow Controller
MLR	Multivariate Linear Regression
MOSFET	Metal Oxide Field Effect Transistor

MOX	Metal Oxide Sensor
MS	Mass Spectrometry
NIST	National Institute of Standards and Technology
PC	Principal Component
PCA	Principle Component Analysis
PCR	Principle Component Regression
PEL	Permissible Exposure Limit
PLS	Partial Least Squares
PVD	Physical Vapour Deposition
QCM	Quartz Cyrstal Microbalance
RGTO	Rheotaxial Growth and Thermal Oxidation
RMS	Root Mean Square error
SAW	Surface Acoustic Wave
SC	Semiconductor
SIMS	Secondary Ion Mass Spectroscopy
STM	Scanning Tunnel Microscopy
TEM	Transmission Electron Microscopy
TLM	Transmission Line Measurement
TPD	Temperature Programmed Desorption spectroscopy
UPS	UV Photo Spectroscopy
XAS	X-ray Adsorption Spectroscopy
XPS	X-ray Photo Spectroscopy

1 Introduction and Motivation

1.1 Introduction

Gas sensors are devices, which allow for the determination of information about the ambient gas atmosphere, consisting of a sensitive layer and a signal transfer component the so-called transducer. The former is optimised by a proper choice of materials, the latter by a suitable technology. The gas detection is based on the fact that changes in the gaseous atmosphere alter the properties of the sensing layer in a characteristic way, which is transformed in a signal by the transducer. In case of optical sensors, changes in the ambient atmosphere change the sensor's optical properties e.g. optical thickness Δnd or adsorption $\Delta\epsilon$, which are measured by interferometers, optical wave-guides, fibres, etc. Capacitive sensors respond by capacitance changes of the material, which are mostly detected through low frequency AC measurements - the choice by monitoring compounds with high dielectric constant like water. In the case of mass sensitive sensors (e.g. Quartz Micro Balances QMBs, Surface Acoustic Wave sensor SAWs), the composition of the gas atmosphere affects the mass and thus, oscillating frequency which is used as transducer. Conductance sensors (e.g. Metal OXide MOX sensors, Conductive Polymer sensors CP, ionic conductors) respond with changes in resistance, which is normally determined by a 2- or 4-point resistance measurement. Figure 1 shows a selection of the different types of sensor.
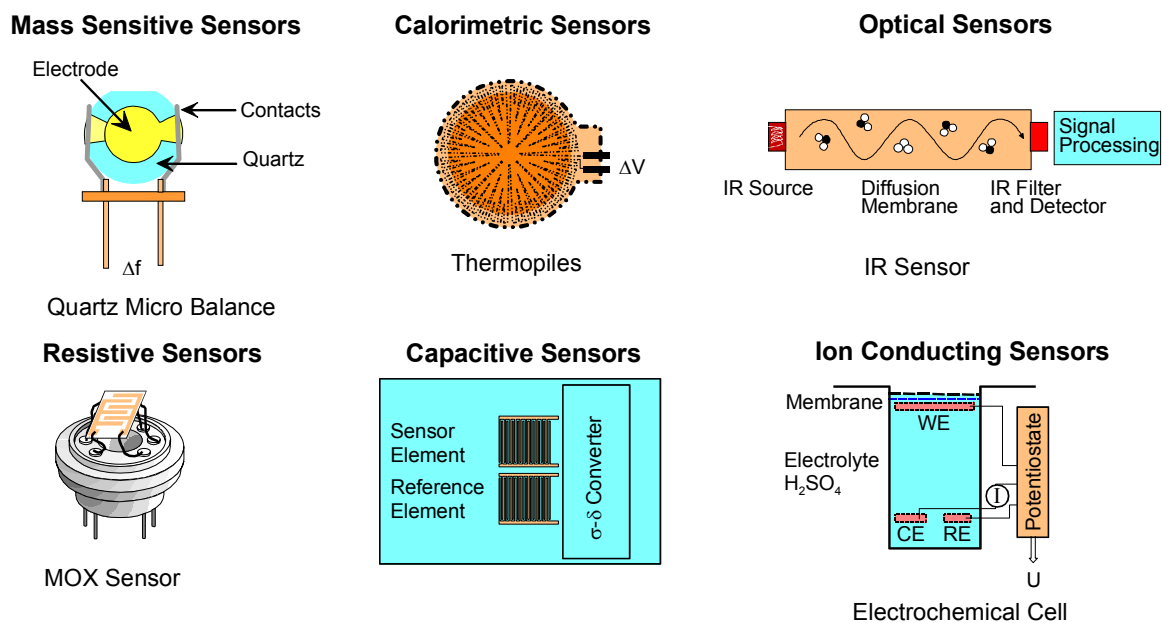
Figure 1: A selection of available gas sensor types.

The sensing principles are illustrated in Figure 2 (for details see the figure caption).
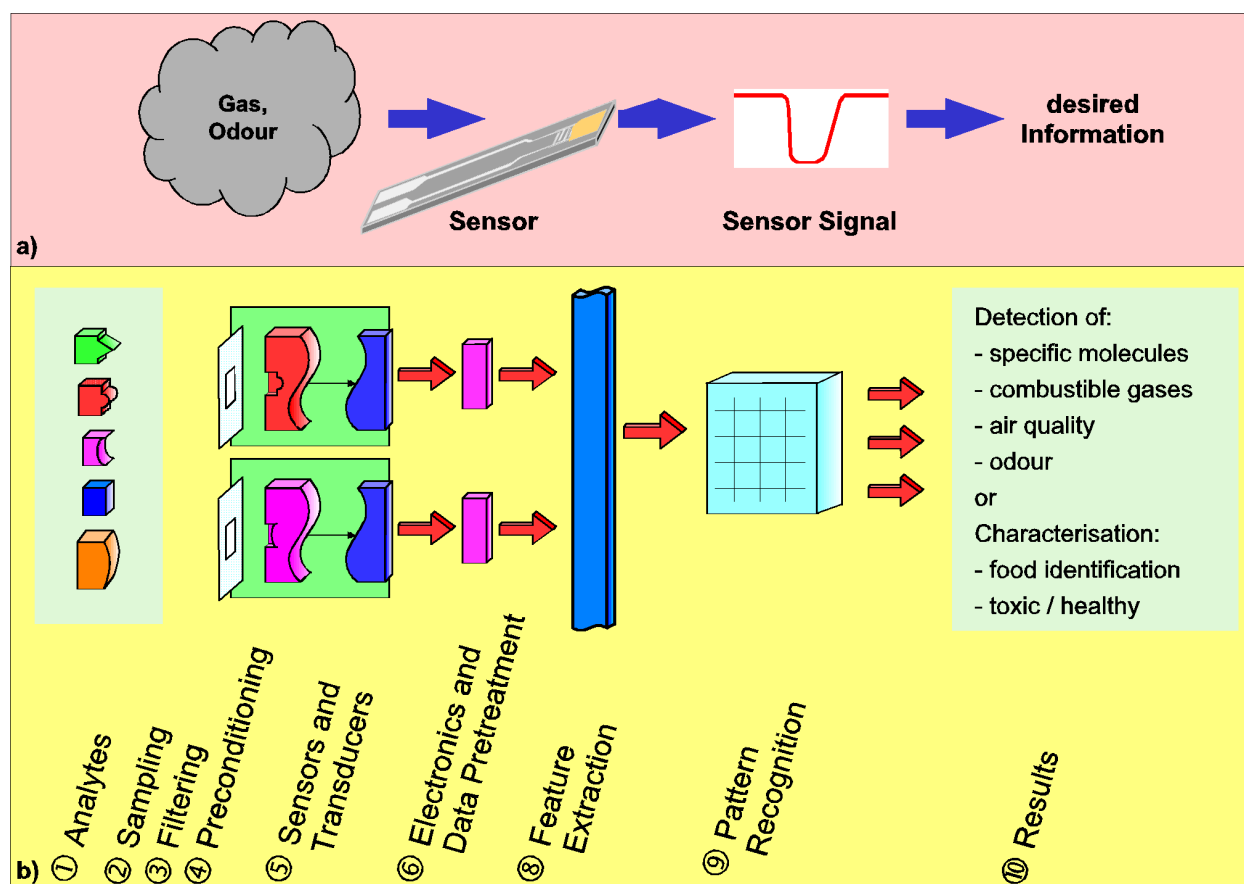
Figure 2: *Sensing principle. a) Simple model: A change in the ambient gaseous atmosphere changes the sensor properties in a characteristic way. The sensor signal obtained can be used to obtain the information desired. b) More realistic model: The gas detection unit is exposed to a complex gas mixture. After sampling, some of the analytes can be selected by a filter, and subsequent to an optional preconditioning of the sample; the remaining gases are exposed to the sensor(s). Here some of the gas types will trigger a characteristic change in the sensor properties. The transducer(s) transform these changes into electronic signals. The data obtained can then be processed and the characteristic features can be extracted. Depending on the application, a more or less sophisticated pattern recognition may follow in order to gain the information required.*

Gas sensors are used to detect gases, to discriminate odours or generally to monitor changes in the ambient gas atmosphere. At present, the number of potential applications for gas sensors or gas sensor systems is huge. Gas sensors or devices based on gas sensors cover applications ranging from high volume (e.g. control of car ventilation) to small volume products (e.g. stand-alone multi-function tools, often referred to as 'electronic noses').

The sensors are not the only means of gas detection or more general analysis of gas mixtures. The composition of gas mixtures can also be measured precisely by means of analytical tools such as GC (Gas Chromatography), MS (Mass Spectrometry), FTIR (Fourier Transform Infrared Spectroscopy) or by a combination of these. These tools are all expensive and not so easy to operate. Moreover, for many applications, the complete set of data a sophisticated

analytical tool offers is not needed. In such cases gas sensors or systems based on gas sensors have proven to be a usable alternative.

Among gas sensors, semiconducting MOX sensor are important due to their variety of sensitive material and preparation methods. The fact that they are heated makes them less dependent on ambient temperatures and reduces poisoning. However, the power consumption has to be reduced as much as possible to be able to operate them by batteries and thus open up applications. The resistance change of the sensitive material is typically measured with a 2-, 3- or 4-point electrode.

The sensors investigated in this work are semiconducting SnO_2 thick film gas sensors. A typical semiconducting SnO_2 sensor consists - in a simplest design - of substrate provided with heater and electrodes and a sensitive layer in contact with the electrodes (see Figure 19 in chapter 3.1.2.1).

Some advantages of the actual SnO_2 sensors are [Iho94]:

- Long operating life and reasonable parameter stability.
- High reliability (in part because of the very simple associated electronics) leading to a low failure rate.
- Good resistance to corrosive gases.
- Robust construction and good mechanical strength.
- Inherently low cost (including the electronics), small and easy to handle.
- Little maintenance.

There are also disadvantage like:

- Poor selectivity of single sensors.
- Influence of ambient humidity.
- Long stabilizing time after energisation.
- Large power consumption (compared with electrochemical cells or ionisation-type smoke detectors, for example).

There is a need to overcome these limitations and a lot of work was performed in the last years to handle these disadvantages. Some are also topic of this thesis. In the case of the first two items, the poor selectivity can be overcome by using sensor arrays or selecting appropriate materials (treatment, manufacturing), additives and/or carefully choice the working temperatures or the use temperature cycling.

Developing technical reproducible fabrication methods and using miniaturized sensors will clear the latter disadvantages.

1.2 Motivation

Tin dioxide (SnO_2) is widely used as material for gas sensors. Therefore, besides titanium dioxide (TiO_2) it is one of the best-investigated materials. Many of the papers deal with the physical and electrical properties of pure or doped – mainly Pd and Pt - SnO_2 that is partly characterised with vacuum technologies like SIMS (Secondary Ion Mass Spectroscopy), TEM (Transmission Electron Microscopy), STM (Scanning Tunnel Microscopy), XPS (X-ray Photoelectron Spectroscopy), etc. Although reactions like oxygen (O_2) adsorption have been studied with these techniques, their results cannot be transferred easily to real operation conditions. In real-life conditions, SnO_2 sensors were investigated by DC-, AC-, work function- and consumption measurement, IR (InfraRed)-, DRIFT spectroscopy (Diffuse Reflectance Infrared Fourier Transform spectroscopy) – to name only some.

The best-investigated molecules reactions with $SnO2$ sensors are oxygen (O_2), water (H_2O), carbon monoxide (CO), methane (CH_4) and nitrogen oxides (NO_x). The adsorption process and the resulting adsorbed species of O_2 and H_2O, because of their presence in most cases, play an important role in the sensing mechanisms of SnO_2 sensors. Temperature Programmed Desorption measurements (TPD) showed that oxygen adsorption results in temperature-dependent ionosorbed species (O_2^-, O^{2-} and O^-), with O^- dominating in the range of interest (250 to 400°C, chapter 2.2.1). Water adsorption results in the formation of hydroxyl groups bound to Sn atoms forming strong surface dipoles hence leading to changes in the electron affinity (chapter 2.2.2).

The reaction of SnO_2, in air with different test gases is relatively extensively studied. Generally CO, CH_4 and NO_x are the most used gases to characterise the performance of the sensors, because of their different sensing mechanisms. CO and CH_4 introduce electrons in the conduction band (decrease of sensor resistance) by reacting with the SnO_2 surface, whereas NO_x removes electrons and increase the sensor resistance. It was shown that the resistance of Pd/Pt doped and undoped sensors decreases, in air, in the presence of humidity and of reducing gases. With different sensor preparation methods and at different operation temperatures it is possible to control the sensitivity to a certain extent [Kap01].

All the mentioned investigations were performed in vacuum or real live condition, which imply synthetic air as carrier gas and relative humidities ranging from 0 up to 80%. Some measurements have been carried out at low oxygen concentrations with the purpose of identifying the oxygen species adsorbed at the sensor surface [Nan82]. There are only few papers dealing with sensing mechanism in low oxygen concentrations [Tou99] (see chapter 2.2.1).

Despite of some investigations with spectroscopic techniques like Mössbauer spectroscopy [Saf02] very little is known about the sensor performance in the absence of oxygen [Car00]. Oxygen is seen to be crucial for the reaction but up to now its role at low concentration was not individually studied in working condition. This is an interesting problem because the general assumption is that a chemical conversion with oxygen species takes place at the semiconductor sensor surface.

The first part of this thesis is dedicated to the reaction of doped and undoped SnO_2 thick film sensors with different test gases in the absence or at low O_2 and H_2O concentration. The O_2 was varied in small ppm rang and low % range. The humidity was ranging from ppm up to 10% absolute humidity. Both, O_2 and H_2O were monitored online. CO and propane (C_3H_8) were chosen as test gases. CO is one the best-investigated compound on SnO_2 surfaces and it is generally used to characterize the sensor performance. A hydrocarbon (HC) as second test gas is interesting to study in oxygen dependent condition because of the different sensing mechanism when compared to CO. From CH_4 it is known that the dependence of the sensing on humidity is the opposite of the one corresponding to CO. Normally methane (CH_4) is selected, as a typical hydrocarbon, but in this thesis propane (C_3H_8) was used because it plays an important role in the automotive exhaust, where one finds the above-mentioned conditions of low oxygen concentrations and high humidities.

Up to now there are only a small number of HC-sensors available to monitor the amount of hydrocarbons in the exhaust. One sensor on the market is produced by Bosch and consists of a Au/Pt alloy fabricated in multi-layer ceramic technology (Figure 3).
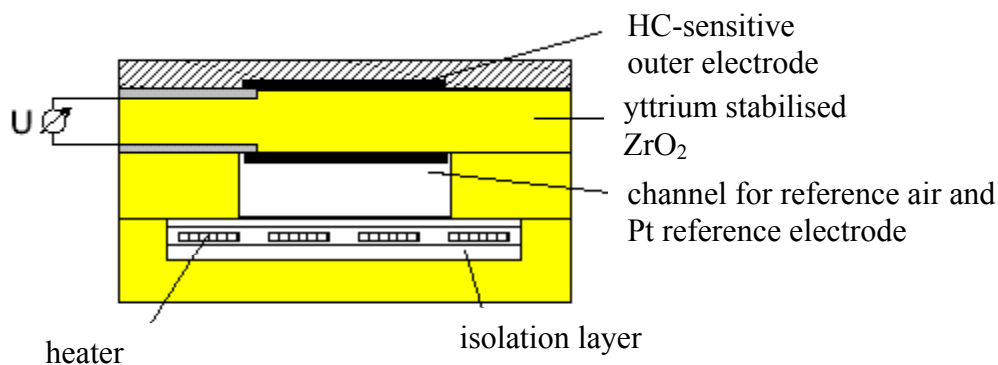
Figure 3: Schematic representation of a profile of a sensor element fabricated in a multi-layer ceramic technology which is fabricated by Bosch [Mos00].

The set-up corresponds to the one of the λ-probe, as the potential is measured compared to reference air. At an operating temperature of 530°C, the sensor is very sensitive to unsaturated

hydrocarbons but for saturated hydrocarbons, no sensitivity was found. Additionally, cross sensitivities were found to H_2, CO and the partial pressure of O_2.

The aim of the study is to find out if a SnO_2 thick film sensor is able to detect CO and C_3H_8 in the absence of O_2 and H_2O and how do changing O_2 concentration, temperature and humidity influence the sensing. With this information, sensing mechanism for these conditions can be derived. The knowledge about the sensing mechanism will help to develop a sensor or a sensor array that is able to detect and quantify hydrocarbons in the background of CO in exhaust like conditions.

The second part of this work is dealing with an application of classical chemical sensors, id est undoped and Pd/Pt doped SnO_2 thick films on alumina substrates. This type of sensors has been chosen because of their proven reliability and high sensitivity. The application is domestic one dealing with natural gas heating systems. In the case of gas-operated burners, one faces two serious problems: leakages and incomplete burning of the natural gas. The first results in an increasing methane concentration (danger of explosion) and the second in an increasing CO concentration (danger of intoxication). The maximum allowed gas concentration at work places in Germany (PEL[1]/MAK[2]) is 30mg / m^3 CO [Röm95]. For CH_4, explosive mixtures are in the range of 5 - 15% CH_4.

The aim is to solve the above-mentioned problems an instrument that is preferably low cost, small size and at best has a low power consumption. In Table 1 some commercial available leakage detection instruments are listed. The detection principle, detection limit, size and price are specified if available.

---

[1] PEL: Permissible Exposure Limit

[2] MAK: Maximale Arbeitsplatz Konzentration

Table 1: Selection of commercial available leakage detectors.

	Detection limit	Detection principle	Size/Price
Tokyo Gas Co.,Ltd. [Tok]	50 - 200 ppm	semiconductor sensor + charcoal filter	$(125 \times 85 \times 54)$ mm^3 450g
Innova™ Stand. Thermo Gas Tech [The]	CO 0 - 300 ppm CH$_4$ 0 – 10 000 ppm Resolution 5%	CH$_4$ thermal conductivity CO electrochemically	$(254 \times 152 \times 127)$ mm^3 2.25kg $ 1400
LD2 [War]	5 ppm CO	1 semiconductor sensor	$(50 \times 63 \times 35)$ mm^3 + probe, 254g $ 240
General Monitors [GM]	Methane, propane 0-100%	Infrared Point sensor	61.5 x 21.5 mm 1.4kg
Primatech [Pri] ESM-1279	1/10 - 1/4 L.E.L.[1]	Semiconductor sensor	$(140 \times 85 \times 38)$ mm^3 $ 450
Kane Int. Ltd. CD100A [Kan]	50 ppm (methan) not selective	low power semi-conductor sensor	$(100 \times 205 \times 36)$ mm^3, 460g
RKI Intruments Eagle [RKI]	0 - 50000ppm CH$_4$ CO$_2$ 5 ppm resolution	IR sensor	$(10.5 \times 5.9 \times 7)$ inch^3

As shown in Table 1 the most used detection principle for leakage detectors are semiconductor sensors and infrared sensors. Some of the instruments measure CO by electrochemical cells and CH$_4$ by its thermal conductivity. Electrochemical cells offer a great selectivity and stability but they are expensive. For monitoring CH$_4$ at the same time another type of sensor (here thermal conductivity sensors) is needed which increases the instrument size, configuration and ultimately the costs. Infrared systems suffer on large size, sophisticated equipment and their high costs. The choice for low cost systems is clearly the use of semiconductor sensors. Unfortunately, some systems are equipped only with one sensor, which makes the instruments vulnerable to changing humidity backgrounds or interfering gases. These can cause false alarm. Additionally, it is desired that the sensor indicate the kind of problem occurred – leakage or incomplete burning – to facilitate the repair. To solve these problems one has to use a sensor arrays to get different patterns for the different mixtures of the single compounds.

One is also interested in the very end of the function of SnO$_2$ tick film sensors. In order to simulate the situation different mixtures of CO and CH$_4$ in changing humidity background (0

---

[1] Lower explosive limit

– 50% relative humidity) were measured by a sensor array of differently doped and undoped SnO_2 thick film sensors. For evaluating the data, multivariate data analysis has to be used. In this work, the evaluation was performed with Principle Component Analysis/Regression (PCA/PCR) and Fuzzy Inference Systems (FIS).

The third part of experimental results will deal with the sensor performance of newly developed micromachined sensors. At the moment, most of the commercial available sensors are manufactured in screen-printing technique on small and thin ceramic substrates [Fig00] [FIS99] [UST99]. The screen-printing technique has the advantage that thick-films of metal oxide semiconductor sensors are deposited in batch processing thus leading to a small sensor-to-sensor distribution within production lots. This technology is nowadays well established and high performance of screen-printed ceramic sensors is achieved in various application fields.

The classical screen-printed ceramic gas sensors used are, with respect to the power consumption, mounting technology and selectivity still in need of improvement. The power consumption of screen-printed devices is typically in the range of 200 mW to about 1 W. That is too much for applications, which ask for the use of battery-driven elements. The mounting of the overall hot ceramic element is difficult. One has to find designs that ensure good thermal isolation between sensor elements and housing as well as high mechanical stability. Good thermal isolation is thereby not only needed to minimize the overall power consumption but also to enable the integration of signal processing electronics in the same housing. The above-mentioned difficulties lead to integration of gas sensitive metal oxide layers in standard microelectronic processing.

Microstructured sensors developed at the University of Warwick and the Institute of Physical Chemistry (IPC) at the University of Tübingen and produced at the Institute of Microtechnology (IMT) Neuchâtel (Switzerland) were well investigated at IPC. Some papers and doctoral thesis deal with the production [Sim01] and sensor performance [Cap01]. The schematic layout of IPC/IMT microsensors is shown in Figure 4 [Bri99], [Hei97].

cross section: **top view:**
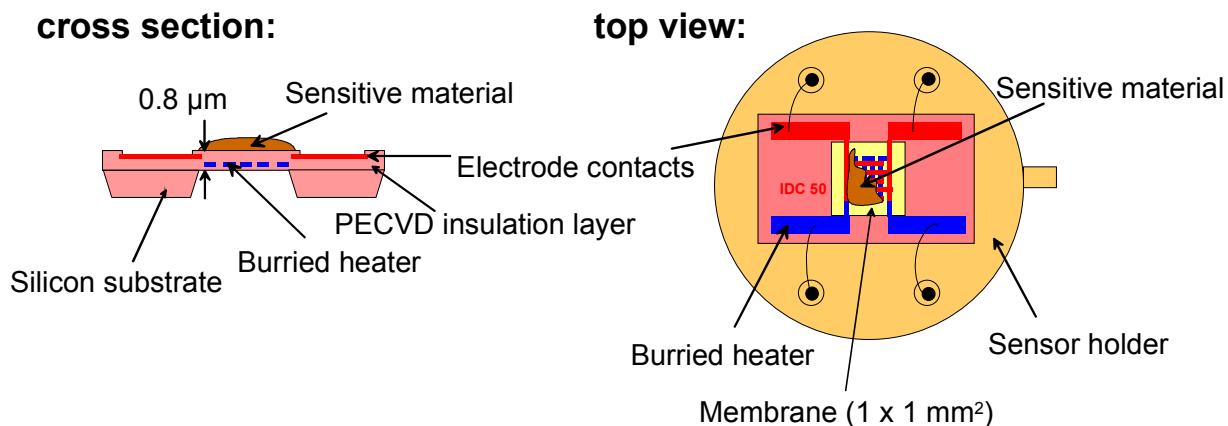
Figure 4: Schematic of IPC/IMT microsensor. The sensitive film was deposited by drop deposition onto the micromachined substrate. The membrane consists of stress-free LPCVD silicon nitride and platinum as heater and electrode material [Bri99], [Hei97].

The IPC/IMT microsensors face one major drawback: they are non CMOS (Complementary Metal Oxide Semiconductor) technology and therefore electronics can only implemented in a post-processing step, which brings in an additional costs and transportability issues.

CMOS technology has become by far the predominant fabrication technology for Integrated Circuits (IC). The production of microsensors by CMOS technology will benefit from well-established fabrication technologies and the possibility of on-chip circuitry. In these devices, added on-chip functionality can be implemented, such as calibration by digital programming, self-testing, and digital interfaces.

During the elaboration of this thesis a CMOS technology-based microsensor was developed in cooperation with the Eidgenössische Technische Hochschule Zürich (ETHZ) in Switzerland, Austria Mikro Systeme (AMS, Unterpremstatten, Austria) and Applied Sensor/Advanced Sensing Devices (AS/ASD, Germany). The ETH designed the chip layout and electronics, the sensor was fabricated at AMS and IPC/ASD applied the sensing SnO_2 thick film layer. The full characterisation of the sensor was performed at IPC. The new type of microsensor offers small size, low power consumption, low cost mass production, automated coating with the sensitive layer, on chip function tests, electronics for temperature stability, signal conversion and evaluation.

In this thesis, the different designs of the CMOS sensors were tested with regard to sensor performance and stability. With an optimised design of CMOS sensors measurements with different classes of chemical compounds at different humidities and temperatures were carried out to characterise the sensor performance.

2   General aspects of SnO$_2$ gas sensors

This chapter consists of three parts. In the first part, a short paragraph is dedicated to the crystalline and electrical properties of SnO$_2$ to point out the good usability of this material for semiconductor gas sensors.

The second part deals with the interaction of gases at the SnO$_2$ surface. The adsorption of O$_2$ and H$_2$O on the SnO$_2$ surface are discussed. Both compounds are typically present in the measured environment. The interaction of CO, CH$_4$ and propane in the presence of O$_2$ and H$_2$O on the SnO$_2$ surface is also described

Afterwards an overview is given about the different types of SnO$_2$ gas sensors id est thin/thick film sensors and micromachined sensors. Some developments to improve their characteristics will be mentioned. Here one has to discriminate between sensor performance id est sensitivity, stability and the production of sensors. The latter include reproducibility of different production runs and costs.

Experimental work was carried out in conditions (no O$_2$ and H$_2$O) in which gas sensors are normally not operated. To find a way of understanding the reactions taking place a careful monitoring of O$_2$ and H$_2$O is necessary. Therefore, at the end of the chapter, a short review is presented on different O$_2$ and H$_2$O measurement instruments.

2.1   Properties of SnO$_2$

SnO$_2$ has various specific and unique properties, which make this material very useful in many applications. Polycrystalline thin films and ceramics of SnO$_2$ have been extensively used for the production of resistors. Conducting SnO$_2$ films are well known as transparent electrodes, and when deposited on glass it is known as Nesa glass [Rob67]. SnO$_2$ films are also used as transparent heating elements, for the production of transistors, for transparent antistatic coatings and other part in electric equipment where transparency is required.

2.1.1   Crystalline structure of SnO$_2$

SnO$_2$ is an anisotropic polar crystal, which crystallises with tetragonal rutile structure with space group D$_{4h}$ [P4$_2$/mm] [Jar76]. The unit cell contains six atoms, two tin, and four oxygen. Each tin atom is at the centre of six oxygen atoms placed approximately at the corners of a regular slightly deformed octahedron, and three tin atoms approximately at the corners of an equilateral triangle surround every oxygen atom (see Figure 5).
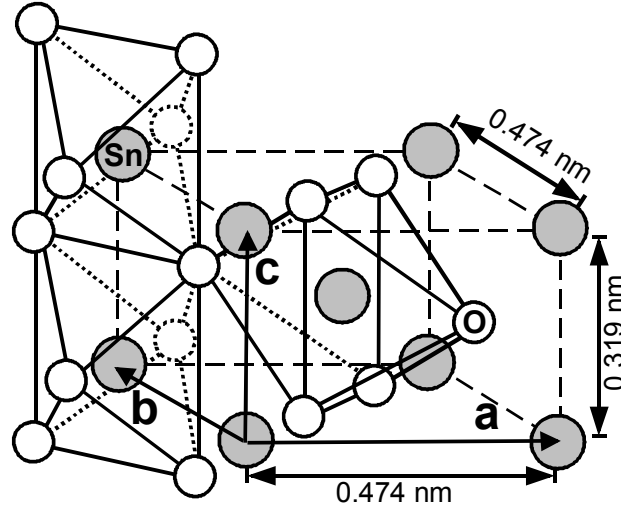
Figure 5: Unit cell of SnO$_2$ with four O^{2-} anions and two Sn^{4+} cations. The crystalline structure of SnO$_2$ is rutile: Each tin atom is at the centre of six oxygen atoms placed approximately at the corners of a regular slightly deformed octahedron, and three tin atoms approximately at the corners of an equilateral triangle surround every oxygen atom

Thus, it is the structure of 6:3 coordination. The lattice parameters are a = b = 4.737 Å and c = 3.185 Å. The c / a ration is 0.673. The ionic radii for O^{2-} and Sn^{4+} are 1.40 and 0.71 Å, respectively. The metal atoms (cations) are located at positions (0,0,0) and (½,½,½) in the unit cell, and the oxygen atoms (anions) at ± (u,u,0) and ± (½+u,½-u,½), where the internal parameter, u, takes the value 0.307. Each cation has two anions at a distance of √2ua (2.053 Å) and four anions at $[2(½-u)^2+(c/2a)^2]^{½}$ a (2.597 Å).

2.1.2 Bulk properties

SnO$_2$ is an n-type, wide-band gap semiconductor. The origin of the n-type behaviour is the native non-stoichiometry caused by oxygen vacancies. The conduction band has its minimum at the Γ point in the Brillouin zone and is a 90% tin s-like state. The valence band consists of a set of three bands (2$^+$, 3$^+$ and 5$^+$). The valence band maximum is a $Γ_3^+$ state. In this way, SnO$_2$ has a direct band gap, with energy $E_{dir}(Γ_{3v}^+-Γ_{1c}^+) = 3.596\ eV$ for $E_\perp$ and *3.99 eV* for $E_{||}$, measured at 4 K. Figure 6 shows the band diagram for SnO$_2$ and the projection of the density of states (DOS) for the 1-states of Sn and O. According to results of Barbarat et al. a large contribution of Sn(s)-states is found at the bottom of the valence band between −7 and −5eV [Bar97]. From −5eV to the top of the valence band, the Sn(p)-states contribution is decreasing, as the Sn(d)-states are occupying the top of the valence band. A large and extended contribution of the O(p)-states is found in the valence band. Clearly, bonding between Sn and O is dominated by the p-states of the latter. Each anion in the unit cell is found to be bonded to the cations in a planar-trigonal configuration in such a way that the

oxygen p orbitals contained in the four-atom plane, i.e., p_x and p_y orbitals, define the bonding plane. Consequently, the oxygen p orbitals perpendicular to the bonding plane, i.e., p_z orbitals, have a non-bonding character and are expected to form the upper valence levels [The92]. The conduction band shows a predominant contribution of Sn(s) states up to 9 eV. For energies larger than 9 eV an equal contribution of Sn- and O-states is found in the conduction band. More information, mainly about the valence band, can be found in [The92][Pad94][Koe95] and references therein.
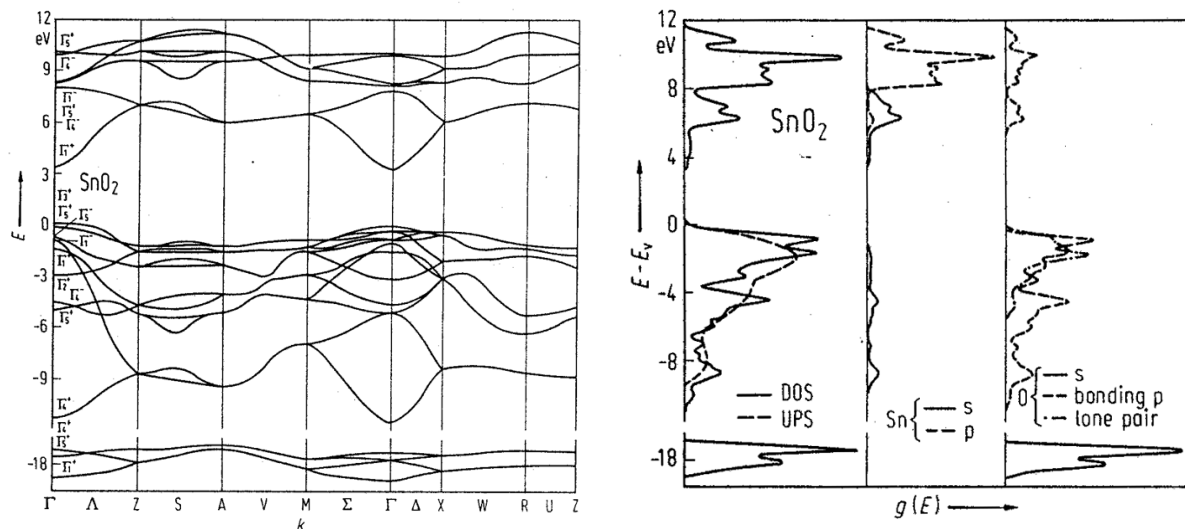
Figure 6: Band diagram of SnO$_2$ (left) and projection of the density of states (DOS) for the 1s states of SnO$_2$, Sn and O (right)[Jol86].

2.1.3 Sensor resistance/conductivity

2.1.3.1 Bulk properties

The conductivity σ_{tot} of a semiconductor crystal can be described as the sum of electronic (σ_e and σ_p) and ionic conductivity (σ_{ion}) if the conduction processes are considered independent. SnO$_2$ gas sensors are typically operated at temperatures between 200°C and 400°C. In this range the ionic contribution can be neglected and the conductivity of SnO$_2$ can be calculated according to:

$$\sigma_{tot} = \sigma_e + \sigma_p + \sum \sigma_{ion,i} \approx \sigma_e + \sigma_p \qquad (1)$$

The resistance of homogeneous bulk material with bulk conductivity σ_b, mobility μ, length l and cross section A can be calculated according to:

$$R_b = \frac{l}{\sigma_b \cdot b \cdot d} = \frac{l}{\sigma_b \cdot A} \quad \text{with } \sigma_b = \sigma_e + \sigma_p = n \cdot \mu_e \cdot e + p \cdot \mu_p \cdot e \qquad (2)$$

where the charge carrier concentrations n and p for an intrinsic semiconductor can be calculated according to:

$$n = \int_{E_C}^{\infty} D(E) f(E) dE \;\; ; \;\; p = \int_{-\infty}^{E_V} D(E)(1 - f(E)) dE \qquad (3)$$

with the Fermi-Dirac distribution f(E) and the density of states D(E):

$$D(E) = \frac{1}{2\pi^2} \left(\frac{2m_e}{\hbar^2} \right)^{\frac{3}{2}} (E - E_C)^{\frac{1}{2}} \;\; ; \;\; f(E) = \frac{1}{1 + \exp\left(\dfrac{E - E_F}{kT} \right)} \qquad (4)$$

For E_C - $E_F \geq 4$ kT, the charge carrier concentrations n and p can be approximated by:

$$n = N_C \exp\left(\frac{E_F - E_C}{kT} \right) \;\; ; \;\; N_C = 2 \left(\frac{2\pi \, m_e kT}{h^2} \right)^{3/2} \qquad (5)$$

$$p = N_V \exp\left(\frac{E_V - E_F}{kT} \right) \;\; ; \;\; N_V = 2 \left(\frac{2\pi \, m_p kT}{h^2} \right)^{3/2} \qquad (6)$$

The n-type behaviour of SnO_2 is associated with oxygen deficiency in the bulk (see Figure 7). The donors are singly- and doubly ionised oxygen vacancies with donor levels E_{D_1} and E_{D_2} located around 0.03 and 0.15 eV below the conduction band edge [Fon71][Sam73]. In the case of SnO_2 the extrinsic donors are multi-step donors. Therefore, donor and acceptor energy levels, concentrations, and the operation temperature determine the bulk conductivity of SnO_2. Experiments performed on various SnO_2 samples to determine the charge carrier density have resulted in values in the range of $2 \cdot 10^{15}$ to $6.8 \cdot 10^{20}$ cm^{-3} for operation at 300K. Hall measurement results indicate that the shallow donor levels (0.03 eV) are completely ionised above 100K, the deep donor levels (0.15 eV) start to be completely ionised around 400K. Hence, in the typical temperature range for sensor operation (200 - 400°C, i.e. 473 - 673K) the donors can be considered completely ionised.
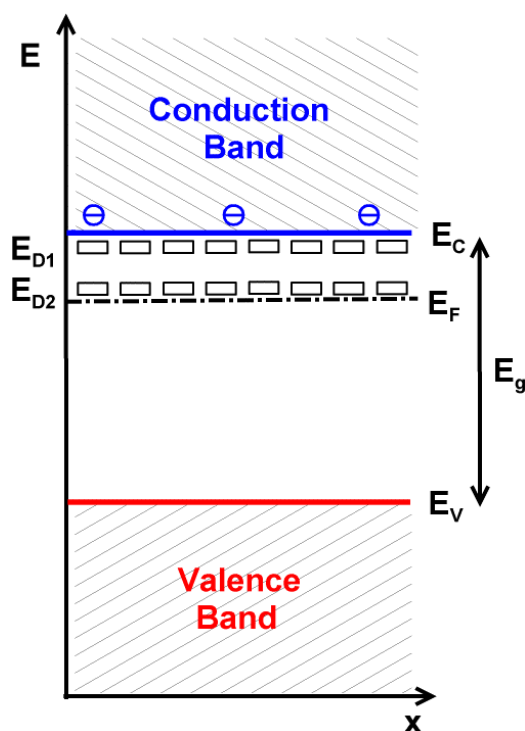
Figure 7: Schematic band diagram of the SnO$_2$ bulk. Two vacancy donor levels E_{D1} and E_{D2} are located 0.03 and 0.15 eV below the conduction band (E_C = 0 eV). The band gab (E_g) is 3.6 eV.

2.1.3.2 Physisorption/Chemisorption

Up to now the effect of the sensor's ambient gas atmosphere has been neglected. Due to the increased reactivity of surface atoms, which lack binding partners, particles from the gas phase will be adsorbed at the SnO$_2$ surface. A distinction has to be made between physical adsorption and chemisorption/ionosorption (see Figure 8). Physisorption is the adsorption with the least possible interaction with no charge transfer. All species show a week physisorption caused by van-der-Waals' dipole/dipole interactions (left graph of Figure 8). Chemisorption is based on stronger forces and hence is connected with an electron transfer between adsorbent and adsorbate. Ionosorption is a so-called "delocalised" chemisorption because the charge is transferred from/to the conduction band. The latter causes changes a band bending by this changing the surface resistance of the sensing material. In the right part of Figure 8 the ionosorption of a gas with acceptor characteristic e.g. O$_2$ is sketched. The adsorption of an electron acceptor on the surface creates acceptor surface level (E_{SS}) where electrons of the conduction band are trapped creating a depletion layer whose depth is described by the Debye length λ_D. The negative charge built at the surface makes further charge transfer more difficult. At equilibrium, a band bending (eV_s) results that influences the material resistance. Reducing gases, e.g. CO, release electrons into the sensitive material upon interaction at the sensor surface and thus decrease the resistance.

If the surface complex X^{ad} possesses a dipole moment, the electron affinity χ is also changed. Both, electron affinity and band bending influence the work function Φ of the sensing layer. Changes of the chemical potential μ are considered negligible in the adsorption of the studied molecules.
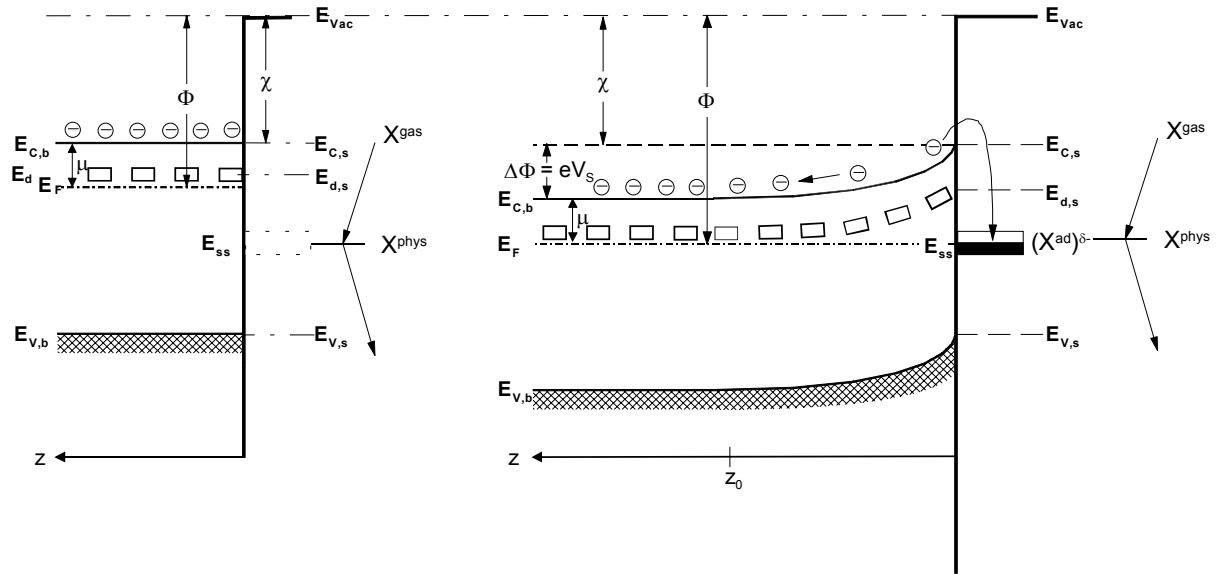
Figure 8: a) Physisorption of gas X on a n-type semiconductor does not change the band diagram and therefore the sensor resistance.

b) Chemisorption of an electron acceptor like O_2 on a n-type semiconductor create surface states E_{SS} that are filled with electrons of the conduction band. This leads to a negative charge of the surface introducing an electric field that prevents a further charge of the surface. A bend bending (eV_S) results that leads to a resistance increase. For chemisorption of an electron donor one obtains a band bending towards lower energies and thus a decrease of the sensor resistance.

2.1.3.3   Grain boundaries

The sensing layer of thick film sensors is very porous and consists of numerous interconnected metal oxide grains. They can be either single crystals or polycrystalline agglomerates. The high porosity enables the ambient gases to access these intergranular connections. Because of this, a depletion layer is created around the grains, the extension of which is determined by the partial gas concentrations and the bulk characteristics of SnO_2. Therefore, grain boundaries, as bottlenecks for electronic grain-grain transfer, play an important role in the sensing layer conduction and therefore, in the detection mechanism.

If the grains are punctually connected and the depletion layer depth λ_D is much smaller than the grain radius r, a grain bulk area unaffected by the gas will still exists. In order to contribute to electronic conduction, the electrons originating from the "bulk" must overcome these depletion layers and the related potential barriers with the barrier heights eV_S at the

intergranular contacts. This is equivalent to a significant resistance increase of the sensitive layer.

As discussed before, the overall resistance R is a function of the contributions of the bulk and the surface of SnO$_2$ grains, the electrode contacts and the intergranular contacts. The properties of the bulk, i.e. the part of the grain, which is not depleted, are not influenced by surface phenomena due to the rather low operation temperatures ($\leq 400°C$). The resistance contribution of the electrode contacts, which is related to Schottky barriers between the sensing layer and electrodes, depends on the contact material. Electrodes might also show a gas dependent catalytic effect. The resistance contribution of intergranular contacts is related to the gas dependent barriers, which have to be overcome for the numerous intergranular contacts between the electrodes. In most cases, the resistance contribution of the numerous intergranular contacts dominates the other contributions.

Then the conduction of thick film sensors can be approximated with the help of the Schottky model by:

$$G = G_o(T) \cdot e^{\frac{-eV_S}{kT}} = G_o'(T) \cdot e^{\frac{E_F - E_C}{kT}} \cdot e^{\frac{-eV_S}{kT}} \tag{7}$$

where G$_0$ and G$_0$' depend on the temperature and geometric properties of the layer.

2.1.3.4 Compact and porous layers

The differences in compact and porous layers are schematically sketched in Figure 9. In compact layers, the interaction with gases takes place only at the geometric surface. In porous layers, the volume of the layer is also accessible to the gases and in this case, the active surface is much higher than the geometric one. Porous layers are characteristic for thick film preparation techniques and RGTO (Rheaxial Growth and Thermal Oxidation, [Sbe95]).
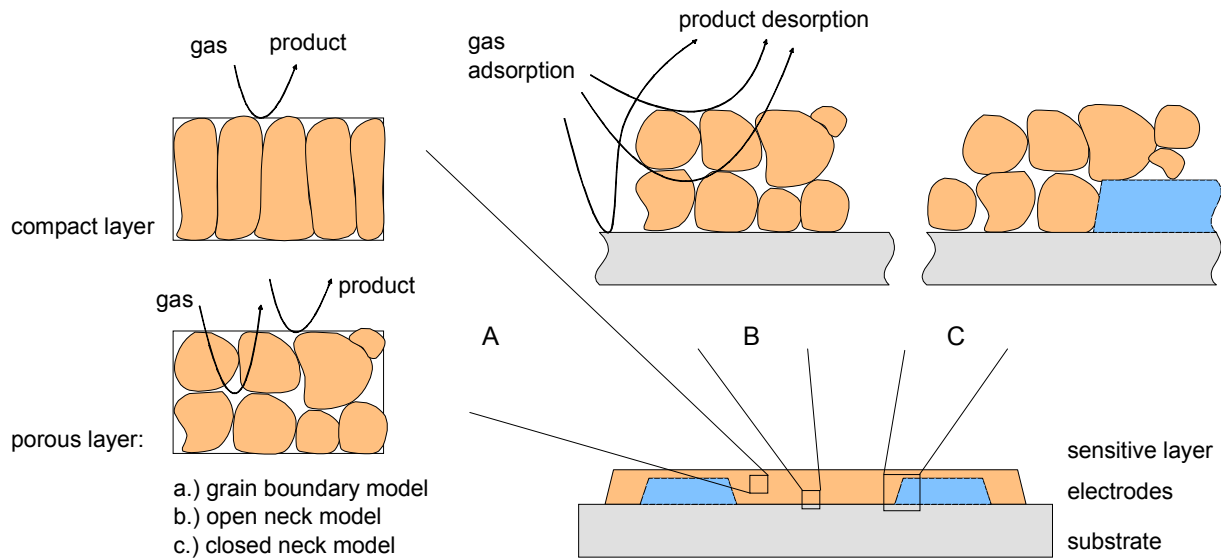
Figure 9: Schematic layout of typical resistive SnO₂ sensor. The sensitive metal oxide layer is deposited over the metal electrodes onto the substrate. In case of compact layers, the gas cannot penetrate into the sensitive layer and the gas interaction is only taking place at the geometric surface. In the case of porous layers, the gas penetrates into the sensitive layer down to the substrate. The gas interaction can therefore take place at the surface of individual grains, at grain-grain boundaries and at the interface between grains and electrodes and grains and substrates [Bâr01].

The type of layer determines the conduction mechanism of the sensor. Here a only a small summary is given; for detailed information see [Bâr01].

For compact layers, there are at least two possibilities: completely or partly depleted layers[1], depending on the ratio between layer thickness and Debye length λ_D of the electron. For partly depleted layers, when surface reactions do not influence the conduction in the entire layer the conduction process takes place in the bulk region. Formally, two resistances occur in parallel, one influenced by surface reactions and the other not; the conduction is parallel to the surface, and this explains the limited sensitivity of compact layers (see also Figure 10).

For porous layers the situation can be further complicated by the presence of necks between grains. It may be possible to have all three types of contribution in a porous layer: surface/bulk (for large enough necks, layer thickness > thickness of depletion layer), grain boundary (for large grains not sintered together), and flat bands (for small grains and small necks). For small grains and narrow necks, when the mean free path of free charge carriers becomes comparable with the dimension of the grains, a surface influence on mobility should be taken into consideration. This happens because the number of collisions experienced by the free charge carriers in the bulk of the grain becomes comparable with the number of surface

---

[1] The depletion layer is formed due to gas adsorption like O_2.

collisions; the latter may be influenced by adsorbed species acting as additional scattering centres (see discussion in [Bâr94]).

Figure 10 illustrates the way in which the metal-semiconductor junction, built at electrode-sensitive layer interfaces, influences the overall conduction process. For compact layers they appear as a contact resistance (R_C) in series with the resistance of the SnO_2 layer. For partly depleted layers R_C could be dominant, and the reactions taking place at the three-phase boundary, electrode-SnO_2-atmosphere, control the sensing properties.

In porous layers, the influence of R_C may be minimized due to the fact that it will be connected in series with a large number of resistances, typically thousands, which may have comparable values (R_{gi} in Figure 10). Transmission Line Measurements (TLM) performed with thick SnO_2 layers exposed to CO and NO_2 did not result in values of R_C clearly distinguishable from the noise [Bau97] [Sch98], while in the case of thin films the existence of R_C was proved [Hoe95].
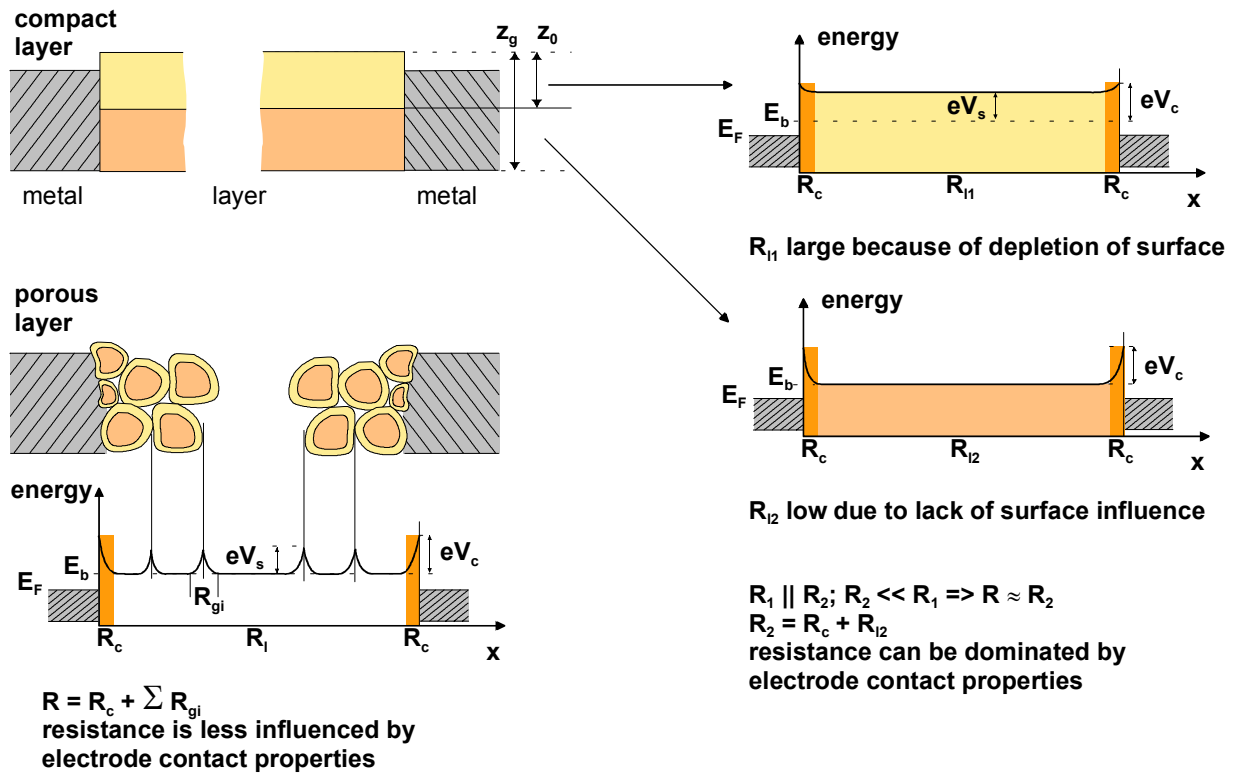
Figure 10: Schematic representation of compact and porous sensing layers with geometry and energetic bands, which shows the possible influence of electrode sensing layers contacts. R_C resistance of the electrode-SnO_2 contact, R_{l1} resistance of the depleted region of the compact layer, R_{l2} resistance of the bulk region of the compact layer, R_1 equivalent series resistance of R_{l1} and R_C, R_2 equivalent series resistance of R_2 and R_C, R_{gi} average intergrain resistance in the case of porous layer, E_b minimum of the conduction band in the bulk, eV_S band bending associated with surface phenomena on the layer, and eV_C also contains the band bending induced at the electrode-SnO_2 contact.

2.2   Gas interaction with SnO_2 thick film sensors

Gas sensors are usually operated in an ambient atmosphere containing oxygen and humidity. Therefore, it is important to understand the gas interaction of SnO_2 gas sensors with oxygen (O_2) and water (H_2O), which determines to a significant extent the response of SnO_2 gas sensors. The first part of this chapter deals with the interaction of O_2 and H_2O on SnO_2 surface. Later the sensing mechanism of some of the test gases CO, CH_4 and propane, which are target gases for different applications are discussed in the presence/absence of O_2 and H_2O.

2.2.1 Oxygen (O₂)

The species found on semiconductor surfaces of adsorbed O_2 are manifold and depend on the operating temperature of the sensor. At typical operation temperatures of semiconductor gas sensor - between 100 and 500°C - the interaction with the atmospheric O_2 leads to its ionosorption in molecular (O_2^-) and atomic (O^-, O^{--}) forms.

It is proved by TPD (Temperature Programmed Desorption), FTIR (Fourier Transform InfraRed Spectroscopy), ESR (Electron Spin Resonance spectroscopy) that below 150°C the molecular form dominates and above this temperature the ionic species. The presence of these species is leading to the building of a depletion layer at the surface of SnO_2. The dominating species are depending on temperature and, probably, on surface dopants. Typical results available in the literature are summarised in Figure 11.
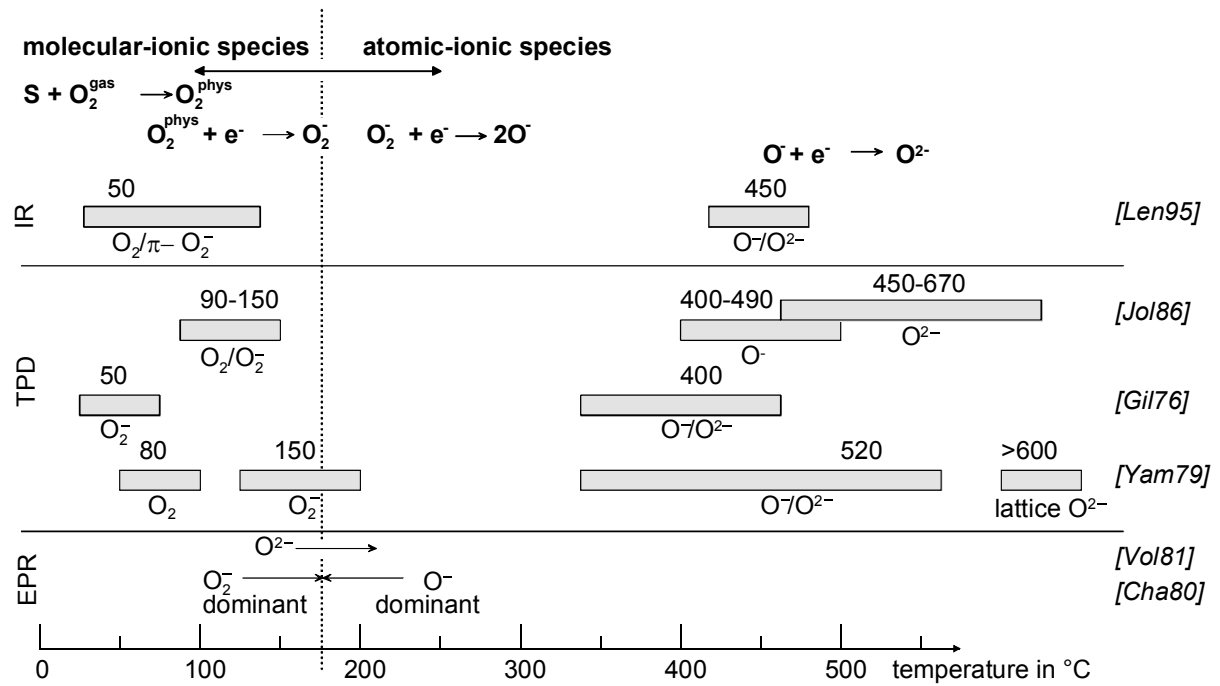
Figure 11: Literature survey of oxygen species detected at different temperatures at SnO₂ surfaces with IR (InfraRed analysis), TPD (Temperature Programmed Desorption), EPR (Electron Paramagnetic Resonance). For details, see listed references

The equation describing the oxygen chemisorption can be written as:

$$\frac{\beta}{2} O_2^{gas} + \alpha \cdot e^- + S \; \rightleftharpoons \; O_{\beta\,S}^{-\alpha} \tag{8}$$
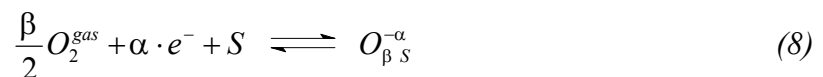
where O_2^{gas} is an oxygen molecule in the ambient atmosphere and e^- is an electron which can reach the surface despite the electric field resulting due to the accumulation of negatively charged particles at the surface. Their concentration is denoted by number of electrons in the surface layer (n_S), S is an unoccupied chemisorption site for oxygen, $O_{\beta\,S}^{-\alpha}$ is a chemisorbed

oxygen species with; $\beta = 1$ for atomic forms, $\beta = 2$ for molecular forms, $\alpha = 1$ for singly ionised forms, $\alpha = 2$ for doubly ionised forms.

Detailed description of how O_2 adsorption influences the band bending, the number of surface states, etc. can be found in [Wei01], [Bâr01], [Kap01]. In these references, it is pointed out that the chemisorption of oxygen is a process, which has two parts: An electronic one and a chemical one. This is coming from the fact that the adsorption is produced by the capture of an electron on a surface level, but the surface level does not exist in the absence of the adsorbed atom/molecule. This fact indicates that at the beginning of the adsorption the limiting factor is chemical, the activation energy for adsorption/dissociation, due to the unlimited availability of free electrons in the absence of band bending. After the building of the surface charge, a strong limitation is coming from the potential barrier, which has to be overcome by the electrons in order to reach the surface. The desorption is controlled from the very beginning by both electronic and chemical parts; the activation energy is not changed during the process if the coverage is not high enough to provide interaction between the chemisorbed species [Mor90]. The maximum coverage of adsorbed oxygen is $10^{-5} - 10^{-3}$ of a monolayer (ML) because of the electrostatic reasons (Weisz limitation [Wei53]).

Summarizing, the adsorbed oxygen removes electrons from the conduction band of the SnO_2 that results in an increase of sensor resistance respectively an increase of conductivity. The conductance of a sensor is inversely proportional to the root of the oxygen partial pressure p [Adv80][Ega87]:

$$G \left(= \frac{1}{R} \right) \propto p_{O_2}{}^{-0.5} \qquad (9)$$

The exact value is modified by additives in the sensor material or by changing structures, such as thickness of the active material. This is why the mechanism whereby the oxygen pressure controls the conductivity has been described is simplistic: it must actually be more complex in order that modifications to the value of β become at all possible.

2.2.2 Water (H_2O)

In nearly every applications water is present as an interfering gas. For this reason the interaction of the semiconductor surface with water is of great interest. TPD and IR studies showed, as summarised in Figure 12, that the interaction with water vapour results in molecular water, adsorbed by physisorption or hydrogen bonding, and hydroxyl groups. Above 200°C molecular water is no longer present, whereby OH groups are still present above 400°C. IR investigations prove the presence of hydroxyl groups. However, the way in

which and where the hydroxyl groups are fixed on the tin dioxide is still under discussion. There are publications claiming that the hydroxyl groups are based on an acid/base reaction of the OH^{-} sharing its electronic pair with the Lewis acid site (Sn) and leaving the weakly bonded proton, H^{+}, ready for reactions with lattice oxygen (Lewis base) or with adsorbed oxygen [Bar93]. Others assume a homolytic dissociation of water resulting in two hydroxyl groups, an 'isolated' hydroxyl bond to Sn and a 'rooted' hydroxyl group including lattice oxygen [Hei88].

physisorbed   hydrogen bond   chemisorbed hydroxyl groups

$H_2O^{gas}+ S \longrightarrow H_2O^{phys}$

$H_2O^{phys} \longrightarrow H_2O$ (H-H bond)

H_2O (H-H-bond) $+ O_{lat}^{-} \longrightarrow$ 2 OH $+ V_{O,s}$ $V_{O,s} \longrightarrow V_{O,lat}^{\bullet} + e^{-}$ *[Koh92]*
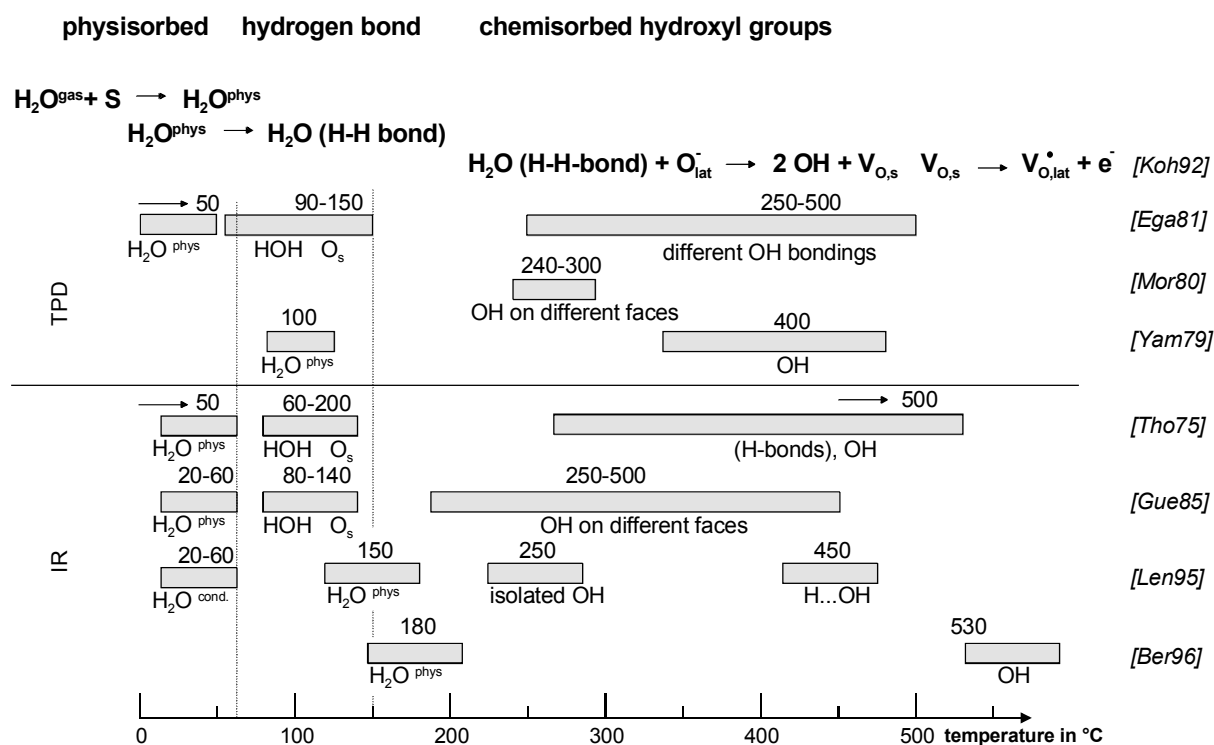
Figure 12: Literature survey of water-related species [Cli82] formed at different temperatures at SnO₂ surfaces. The results have been obtained by means of IR (InfraRed analysis) and TPD (Temperature Programmed Desorption).

All experiments reported a reversible decrease in the surface resistance in the presence of water. The resistance decrease does not vanish with the molecular water but with the disappearance of hydroxyl groups and could therefore be related to the presence of hydroxyl groups [Gil76]. Various types of mechanisms have been suggested to explain this finding. Two direct mechanisms have been proposed by Heiland and Kohl [Hei88]. The first mechanism attributes the role of electron donors to the 'rooted' OH group, which includes lattice oxygen according to:

$$H_2O + Sn_{lat} + O_{lat}^{-} \; \rightleftharpoons \; (HO - Sn_{lat}) + (O_{lat}H)^{+} + e^{-} \qquad\qquad (10)$$

whereby Sn_{lat} and O_{lat} are tin and oxygen atoms in the lattice.

The reaction would imply the homolytic dissociation of water and the reaction of the neutral
H atom with the lattice oxygen:

$$H + O_{lat}^{2-} \quad \rightleftharpoons \quad (O_{lat}H)^- + e^- \qquad (11)$$

The second mechanism takes into account the reaction between the proton and the lattice
oxygen and the binding of the resulting hydroxyl group to the Sn atom. The resulting oxygen
vacancy produces additional electrons by ionisation according to:

$$H_2O + 2Sn_{lat} + O_{lat} \quad \rightleftharpoons \quad 2(OH - Sn_{lat}) + V_O^{\cdot\cdot} + 2e^- \qquad (12)$$
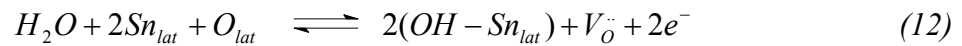
Others [Mat88b], [Schi91] assumed that instead of a reaction with the surface lattice, a
reaction with chemisorbed oxygen, which results in two hydroxyl groups linked to Sn occurs.
Morrison [Mor90] as well as Henrich and Cox [Hen94] consider an indirect effect, i.e. the
interaction between either OH⁻ or H⁺ with an acidic or basic group, which are also acceptor
surface states. The coadsorption of water with another adsorbate, which could be an electron
acceptor, may change the electron affinity of the latter. Henrich and Cox suggested that
preadsorbed oxygen could be displaced by water adsorption. In addition, others have found
hints for an influence of water vapour on oxygen chemisorption. Caldararu and others (e.g.
[Cal96], [Vla93], [Ion99]) assume a blocking of the adsorption sites for oxygen by water. For
all these mechanisms, the particular state of the surface plays a major role. Surface doping can
also influence these phenomena. Egashira et al [Ega81a] showed by TPD and isotopic tracer
studies that the rearrangement of oxygen adsorbates due to the presence of water vapour
depends on the surface doping. Williams and Morris al. also reported that H_2O displaces
chemisorbed oxygen by H_2O_{ads} and OH_{ads} producing on SnO_2 a surface electronic state such
as a surface hydroxyl species, which lies higher in energy than the oxygen species, which is
displaced [Mor01].

Clifford and Tuma [Cli82] approximated the influence of water vapour in synthetic air
empirically by:

$$R = R_0 \left(1 + k_{H_2O} \cdot p_{H_2O}\right)^{-\beta} \qquad (13)$$

with the water-independent constants R_0, k_{H_2O} and β and the water concentration in
volumetric ppm p_{H_2O}.

2.2.3 Carbon monoxide (CO)

CO is one of the main gases of interest in the field of gas sensor applications. It is a target gas in case of fire detection, incomplete burning, etc. as well as an interfering gas because of its high reactivity with semiconductor gas sensors. Because of this, it is mostly chosen – besides H_2 – to characterise the sensor performance. In addition, the physical and chemical properties of CO facilitate investigations monitoring CO and its typical reaction product CO_2; with the help of IR one can trace the production of CO_2 by looking at its adsorption wavelength.

In the following a distinction is made between CO interaction with SnO_2 surfaces in the presence of oxygen, which is well characterised and in the absence of oxygen (no UHV conditions), where not much data is available.

2.2.3.1 In the presence of O_2

Carbon monoxide is considered to react with pre-adsorbed or lattice oxygen [Hen94]. IR studies identified CO-related species i.e. unidentate and bidentate carbonate between 150°C and 400°C and carboxylate between 250°C and 400°C. A summary of the IR results is presented in Figure 13. Moreover, the formation of CO_2 as a reaction product between 200°C and 400°C was identified by FTIR.
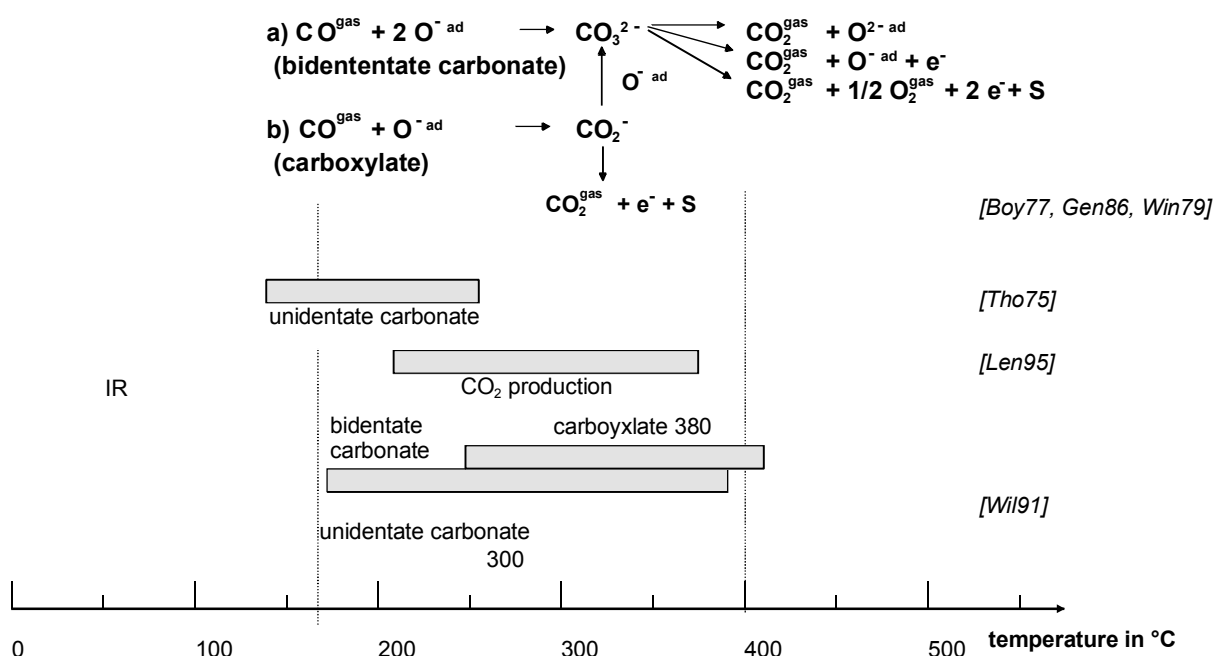
Figure 13: Literature survey of CO-related species found by means of IR (infrared analysis) at different temperatures on a (O_2) preconditioned SnO_2 surface. For details, see listed references.

All experimental studies in air at temperatures between 150°C and 450°C reported an increase in the surface conduction in the presence of CO. It is generally accepted that the CO reacts with ionosorbed oxygen species and thus release electrons in the conduction band.

Morrison derived – using a simplified model – the dependence of the resistance on the partial pressure of CO [Mor87]. He assumed that oxygen is present as O^{2-} and O^{-} at the sensor surface according to:

$$e^{-} + O_2 \;\rightleftharpoons\; O_2^{-}; \quad e^{-} + O_2^{-} \;\rightarrow\; 2O^{-} \qquad\qquad (14)$$
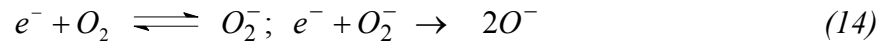
Hereby the reverse reaction of the latter reaction is neglected due to the small probability of a reaction, which is of second order in O^{-} concentration. In addition, he assumed that due to the high reactivity of O^{-}, the reaction of O_2^{-} with CO could be neglected. It is:

$$CO + O^{-} \;\rightarrow\; CO_2 + e^{-} \qquad\qquad (15)$$

The detailed description of how the resulting equation of the steady state can be solved is given in [Bâr01]. An overview of the various conductance dependencies found is given in Table 2.

Table 2: Equations describing the dependence of conductance on CO concentration as derived empirically or from theoretical calculations.

Equation	Comments / Assumptions	Literature
$G \sim n_S \sim p_{CO}^{2\beta/(\alpha+1)}$	$L_D > r$: reactive oxygen species: $O_\beta^{\alpha-}$; $\beta = 1, 2$; $\alpha = 1, 2$, i.e. O_2^-, O^-, O^{2-}	[Bâr94]
$G \sim n_S \sim p_{CO}^{\beta/(\alpha+1)}$	$L_D < r$: reactive oxygen species: $O_\beta^{\alpha-}$; $\beta = 1, 2$; $\alpha = 1, 2$, i.e. O_2^-, O^-, O^{2-}	
$G \sim p_{CO}^{0.5}$	empirical	[Fig95]
$G = G_0 + A_1 p_{CO}^{1/2}$	rate equations + SC[1] physics	[Win79]
$G = G_{air} + A_1 p_{CO}^{n}$	empirical	[Pin80]
$G \sim (A_0 + A_1 p_{CO}^{m})^{0.92}$	SC physic	[Pin80]
$G^2 - G_{air}^2 \sim p_{CO}$	rate equation and SC physic	[Bâr89]
$G^\beta - G_{air}^\beta \sim p_{CO}, \beta \geq 2$	rate equations and SC physics	[Ipp90]
$G \sim 1/A \sim \ln(p_{CO})$	open neck	
$n_S \sim n_b \exp(-eV_S^{eff} / kT)$	closed neck	

It is well known that the presence of water in the ambient atmosphere has a strong influence on the CO detection. It has been observed [Schi91, Cli82] that water enhances the interaction of CO. Three models have been proposed which may account for this observation. On the one hand, it has been assumed that water enhances the reaction with oxygen [Ega81]. On the other hand, a reaction of CO with hydroxyl groups [Ion94], [Schi91], [Kap99] has been proposed. Various equations have been derived for the sensor conductance in the presence of CO and water vapour. Kappler et al. reported that an increase in humidity leads to an increase in the number of oxygen vacancies (equation 12) [Kap99]. The oxygen vacancies enhance the chemisorption of oxygen and form specific oxygen sites [Yam79], [Cox98]. The increase in the number of available oxygen reaction partners for CO leads to an enhancement of the sensor signal

A summary is given in Table 3. Moreover, in some cases a correlation between ageing and the irreproducibility of sensors and the presence of water-related species could be found [McA87], [Mat88b].

---

[1] semiconductor

Table 3: Equations describing the dependence of conductance on the CO concentration and the water vapour pressure as derived empirically or from theoretical calculations.

Equation	Comments / Assumptions	Literature
$G \sim (1+k_{CO}\, p_{H_2O}\, p_{CO})^{\beta}$	Empirical	[Cli82]
$G \sim (p_{CO}\, p_{H_2O})^{1/3}$	rate equations and SC physics	[Str83]
$G \sim$ $p_{CO}/p_{0,CO})^{\beta_{CO}}(p_{H_2O}/p_{H_2O,0})^{\beta_{H_2O}}$	rate equations and SC physics	[Bâr93, Schi91]

2.2.3.2   CO interaction in the absence of oxygen

There are only a few papers dealing with gas interaction of semiconductor SnO$_2$ gas sensors in the absence of oxygen. The few relevant for this thesis are listed below.

Safonava at al. studied the mechanism of CO sensing in nitrogen for nanocrystalline undoped and Pd doped SnO$_2$ by Mössbauer spectroscopy and conductance measurement [Saf02]. The conductance measurements were coupled with Mössbauer spectroscopy [Mad97] and carried out at different temperatures (50 – 380°C) and at a constant CO concentration of 1% in nitrogen. With the help of the Mössbauer spectroscopy the reduction of Sn(IV) to Sn(II) in the presence of CO was studied. They found that the electrical response of 1% w.t. Pd doped and undoped SnO$_2$ at temperatures between 125°C and 380°C is associated with the process announcing the beginning of Sn (IV) to Sn(II) transition. Accordingly, CO reacted with lattice oxygen, but, as no metallic tin was detected in the spectra, Sn is not completely reduced.

In situ Electron Paramagnetic Resonance spectroscopy (EPR) confirmed the change of chemisorbed oxygen O_{2S}^{-} and single ionized oxygen vacancy $V_O^{\bullet}$ concentration in SnO$_2$ during the interaction with CO/N$_2$ gas mixtures [Can97] (see chapter 2.2.1).

2.2.4   Methane (CH$_4$)

CH$_4$ is generally measured in comparison to CO because of its different reaction mechanism and dependency on humidity [Kap01]. It is the simplest representative of hydrocarbons and its detection itself and its higher homologues are target gases for sensors monitoring gas burn leakages or automotive exhausts.

Experimental studies report a decrease of the sensor resistance in the presence of CH$_4$. It is observed that CH$_4$ detection is favourable at higher temperatures than CO detection. Kohl et al. [Koh92] assumed, based on TDS and reactive scattering results, two principle reaction pathways for CH$_4$. The first involves the reaction with lattice oxygen and the second one the reaction with ionosorbed oxygen. The product fluxes were independent of the primary oxygen

flux. Kohl attributed this observation to the surface oxygen density due to the Weisz limitation. Tournier et al. [Tou99] interpreted similar results as a hint for a methane interaction that does not involve oxygen adsorbed species (Figure 14 right char flow). The reaction of CH_4 with lattice oxygen leads to the creation of oxygen vacancies, which can be tin oxide donors by diffusion into the bulk. Therefore, they can account for the removal of ionosorbed oxygen and the resistance increase observed in the presence of CH_4 at higher sensor operation temperatures.

In the presence of adsorbed oxygen, the oxidation process of CH_4 at the SnO_2 surface involves further reaction route (left-side of Figure 14). All the reaction products in the absence of gaseous oxygen are present and in addition small amounts of ethanol (CH_3CH_2OH), acetic acid (CH_3COOH), keten (CH_2CO) and formaldehyde (H_2CO).

Reactive scattering at 500°C
$CH_4 + O_2$ on SnO_2
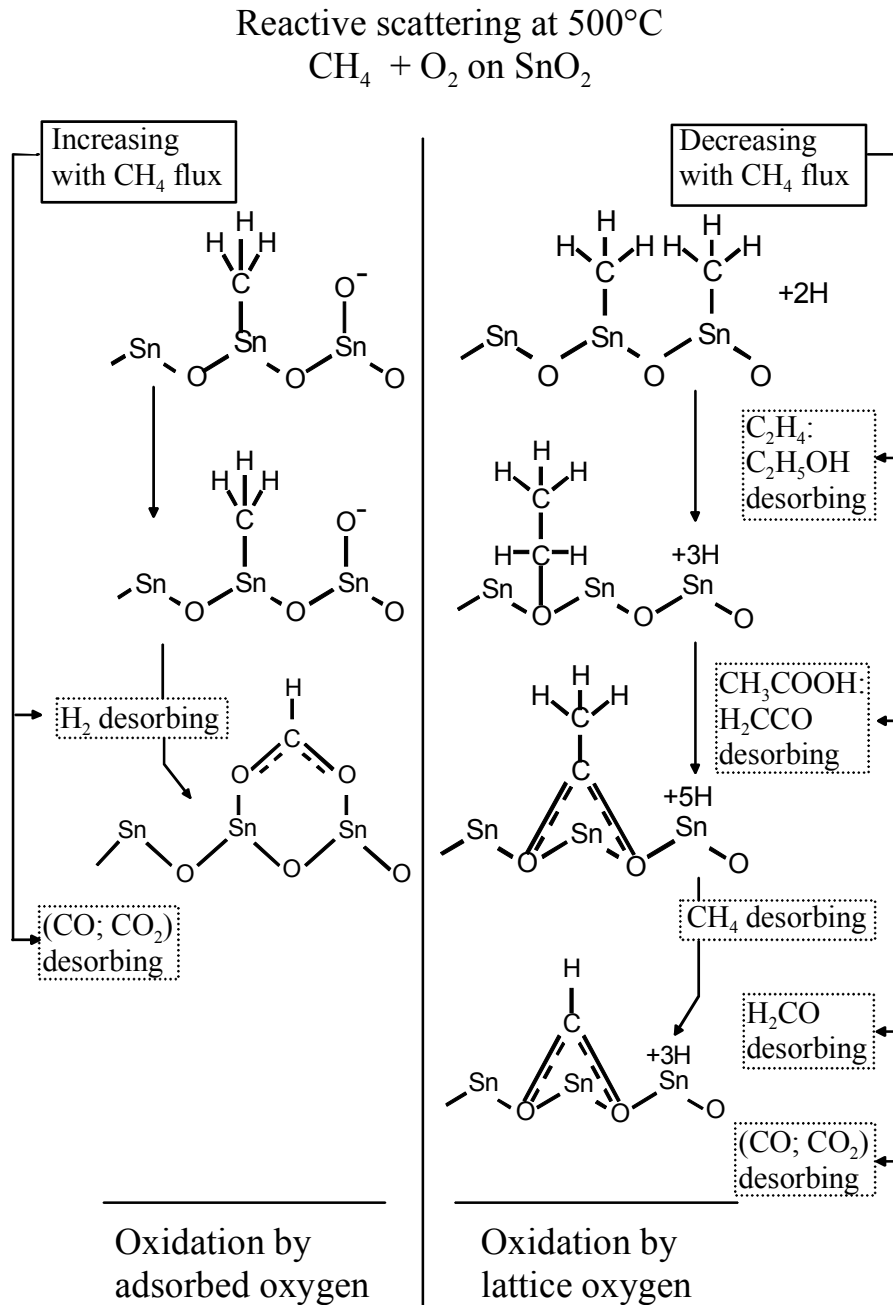
Figure 14: Reaction scheme of methane (CH₄) with oxygen on a sputtered SnO₂ film derived from reactive scattering data. Hydrogen atoms, released or consumed in all steps, are not sketched. For details see [Koh89][Wei01].

For the influence of water on CH_4 sensing, several models have been proposed. Egashira et al. found a decreasing reaction of CH_4 with oxygen in the presence of water [Ega83]. They assumed that water blocks the adsorption sites for methane. Recently, Ionescu et al. proposed a model, which is based on dynamic resistance measurements for the water influence on the CH_4 interaction [Ion99]. They assume that CH_4 reacts with lattice oxygen hereby competing with water for the same oxygen sites, whereas CO and water react with different oxygen types.

2.2.5 Propane (C$_3$H$_8$)

There are no papers dealing with the sensing mechanism of C$_3$H$_8$ on semiconductor surfaces. Sensor measurements performed with C$_3$H$_8$ and other hydrocarbons showed the same dependencies on humidity as CH$_4$ [Kap99]. It was mentioned before that one determining step in CH$_4$ and therefore hydrocarbon sensing is the separation of a hydrogen atom and the adsorption of CH$_{3ads}$. As the binding energy C—H is the biggest among the class of hydrocarbons (443 kJ/mol compared to 413 kJ/mol for primary CH bonds of higher alkanes [Mor86]) the reactivity of higher respectively branced hydrocarbons is higher [Kim97].

2.3 SnO$_2$ based gas sensors

The SnO$_2$ gas sensors can be distinguished by many parameters. The most common is the discrimination in thick and thin film sensors. This reflects to a certain extent the different composition – compact or porous - of the layer itself (see chapter 2.1.3.4), which is an important feature for the electronic sensing characteristics of gas sensor [Wei01]. Thick film layers are in general porous and thin film compact.

Another grouping of SnO$_2$ gas sensors arise simply by the size of the sensor and due to it the manufacturing technology or process. Sensors with a size around some hundred micrometer of sensitive area are called micromachined. The techniques used for manufacturing are adapted from chip production like CMOS or MEMS (Micro Electro Mechanical Systems). Micromachined sensors typically are e.g. MOSFET (Metal Oxide Semiconductor Field Effect Transistor) and ISFETs (Ion-Sensitive Field Effect Transistor).

First, thin and thick film sensor will be treated in respect to preparation methods and typical application. Second, some developments towards micromachining of chemical gas sensors are showed. At last, a selection of commercial available SnO$_2$ gas sensors will be mentioned.

2.3.1 Thick film gas sensors

Ceramic thick film sensors were the first type of metal oxide semiconducting sensors. The first sensors were fabricated by pressing a heater coil and an electrode wire in the powder material (Taguchi sensors [Tag62]). The sensitive material was painted as a paste on a alumina tube, in which the heater was separated from the layer. Later planar structures were obtained by thick-film technologies like screen-printing onto electrode-covered ceramic Al$_2$O$_3$ substrates with a heater and temperature sensor at the backside (see chapter 3.1.2.1).

The oxide base material is typically prepared from salt solutions (mostly SnCl$_4$), organo-tin compounds, or the pure metal dissolved in nitric acid as precursors. This process will be

nominated more general the sol-gel process, knowing that normally this means a special preparation route [Ka01], [Sch98]. Improvements of the sensor properties are possible by chemical modifications of the precursor or of the base material. Catalysts and receptor functions [Yam91] can be introduced before or during the preparation of the paste by mixing the calcined powder with salt solutions (e.g. $PtCl_4$ impregnation or $K[PtO]$ fixation method) or by addition of metals (colloid method) [Mat92b]. In this case it is supposed, that the stannic oxide surface adsorbs all the metal catalyst from the solution. The intended catalyst concentration is calculated as weight percent usually in the range between 0.01 to 3%. The catalyst surface density could therefore be much higher. Typical catalysts are noble metals like Pt [Lee87], Pd [Hue89], Au [Mae93], Cu [Yoo95] or basic materials like Ca [Xu91a] or La [Miz93].

In spite of their complicated microscopic and chemical structure, the ceramic sensors have surprisingly good sensitivities, because they have been optimised by a careful choice of materials and preparation steps. Nevertheless long-term stability can only be achieved by long pre-aging times. Other drawbacks are the high power consumption of the final bulky device and problems arising mounting the hot sensor element.

2.3.2   Thin film gas sensors

Compared with the preparation methods for thick film sensor, the fabrication of thin-film structures is based upon a number of well-defined evaporation or sputtering processes under clean room conditions. A selection of different methods is given in Table 4.

Table 4: Typical deposition techniques used for the preparation of thin film semiconductor sensors like the prototype material SnO_2. For details see [Sch98].

chemical vapor deposition (CVD)	physical vapour deposition (PVD)	
	sputtering	evaporation
Thermal CVD	Sputtering	Molecular beam epitaxy
Plasma activated CVD	Reactive sputtering	Thermal evaporation
Laser induced CVD	Cathode sputtering with bias	Reactive evaporation
Electroless plating	voltage	Ion plating
Spray pyrolysis	Ion beam deposition	Reactive ion plating
Melt dipping	Ionised cluster beam (reactive)	Arc evaporation
Liquid quenching	Plasma decomposition	Laser evaporation
Deposition of organic polymers		
Deposition of emulsions		

Most of the techniques listed in Table 4 are direct spin-offs from the semiconductor industry. The processes used for the preparation of sensitive layers are also used for structuring the complete sensors device. Therefore, one aim is to use silicone as a substrate material. A large knowledge and apparatus base is already available, which allows the production of cheap devices. The sensor is structured on these substrates by means of common lift-off-processes. Adhesion layers of Ta, Ti, Cr, TiW has to be used for a good quality of the contacts (Au, Pt, Al). Heating elements, and temperature sensors are produced from poly-Si or Pt, and insulation layers in case of Si wafers from SiO_2 or Si_3N_4. Micromachining and etching of diaphragms in Si wafers is performed by adjusting the etching time or using highly doped stopping layers [Chu94][Dem93].

Bulk-doping with homogeneous dopant concentration may be achieved by using corresponding mixed metal- or oxide-based targets with the intentional composition of the film. Alternatively, several independent evaporation sources may be operated under the conditions of continuous or chopped evaporation of the oxide and its bulk additives. Surface-doping is possible by subsequent evaporation of metals.

The most common preparation method for thin film sensors is the vapour deposition which are clean and well controllable methods. Each method has its own (dis)advantages. Important parameters are

- Total pressure, the partial pressure of the evaporated gas, and of a reactive gas
- Substrate temperature

which have to be optimised. Chemical vapour deposition (CVD) techniques usually need higher substrate temperature to bring the precursor material to reaction; physical vapour deposition (PVD) techniques need low partial pressures to have a long enough mean free path. In PVD the chemistry of the deposited material does not play a substantial role in the deposition process, whereas in CVD it defines the feasibility and the deposition parameters.

Sberveglieri et al. introduced a special preparation method for porous thin films [Sbe91]. It was named Rheotaxial Growth and Thermal Oxidation (RGTO) for the deposition of tin on a substrate with the temperature just below the melting point of tin, and subsequent oxidation (reactive growth) of the grains with well-defined temperature program in oxidizing atmosphere.

In CVD the film is formed by thermal decomposition of gaseous molecules on the hot substrates. This process is controlled by mass transport and by the reaction constants. SnO_2 layers can be processed by CVD from different precursors: from tin (II) or (IV) chloride

[Gal95],[Hon94b], from dibutyltin tetraacetate [Sbe93], [All93], from oxalates [Ega96]], or other organo-tin compounds [Chu94], [Tsa95].

The mayor drawback of thin film sensors is their low sensitivity because of the small surface area available for the test gas.

2.3.3 Micromachined sensors

Micromachined sensors are processed by techniques also used for chip technology. In general, microsensors consist of an active area that comprises a heater, sensor electrodes and a gas sensitive layer situated at the centre of a thin membrane which itself is supported by an outer frame of silicon (micro-hotplates). The sensing layer can be processed by thin film technologies like PVD resulting in thin films or are drop coated. The first is mostly used. In the following, two types of micromachined, sensors will be introduced on selected samples. Firstly two types of Si-micromachining based sensors, one developed by Semancik at. al [Sem01] and the seconded developed in cooperation by Institute of MicroTechnolgy (IMT) of Neuchâtel in Switzerland and IPC are introduced; both are based on micro-hotplates but they use different types of sensitive layer. Secondly, gas sensors fabricated by (compatible) CMOS technology with integrated circuitry are presented as they have been developed up to now.

2.3.3.1 Micro-hotplate chemical gas sensor

In the following, two types of micromachined sensors are introduced based on CMOS-compatible mirco-hotplate structures as main element of the sensors. Differences occur in the design of the sensor and in preparation of the SnO_2 coating.

At the IMT micro-hotplates are made by using silicon bulk mircomachining [Bri99][Bri00]. Deep Reactive Ion Etching (DRIE) is used for silicon etching at the back side and so for releasing a dielectric membrane (1.0 - 1.5 mm) that thermally isolates the heated sensing area from the chip frame (see Figure 4). The membrane itself is made of low stress LPCVD (Low Pressure Chemical Vapour Deposition) silicon nitride ($0.25 - 0.5$ μm). Platinum (250 nm) is used both for heater and electrodes. The insulation layer consists of low-stress LPCVD silicon nitride or annealed CVD oxide (0.5 μm) and the passivation layer on the top of low-stress LPCVD nitride (0.2 μm).

This kind of sensor can withstand high annealing temperatures (~ 700°C) and a pulsed temperature mode operation. The sensor was drop coated with SnO_2 thick film by IPC. This sensor combines the high sensitivity of thick film SnO_2 gas sensors with the fast response time of mircomachined substrates.

It was also possible to transfer deposition methods known for ceramic substrates to micromachined ones. Vincenzi et al. report on a thick film gas sensor deposited for the first time by screen-printing technique onto a micromachined hotplate [Vin01].

The basic MEMS sensing device structure developed at NIST (National Institute of Standards and Technology) by Semancik at al. in the early 1990's, is a temperature-controllable micro-hotplate illustrated in Figure 15. The left picture in Figure 15 shows a suspended mirco-hotplate with four arrow-shaped electrodes, which as been produced by surface micromachining the Si on which the device was fabricated. The functional layers are shown in the left schematic picture of Figure 15. Micro-hotplate fabrication was done differently at three foundries offering different advantages and limitations. For details see [Sem01] and the references therein.
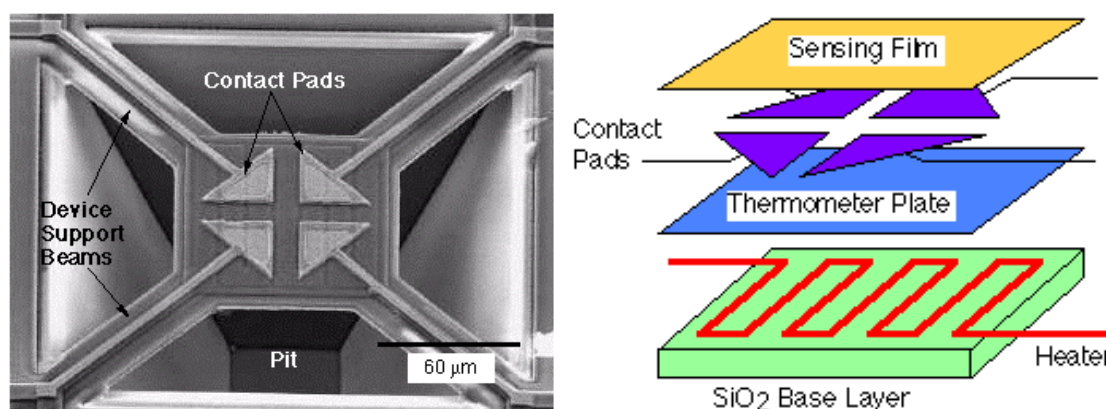
Figure 15: Left: Micrograph of single micro-hotplate with four arrow-shaped electrodes. Right: Schematic of functional layers in a surface-micromachined micro-hotplate.

Local heating is made possible by a polysilicon resistive heater. Temperature measurement can be done by calibrated resistance measurements on either the polysilicon heater or the heat distribution/thermometry plate, and use as feedback input. The accessible temperature range is 20°C – 500°C (with heat distribution/thermometry plate) and 20°C – 750°C (without the plate). The top surface microelectrodes contacts the sensing SnO_2 thin film deposited by e.g. self-lithographic CVD.

Semancik et al. designed different microsensor array prototype platform with 4 or 16 micro-hotplate elements.

These kinds of micromachined sensors comprise the advantage of small size especially if sensor arrays on a single chip are realised, low power consumption, batch production, etc. The mayor drawback, which was already mentioned in the motivation, is that post-processing steps can only provide electronics.

2.3.3.2   CMOS processed gas sensors with circuitry

A gas sensor processed in CMOS technology provides the possibility to integrated electronics on chip, which acquire, amplify and evaluate the electrical sensor signal. This is will enable to provide a low cost self-maintaining gas sensor. Now the development of CMOS processed semiconductor gas sensors with integrated circuitry just began and one of the first developments is introduced in this work. Papers dealing with gas sensors based on CMOS technology have been published for 2 – 3 years introducing different sensing technologies.

Baltes et al. al introduced different kinds of sensors based on CMOS chips [Bal01]:

- CMOS based thermal imagers with up to 1280 pixels [Scha01]. Incoming IR radiation is adsorbed by the membrane sandwich and heats up individual pixels. This temperature increase is converted into an electrical output voltage using integrated thermopiles consisting of the polysilicon and the aluminum layer of the CMOS process. The individual thermopiles are addressed by an on-chip multiplexer and the thermo voltage is amplified on-chip using a low-noise amplifier.

- Temperature microsensors consisting of an aluminum resistor of circular shape, which is integrated around a circular bonding pad [May00].

- Stress piezoresistive microsensors integrated below test bonding pats [May00].

- Chemical microsensors using spray-coated polymer films as chemically sensitive layer [Bal99]. Changes in the mass, temperature and dielectric constant of the polymer upon analyte absorption are sensed with resonant [Lan99], calorimetric [Ker00], and capacitive [Kol99][Hag99] sensing structures, respectively. All three types can be fabricated on a single die together with their signal conditioning circuitry.

The latter comprises the advantages of sensor arrays operating with different sensor principles. Different polymer films will improve the selectivity of the chemical microsystem towards specific analytes.

There are other groups who have been developed CMOS based gas sensors like:

- Suehle et al. [Sue93] successfully fabricated CMOS compatible sensors through a commercial foundry (MOSIS). These sensors are based on oxide Al micro-hotplates and polysilicon heaters.

- Udrea et al. introduced design and simulations of SOI CMOS micro hotplates for a high temperature resistive gas sensor (max. 350°C) [Udr01].

- Sheng et al. report on a CMOS compatible integrated gas sensor using maskless tin oxide sputtering. First results are shown on hydrogen (around 1000 ppm).

But up to now they did not integrate on-chip electronics to drive the sensor.

2.3.4 Commercially available SnO$_2$ gas sensors

There is only a small number of companies who sell single semiconducting gas sensors. The most sensors are sold with whole instruments to serve a special application. These instruments may also include sampling unit, electronics, evaluation units, etc.

In the following commercial available single sensors and sensor systems are mentioned.

2.3.4.1 Single sensors

The first semiconductor gas sensor was developed by Seiyama et al. in 1962 [Sey62]. N. Taguchi patented different configurations and embodiments of this device [Tag62][Tag70], which were already mentioned in the introduction (chapter 1.1). The sensor can be mounted in a TO-like socket, thus final packaging can contain a filter e.g. charcoal. The Figaro company distributed this sensor and they still sell thick film SnO$_2$ sensors but now on planar substrates [Fig] [Fig95], which were already mentioned in the introduction and are described in detail in chapter 3.1.2.1.

Besides Figaro, Fis (Japan) [Fis] and Capteur - now City Technology - (United Kingdom) [Cit] produce thick film sensors with planar design. The three companies are one the main distributors of single SnO$_2$ gas sensors. A uncompleted list of SnO$_2$ gas sensor vendors is given in Table 5.

Table 5: Selection of vendors of SnO$_2$ gas sensors.

American Sensor Inc. SNIFF	American Sensor Inc. SNIFF, Toronto Canada
Capteur	Capteur, Abington, United Kingdom
Figaro	Figaro Engineerings Inc., Mino Osaka, Japan
IL Metronic	IL Metronic Sensortechnik GmbH, Illmenau, Germany
Mircrosens SA	Microsens, Neuchâtel, Swizerland
MiCS	MicroChemical Systems SA, Corcelles, Switzerland
Nemoto	Nemoto & CO., Ltd, Suginami-ku, Tokyo, Japan
Pewatron	Pewatron, Wallisellen/ZH, Switzerland
Siemens Matsushita	Siemens AG, München, Germany
UST	Umwelt Sensor Technik, Geraberg, Germany

Companies like Bosch and Siemens develop currently gas sensor mainly for automotive application but mainly with other types of sensitive material such as TiO$_2$ [Fle97][Ing95].

Motorola and Microsens fabricated micromachined gas sensors with sputtered active layers. A couple of years ago they ceased their activity in sensors to start a joined venture: MicroChemical Systems (MiCS, [Mic]).

The middle picture in Figure 16 shows schematic drawing of type of micromachined sensor sold by MiCS respectively Motorola. On the right hand side the packaging of this micromachined sensor is shown which represents the typical way of packaging that can also be found for sensors on ceramic substrates. The sensor is glued to the socket (mostly TO) and the electrical contacts are bonded to the pins. A mesh is mounted underneath the charcoal filter to prevent a contamination of the sensitive layer. A nylon cap equipped with a mesh to allow the gas influx completes the whole. On the left hand side a photograph of an encapsulated sensors - here Figaro sensors - is shown.
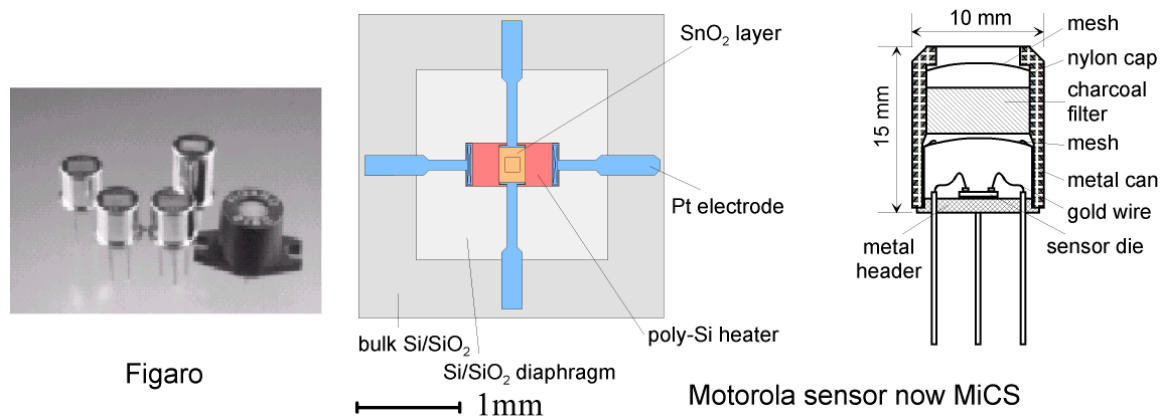
Figure 16: The left picture shows the encapsulated Figaro sensors [Fig] mounted on TO sockets. In the mid a schematic drawing of the microsensor distributed by MiCS is shown [Mic]. The right picture gives an image of the packaging of gas sensors.

2.3.4.2   Sensor systems

One big disadvantage of semiconductor gas sensors is their barely existing selectivity. To overcome this, instruments are offered equipped with sensor arrays consisting of differently sensitive semiconductor sensor or sensors of different sensing principles, so called hybrid systems. Most of the sensor systems – often called "Electronic Noses" – comprise commercial available gas sensor already mentioned above. A uncompleted list of distributors of sensor systems are:

- MOSES II, 8 Figaro sensors (hybrid system) [App]
- VOC series, 4 Figaro sensors (hybrid system) [App]
- AlphaMos Fox Series, 4 – 24 different sensors (hybrid system) [Alp]
- Airsens Analytics [Air]
- RTS Rostock & EADS SamSelect (hybrid system) [RTS]

In hybrid systems other detection principles like quartz crystal microbalances (QCM), electrochemical cells, surface acoustic wave (SAW), mass spectrometer (MS), etc. are used.

Furthermore, some sensor arrays do not consist of single sensors. For example, the KAMINA system developed at the University of Karlsruhe is a micro-system that comprises a field of 38 multi-layer sensor elements, which are attached on a 100 mm^2 oxidized silicon substrate [Gos01]. SnO_2 as well as WO_3 is used as sensitive metal oxide and SiO_2 as membrane material. Due to different inhomogeneous SnO_2-coatings of few nanometers and/or inhomogeneous heating the initially uniform sensor element, get different gas selectivity.

2.3.5 Improvements of gas sensors

The possibilities to improve the performance of SnO_2 gas sensors are manifold. The main are:

- Doping
- Grain characteristics influenced by calcination and grinding [Kap01]
- Operation temperature [Kap01]
- Temperature cycles [Hei99]
- Filters [Sch98]

In the following the most important − the doping − is explained in more detailed. Additionally, the most sensors used for carrying out the measurement of his theses are doped SnO_2 sensors. It will be shown in the results that the doping has a strong influence on the sensing of the different sensors.

 The other possibilities for sensor performance enhancement will be handled shortly.

2.3.5.1 Doping of SnO_2 gas sensors

Dopants are additives, which are added to change the charge carrier density in the bulk, as it is the case for classical doping in Si technology. Typically small amounts of precious metals or metal oxides are often added to enhance the sensing properties [Yam91], [Amb93], [Duk87], [Col91]. These additives can affect the sensing behaviour of a gas sensor significantly. They can result in faster response and recovery times, in an enhancement of sensitivity or selectivity, in a smaller drift or in a better reproducibility. In this work sensors doped with Pd and Pt are used. Another typical doping material is gold (Au). The preparation of doped sensitive layers was already mentioned in chapter 2.3.1 and 2.3.2.

To explain the influence of the dopants on the semiconductor two models are commonly used. Both models assume that small doping crystallites are located on the surface of a much bigger

grain of tin dioxide. The distribution of these small dopant particles on the surface is assumed to be more or less homogeneous.

The first model is called the spillover or catalytic effect. In this case, the catalyst facilitates the activation of certain gas particles, e.g. the dissociation of oxygen or hydrogen. Then the activated reactants reach the semiconductor, where the final reaction takes place. Due to spillover, reactions can be accelerated and shorter response time and larger sensitivity can result. If a given catalyst facilitates the activation for only a few gases, a higher selectivity can be obtained. Well-known examples for spill-over are the spill-over of hydrogen and oxygen from metal catalysts onto the semiconductor support [Bia75, San71, Ser73, Bat75]. In the case of the spill-over of oxygen and hydrogen due to the presence of Pt, an explanation for the lowering of the activation energy can easily be found. The bonding energy of Pt atoms to hydrogen atoms is not so different from the bonding energy of one hydrogen atom to another. Therefore comparably little energy is needed to dissociate hydrogen molecules. Similar arguments hold for Pt and O_2. Consequently, the catalyst reduces the energy normally needed for dissociation to a great extent. The subsequent spillover onto SnO_2 is possible after breaking the rather weak bonds between hydrogen or, oxygen and Pt, respectively. Hence, the presence of the catalyst changes the initial dissociation process with rather high activation energy into a process with two lower energy barriers and hence increases the probability of the process.

The second model is the so-called Fermi energy control. In this case the close electronic contact of the semiconductor with the catalyst dominates the sensor signal. Oxygen species at the surface of the catalyst trap electrons, which are refilled by electrons from the semiconductor. A depletion layer inside the semiconductor and a band bending result. Under the influence of the ambient gas atmosphere, the catalyst particles become oxidised. The stoichiometry of the catalyst oxide (MO_{2-X}) hereby depends on the composition of the ambient gas atmosphere and so does the position of its Fermi level. At equilibrium, the Fermi level of the catalyst and the semiconductor are at the same height. Since the gas reacts via the catalyst with the metal oxide, the chosen catalyst can strongly change the selectivity of pure tin oxide. The possible influences of catalysts are illustrated in Figure 17.
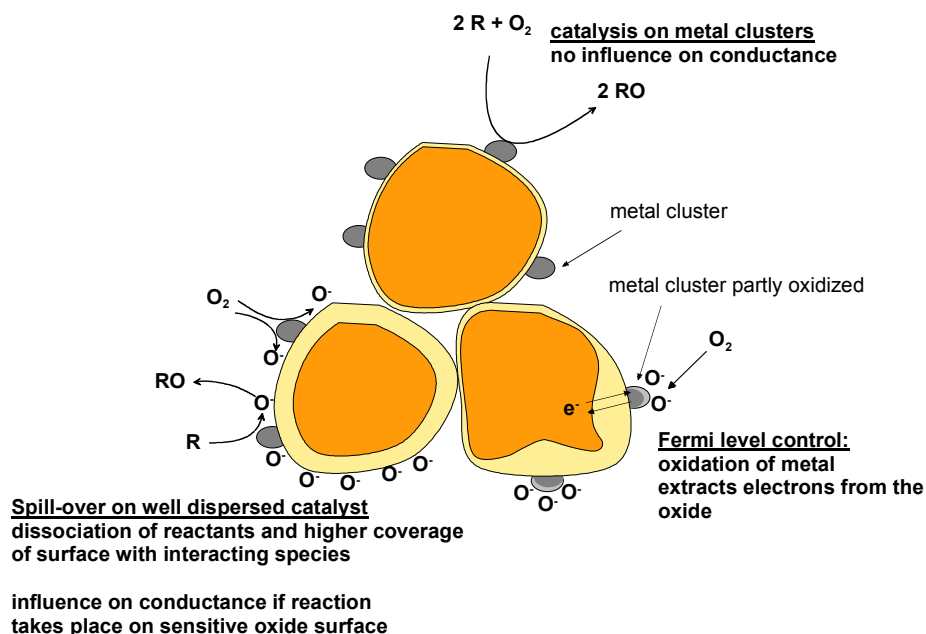
Figure 17: *Effect of doping:*
Top: Catalysis on metal clusters. The gas reaction takes place entirely on the cluster. Hence, the conductance remains unaffected.
Left: Spill-over: Metallic clusters promote the dissociation of certain ambient gases. The reactive particles reach the tin dioxide surface, where the reaction takes place. The conductance is affected due to this.
Right: Fermi level control. Metallic clusters are partially oxidised in the gaseous atmosphere. The ambient gases affect the stoichiometry. Changes in the Fermi level position of the clusters change the depletion layer and the band bending inside the tin dioxide.

2.3.5.2   Others

The SnO_2 grains size can be adjusted by calcination parameters and grinding. Calcination, the initial heat treatment the precursor (hydrated SnO_2) undergoes provides thermal energy, which enables the growth of SnO_2 particles. An increase in calcination temperature increases monotonously the mean grain size starting from 4 nm at 250°C to 110 snm at 1000°C (detailed information in [Kap01]). In addition, the FWHM (Full Width Half Maximum) of the grain size distribution increases monotonously with calcination temperature. A longer calcination time results in larger grains and a broader grain size distribution.

Grinding results in a reduction of the grain size, too. The smallest grains are obtained by grinding before and after the calcination.

Smaller grains result in a bigger surface area and resistance measurements show that the resistance in air increase with decreasing grain size [Lu00]. Because of the increased surface area, the sensitivity towards test gases is increase, too.

The operation temperature plays an important role for the reaction of test gases with the SnO_2 surface. Generally, the sensitivity to polar gases like CO is higher at temperatures between 250°C – 300°C [Kpap01], whereas the optimum operation temperature of hydrocarbons like CH_4 is higher, around 350°C – 400°C [Kap01]. The effect of operation temperature is generally bigger than the influence of the pre-treatment [Wil99].

The modulation of the temperature enables the possibility to take advantage of the temperature dependent sensitivity of semiconductor gas sensor by modulating the temperature of a single sensor. This is mainly done with micromachined sensors because of their smaller size and therefore faster temperature adjustment [Hei99][Jae99][Lee99]. A special signal evaluation routine is required to extract the data out of the transient response of the sensor.

3   Experimental Section

3.1   Material preparation and sensor fabrication

In order to discriminate between the components of a gas mixture, one generally needs to use arrays, id est combinations of sensors with different characteristics, which means different sensing materials. Their preparation is described in detail in [Kap01]. In the following, only a short overview is given.

The sensor fabrication, which is summarised in Figure 18, can be divided in two main parts: the preparation of the sensitive material/doped SnO_2 powder and the fabrication of sensors based on these powders.
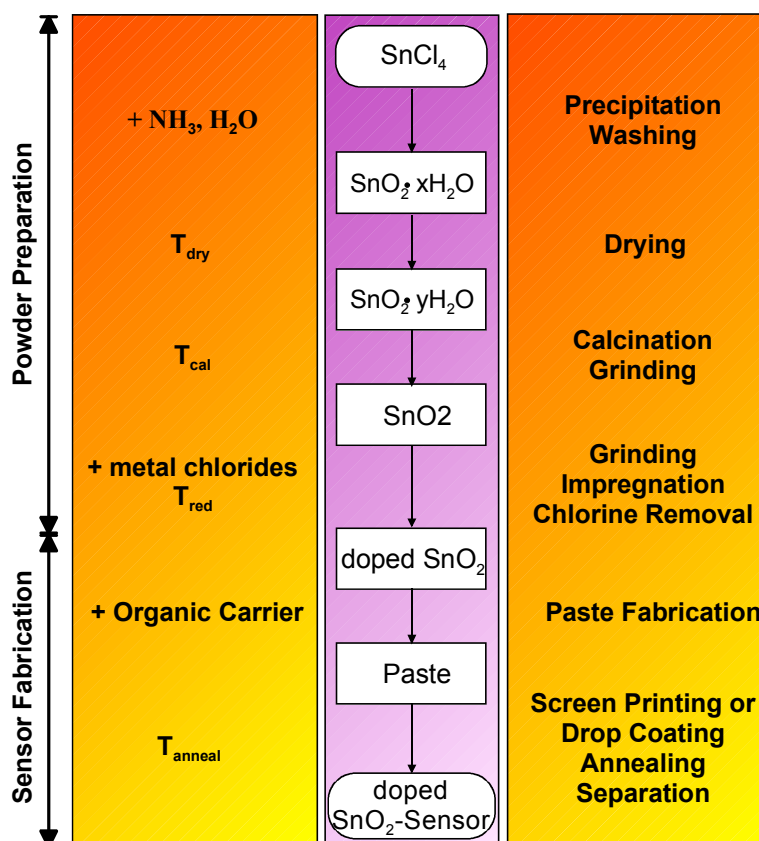
Figure 18: Flow chart summarising the preparation of SnO_2 thick film sensors based on a modified sol-gel route. The influence of various preparation parameters (calcination, grinding treatment, doping and annealing) on the material and sensor properties is big and detailed information is given in [Kap01].

3.1.1   Powder preparation

The preparation of the sensitive material is done in two steps. Firstly, the precursor – hydrated tin dioxide – is obtained by precipitation of ultra-pure, water-free tin chloride (Merck). For doing so, an aqueous, ice-cooled solution of $SnCl_4$ is added in a controlled manner to an ice-

cooled, aqueous solution of NH_3. The cooling of both aqueous solutions has the role of reducing the reaction speed and in this way to ensure the obtaining of a homogeneous nano-sized precipitate. In order to remove the remaining chlorine and ammonia, the precipitate is thoroughly washed several times with bi-distilled water (Millipore Milli-Q PF Plus; resulting water resistivity = 18.2 MΩcm). Thereafter the suspension is centrifuged (Hettich Universal II) and dried at T_{dry} = 80°C in a drying oven (Heraeus UT12). After the last step, the precursor – hydrated SnO_2 - is obtained.

The second step is the calcination of the precursor in a furnace (Heraeus ROK/A 6/30) at elevated temperatures (T_{cal} = 250°C to 1000°C) for 8h. It removes the remaining water, enables the grain growth and forms SnO_2 powder with a well-defined grain size distribution. The resulting SnO_2 powders usually contain large agglomerates, which can be scaled down by grinding.

Metal oxide sensors are usually not very selective, so catalysts were used to increase their selectivity. $PdCl_2$ and $PtCl_4$ were used to introduce precious metals as dopants. The addition of catalysts, which is often referred to as doping, is performed by impregnation of calcined SnO_2. In this case, the tin dioxide powder, an appropriate amount of metal chloride and water are thoroughly mixed by means of a magnetic stirrer (IKA RCT basic). Since the precedent calcination determines the final grain size of the compact SnO_2 grains, the dopant will mainly be located at the surface of the individual SnO_2 grains. A final annealing step (1h at 450°C in the furnace Heraeus ROK/A 6/30) converts the metal chlorides into metals.

The preparation of the paste was the same for all types of sensor investigated in this work. The differences are in the substrate – alumina or micromachined – and therefore in the transfer of the paste.

3.1.2 Sensor Substrates

Measurements with sensors based on two different types substrates were performed, id est. alumina based substrates and micromachined substrates.

3.1.2.1 Alumina substrates

The substrates are based on 96% Al_2O_3. The size of the tile is 2 x 2 inch with a thickness of 0.7 μm and on which tile up to 20 individual sensor substrates are present with dimensions shown in Figure 19. They are equipped with Pt or Au electrodes of different style (interdigitated or gap geometry) on the front side for measuring the sensor resistance and Pt heaters on the back for keeping the sensors at the operating temperature (see Figure 19). The geometry of the electrode structure was adapted to the application; where lower resistances

were needed, the interdigitated electrode solution was chosen and in the case when a higher value of the resistance was desired the gap solution was used.

In this work, alumina substrates with interdigitated Pt electrode are referred as type 1. Type 2 has a gap configuration of Pt electrodes. The substrates with interdigitated Au electrodes are referred to as type 3 alumina substrates.
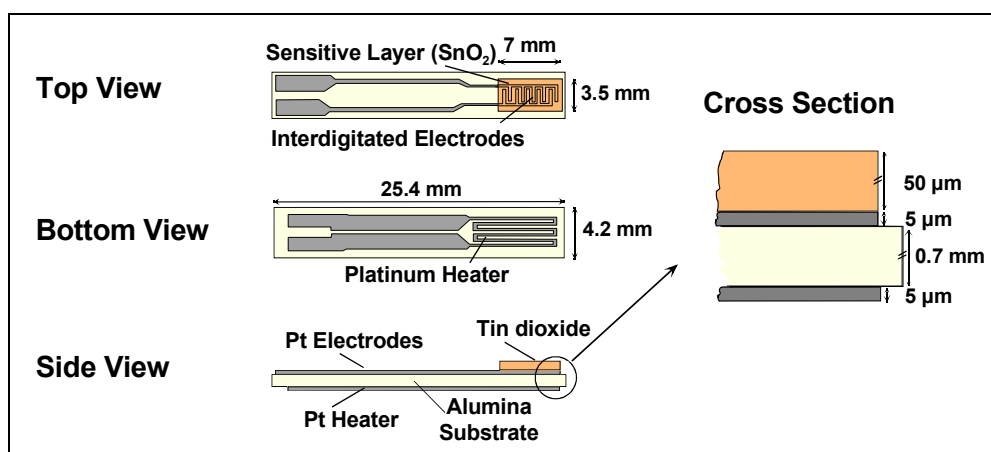

Figure 19: Example of a layout of the planar alumina substrate with Pt electrodes and interdigitated Pt heater (type 1). The SnO₂ layer is printed on top of the interdigitated electrodes. The heater on the back keeps the sensor at the operation temperature.

3.1.2.2   Micromachined substrates

The micromachined metal oxide gas sensor substrate is realized in an industrial CMOS process with the aim of low cost at high volume production.

The newly developed CMOS sensor substrate consists of a membrane, heater, temperature sensors, electrodes and electronics. The left micrograph of in Figure 20 shows a typical sensor substrate used in this thesis; on the right, a closer look of the membrane is presented. The Eidgenössische Technische Hochschule in Zürich, Switzerland (ETHZ) realized the substrate design and the manufacturing took place at Austria Mikro Systeme (AMS) in Graz, Austria.

The dielectric membranes are 500 by 500 μm in size with a heated area of 300×300 μm^2; the dimensions of the active/heated area of the membrane are ensuring enough space for realizing the most appropriate electrode structures. The membrane was released by anisotropic KOH – back-etching. A Si-island structure was realized underneath the heater by using an electrochemical etch stop technology. Different heated area geometries were realized: square, octagonal, and circular. The latter was designed in view of the circular symmetry of the sensing layer, which characterizes the drop deposition technology.
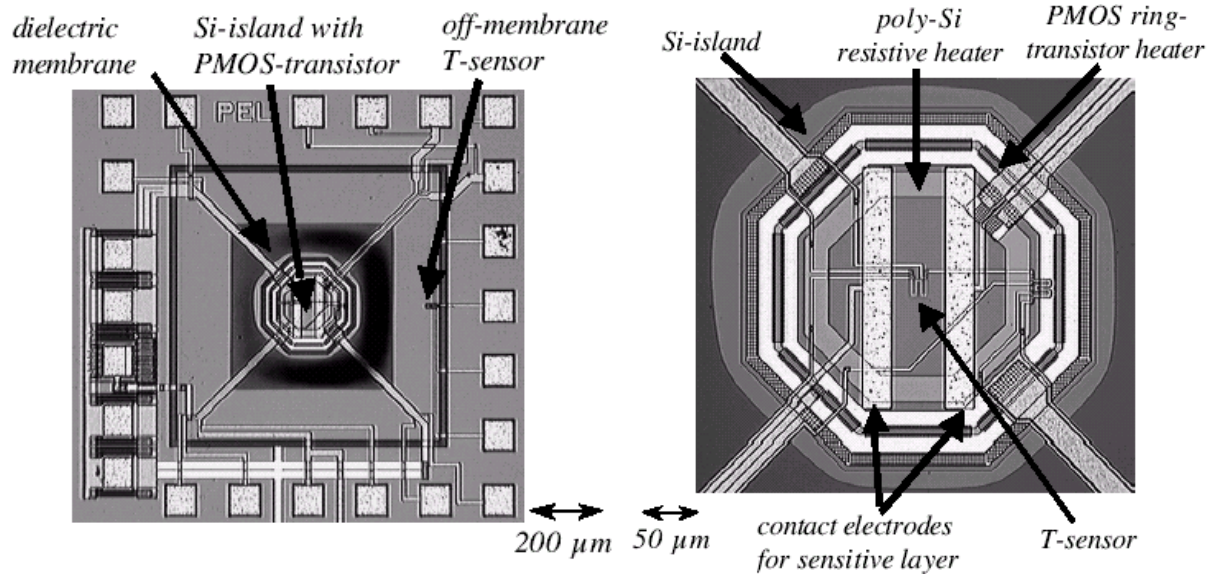
Figure 20: Micrograph picture showing a CMOS micromachined sensor. The left picture shows the chip with membrane and PMOS-heater. On the right one a close-up of the central membrane part is shown with the integrated functional elements [Gra02].

The material used for the resistive heater is polycrystalline Si. Different meander and ring-shaped heater structures with an appropriate electrical resistance were designed on the membrane. The maximum operating temperature of 400 °C was achieved with the standard supply voltage of 5.5 V. Several different temperature sensors have been included (Al, poly-Si and n-Si diffusion resistors) for a resistive temperature measurement.

The first layer of the electrodes was realized by using the proper Al-metallization of the CMOS process. The nitride passivation was opened in the electrode area to ensure tight attachment of the sensitive layer. Interdigitated electrodes and pairs of parallel electrodes with varying center-to-center distance were used.

To prevent the oxidation of the aluminum electrodes during the annealing, an additional metal interface layer had to be added. Two different methods – a thick film and a thin film deposition – were used: By electroless Ni/Au plating (thick film deposition) a 5 μm Ni film is piled with a 50 nm thick Au-layer on top. The other is the deposition of thin films by PVD or sputter deposition. The used metals were gold (Au), rhodium (Rh) and platinum (Pt).

The CMOS sensor substrate is a new development. Therefore, different chip designs had been produced to find out the best solution. The sensor performances of these prototypes are characterised in this work.

3.1.3 Sensor Fabrication

In order to deposit a continuous sensitive SnO_2 layer, the SnO_2 powder was transformed into a homogeneous paste by mixing with an organic carrier.

For the alumina substrates, screen-printing (EKRA microtronic II) is used to transfer the paste. Hereby a rubber squeegee presses the paste through the undeveloped part of the screen, which works as a mask for the paste transfer onto the substrate. By this method SnO_2 layers with a thickness of a few micrometers to around 100 μm, depending on the chosen screen, the paste viscosity and the screen-substrate distance, can be adjusted

In the case of micro-machined sensors, the paste deposition has to be performed in a way, which avoids damaging the sensor. Accordingly, a low-stress method, which allows the reproducible deposition of single paste droplets onto Si-based membranes, has been applied.

After screen-printing/drop coating, the substrates are kept at room temperature for 1 h to allow the paste to settle. Subsequently, the substrates are placed in a drying oven (Heraeus UT12) set at 80°C. Finally, they are inserted into a moving belt oven (Centrotherm Centronic DO 1600-60-D5). During the final annealing ('firing'), the organic additives of the film are removed and the layer becomes mechanically stable and firmly bonded to the substrate. The moving belt oven has four individually operated heating zones. The temperature of each heating zone, the speed of the moving belt and the gas flow inside each heating zone creating the ambient gas atmosphere around the substrate, can be individually regulated. The firing profile was adjusted in such a way that a gradual heating from room temperature to the maximum firing temperature (in the range of 400°C to 700°C) and a gradual cooling back to room temperature was achieved. The velocity of the moving belt is adjusted to allow the substrates to stay in the maximum temperature zone for 10 minutes. Filtered, compressed air or nitrogen was chosen as the gas atmosphere for the firing step.

3.2 Measurement set-ups

At the beginning of this chapter a description of a general set-up for gas sensor measurement is given. The modifications to solve certain measurement requirements are listed at the end.

The measurement set-ups consist of a gas mixing bench to provide the different measurement gases, measurement chambers which contain the sensors, electronics to drive the sensors and system and additional instruments for monitoring different compounds like oxygen, water, etc.

3.2.1 Gas mixing bench

In order to test and calibrate gas sensors, they are exposed to gas mixtures, which mimic the actual ambient gas atmospheres corresponding to specific applications. The gas mixtures are obtained by using gas-mixing benches typically consisting of a combination of computer controlled mass flow controllers (MFCs) and computer-controlled valves (see Figure 21). By means of, e. g. the illustrated 8-channel gas mixing station, up to 6 test gases can be combined with dry and water vapour saturated synthetic air (usually used as carrier gas).
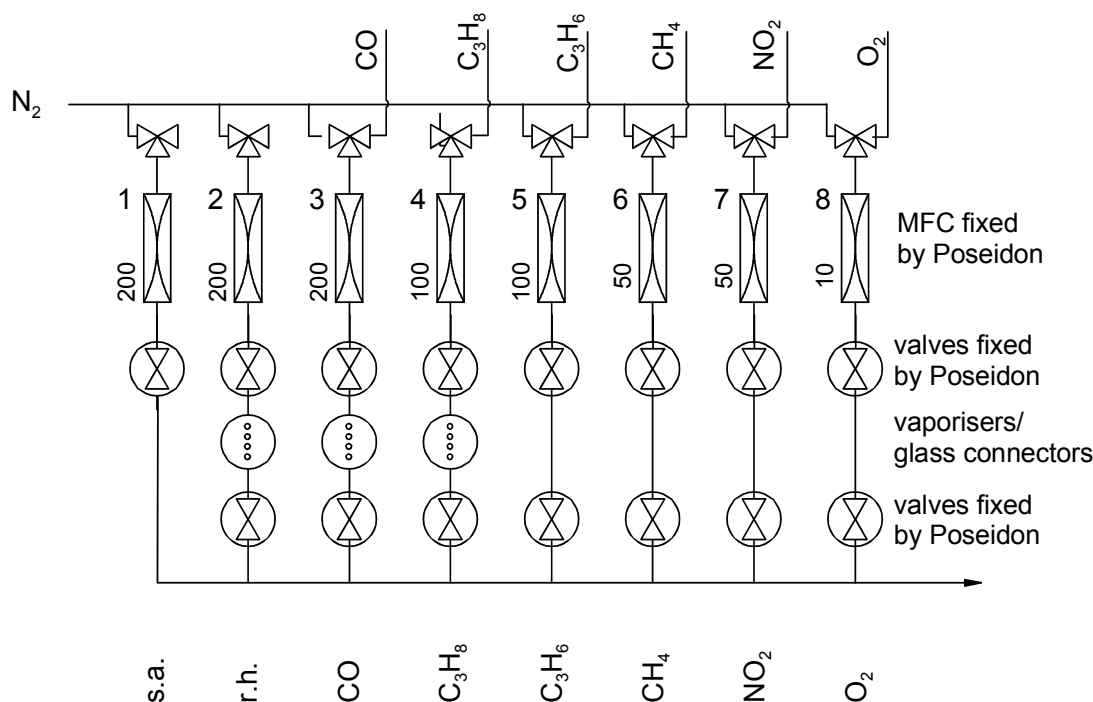

Figure 21: *Schematic picture of a eight-channel gas mixing bench. Test gases are either introduced from gas cylinders (CO, C_3H_8 and CH_4, etc.) or added by flowing nitrogen (N_2) through vaporisers. The latter method is also used to adjust the relative humidity (r.h.), evaporated organic compounds or dry the test gas. Two rows of electromagnetic valves prevent unintended diffusion of test gases.*

The gas mixing bench is operated by a home-made software programme called POSEIDON. The mass flow controllers and the electromagnetic valves are controlled via D/A card (PCL-727). An A/D card (PCL-812 AD) is used to check the performance of the gas mixing bench by recording the actual gas flows through the mass flow controllers. The tubing of the gas channels consists mainly of electrically polished stainless steel pipes; the rest of the tubing, i.e. the tubing of the channels, which are dedicated to highly reactive gases (e.g. NO_2), are made out of Teflon (PTFE, polytetrafluoroethylene).

The gas flows through individual channels are adjusted by means of computer controlled mass flow controllers. Upstream to rows of electromagnetic valves are interconnected via either glass tubes, bubblers or u-shaped glass vessels. The latter are so-called vaporisers,

which are filled with an adsorbent with a high specific surface (Chromosorb P-NAW, Macherey-Nagel) or a dehumidifying material (i.e. molecular sieve). The two types of connectors can easily be interchanged and therefore a maximum flexibility is ensured.

In the case where test gases are injected directly from gas cylinders, glass tubes are used as connectors. Otherwise, carrier gas is conducted through temperature-controlled vaporisers, which are filled with the components, in liquid phase, the vapours of which are test gases and adsorbent. In the latter case, the carrier gas becomes saturated with the vapours and the saturation concentration depends on the temperature at which the vaporisers are kept. This principle is also used for humidifying synthetic air but usually a bubbler filled with water is used because of his bigger capacity.

The test gas concentrations are adjusted by controlling the ratio of the test gas flow to the total gas flow. For the direct gas introduction from cylinders, the gas concentration of the test gas in the gas cylinder is at the basis of calculations. The temperature of the vaporiser determines the vapour pressure of the analyte and allows from the concentration calculation for the other case.

By means of two rows of computer controlled valves the unintended diffusion of test gases is prevented. If the flow through a mass flow controller falls below 5% of its maximum value, the linearity of the flow controller is no longer guaranteed. In this case, the computer closes both valves. Hereby the row of valves which is further away from the mass flow controllers prevents the diffusion of analyte into the gas flow and the back diffusion of gases from the gas flow into the vaporisers; the other row of valves ensures that no pressure is built up in the liquid-filled vaporiser due to an unintended gas flow through the MFCs.

3.2.2 Sensor positioning in the measurement chambers

3.2.2.1 Alumina substrates

Tin dioxide sensors (SnO_2) based on alumina substrates are used for two investigations: For studying the sensing characteristics in low oxygen concentrations and high humidities and the discrimination between CO and CH_4. In the first investigation, two brass measurement chambers were equipped with two type 1 and two type 2 sensors (platinum electrode) of various doping. Five sensors of type 3 (gold electrode) were used for sensors discriminating CO and CH_4 mixtures. They were mounted in two Teflon chambers, which can hort up to three sensors.

3.2.2.2   Micromachined CMOS sensors

The newly developed micromachined CMOS sensor chips were bonded on 28DIL sockets. The 28DIL socket was chosen in order to measure up to14 different features on the sensor chip, id est. measuring the temperature on the membrane at various places on the sensor chip. For the gas testing, an aluminium measurement chamber was designed that holds up to four CMOS sensors on DIL28 sockets. The wires for heating and read out were soldered on separate DIL28 sockets which were plugged on the chamber.

3.2.3   Sensor heating

Tin dioxide sensors are operated at elevated temperatures between 200°C and 400°C. The different sensor types require different electronics and instruments for heating the sensors.

3.2.3.1   Alumina substrates

To keep the sensor of type 1 and 2 at the operation temperature (200°C – 400°C) a power supply (Hewlett Packard DC Power Supply E3610A) is used to ensure a constant voltage drop over the platinum meander on the rear side of the alumina substrate. In order to calibrate the platinum heater, i.e. to obtain the relationship between the applied voltage and the thereby adjusted temperature, an infrared pyrometer (Maurer KTR 2300-1) was used. The measurement set-up is sketched in Figure 22. The pyrometer detects the infrared emission from a measurement spot of about 1 mm² and calculates, using the specific emission coefficient ε ($\varepsilon_{SnO_2} = 0.75$) of the material, the temperature of the sensitive layer. The pyrometer can be used for detecting temperatures from 200°C to 500°C. The resulting relationship between the temperature of the sensing layer and the voltage applied on the heating resistance is given in Figure 22.

In the case of the alumina substrates with Au electrodes (type 3), a special electronic circuitry was used to keep the sensors at a constant temperature.
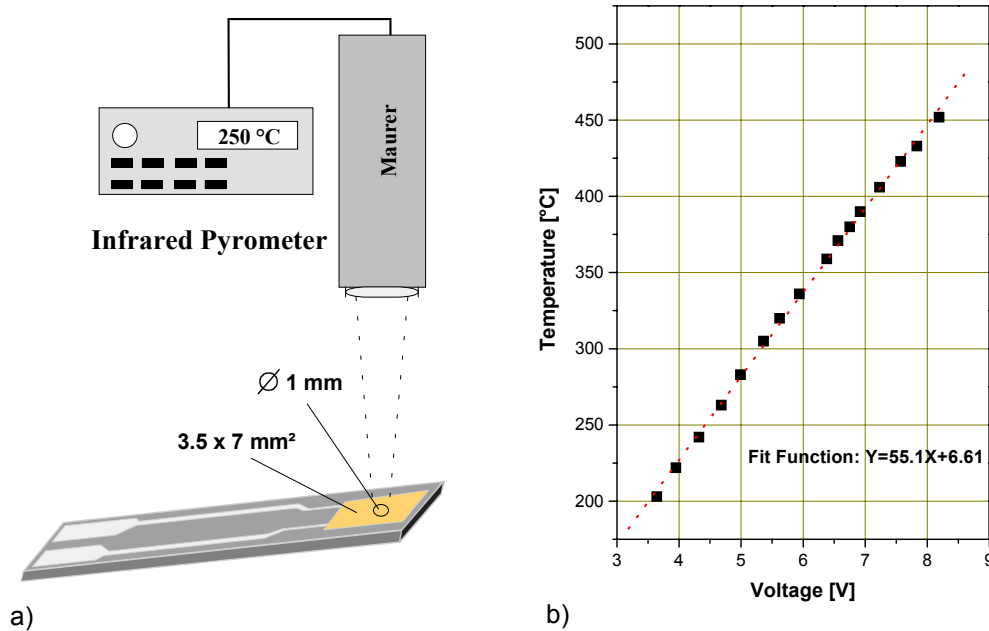
Figure 22: *Calibration of the Pt heater. In a) the measurement set-up is sketched. The resulting calibration curve can be nicely approximated by a linear fit (b).*

3.2.3.2   Micromachined CMOS sensors

The measurements were carried out with two different kinds of microsensors: with circuitry and without circuitry.

The CMOS-chips without circuitry were connected to a reference current of $-500\,\mu A$ or $-50\,\mu A$ depending of the material of the thermo elements (polycrystalline Si or aluminium). The CMOS-chips without circuitry − later called test structures - were heated by a voltage source, supplying voltages between 1.2 and 4.8 V, according to the desired temperature.

The CMOS-chips with circuitry were connected to supply voltage (Vdd) of 5.5 V (Hewlett Packard Dual Output Power Supply HP E3620A, $0 - 25$ V $0 - 1$ A). A reference voltage of $1.24 - 1.73$ V (Knick DC Calibrator S252) was applied to heat the membrane. A reference current of $-10\,\mu A$ was also applied (Knick DC Calibrator J152) for the circuitry. It is recommended to use a stable voltage source because the membrane temperature is sensitive to small changes of the reference voltage.

The sensor chips were designed with four thermo elements on the membrane chip to be able to measure the temperature homogeneity of the membrane. Some are at the edge (number depending of the design) and one is in the middle of the membrane (see Figure 20). For the gas sensing measurements, the one in the middle of the membrane was chosen as temperature sensor for both types of CMOS chips. The output of the temperature element is a voltage drop that was recorded with the Keithley DMM199.

The ratio of the decrease of the resistance (ΔR) and the resistance R at operating conditions (membrane heated) is calculated with the help of the Ohm's law (equation 16). U_0 is the measured at a referent current of – 500 µA respectively –50 µA, U(T) is the voltage drop of the heated membrane (U_{heat} = 1,2 – 3.4 V) and T_0 is the room temperature.

$$\frac{\Delta R}{R} = \frac{U(T) - U_0}{U_0} \tag{16}$$

For the different is the material of the temperature element – aluminum (Al) or polysilicium (Poly 1) – the temperature was calculated according equation 17 or 18.

Poly 1
$$T = T_0 + 1025.4 \cdot \left(\frac{\Delta R}{R}\right) - 309.9 \cdot \left(\frac{\Delta R}{R}\right)^2 \tag{17}$$

Al
$$T = T_0 + 378.5 \cdot \left(\frac{\Delta R}{R}\right) - 15.3 \cdot \left(\frac{\Delta R}{R}\right)^2 \tag{18}$$

In Table 6, the sensor temperatures are calculated for the different applied heating voltages. For the first warm up one has to wait a day to get a stable value for U_0, which also show a small (linear) drift over time.

The temperature is stable for the circuitry controlled sensors; the sensors without cicuitry show a daily temperature fluctuation, which can be related to the changes of the room temperature. The amplitude of the fluctuation is, e. g. for sensor Pt III L/B, around 3°C.

Table 6: Necessary data for calculating the sensor temperature. V_0 – voltage drop at the temperature sensor on the membrane - is measured at room temperature.

Sensor	type	U_0 [V]	U_{heat} [V]	U_T [V]	T [°C]
Au2 is	Al	0.00655	3.2	0.01064	256°C
Au3	Poly	0.59507	3.2	0.7440	262°C
Pt1	Al	0.00650	1.2	0.1040	247°C
Pt5	Poly	1.391	U_{ref}: 1.54	1.8002	300°C
		1.4268	V_{ref}: 1.64[1]	1.8004	270°C
Rh3	Poly	1.332	V_{ref}: 1.54	0.720	298°C
Au II 8	Al	0.006764	3.2V ??	00.010579	279°C
NiAu 3+4	Poly	1.335	U_{ref}: 1.54	1.713	285°C
Pt II 5+6	Poly	1.4472	U_{ref}: 1.64	1.8395	273°C

---

[1] The instruments for the reference current and voltage as well as the way of grounding the sensor were changed.

Pt II #19	Al	0.006489	3.20	0.011177	283°C
Pt III CS1.2A	Poly	1.231	1.31	1.534	252°C
		1.237	1.45	1.614	302°C
		1.237		1.69	352°C
Pt III CS1.2B	Poly	1.293	1.37	1.628	260°C
		1.320	1.50	1.703	302°C
		1.320		1.802	352°C
Pt III L/B	Poly	0.5747	3.00	0.7132	256°C
		0.5982	3.45	0.7790	300°C
		0.5982	3.95	0.8160	351°C
Pt III R/A	Poly	0.5550	3.00	0.6913	250°C
		0.5579	3.43	0.7320	301°C
		0.5579		0.7880	352°C

3.2.4 DC measurements/Sensor read out

The typical characterization technique for metal oxide sensors is the measurement of resistance. For measuring multiple sensors in one run, digital multimeters (DMM, e.g. Keithley DMM 199 or Keithely DMM 2000) were used. The measurement principle of the DMM is the following: a reference voltage drops over a reference resistance and the sensor resistance. The voltage drops over the two resistances are measured and based on the voltage ratio, the sensor resistance is determined. Due to the limited resolution of the A/D converters, different reference resistances are used for different measurement ranges. DMMs are either operated in the auto-range mode or in a fixed resistance range. The advantage of the auto-range mode is that sensors with a large dynamic resistance range or a collection of sensors with very different sensor resistances can be measured. The drawback is that if the resistance range is changed during the measurement, so the used reference resistance changes. Also in which the voltage drop over the sensor changes abruptly. The sensors usually show non-ohmic behaviour. So step-wise changes appear in the measured sensor resistance if the measurement range changes. In order to avoid that such effects are influencing the results, the sensors were measured in a fixed resistance range.

A computer was used to control the gas composition and to record the resistance and various data via a DMM and IEEE card.

3.2.5 Set-up modifications

3.2.5.1 Measurements monitoring oxygen and water

The set-up for monitoring oxygen and water consists of a gas mixing system, two measurement chambers, an oxygen analyser (Advanced Optima Magnos 106, ABB Automation Products, Germany), a hygrometer (Model DS1000, α-Moisture Systems, UK) and a CO_2 sensor based on an optical cell (Figure 23). The carrier gas was nitrogen (with a purity of at least 5.5). The remaining six channels were used for CO, propane, and oxygen, which were provided by bottles/tanks of pressurized gases.

The gas is purged through two brass measurement chambers and the stainless steel measurement chamber of the hygrometer, placed one after the other. The hygrometer is a capacitive solid-state sensor with a measurement range spanning between $-80°C$ and $+40°C$ (equivalent to $0.54\,ppm_v - 78584\,ppm_v$ at $25°C$). Subsequently, the gas runs through the oxygen analyser, which measurement principle is based on the deflection of the paramagnetic oxygen "wind" induced by a magnetic field. In the measurement range (0 - 5%, 0 - 15%) the accuracy was 0.5% of the measurement range, zero point drift 0,03% detection limit < 0.5% and repeatability 0.5%. Due to the zero point drift, the zero point was set every second week with nitrogen (purity 5.6). At the end of the line, the optical carbon dioxide (CO_2) sensor was installed. Due to its the limited sensitivity, reasonable signals (> 5 ppm) were detected only for high O_2 concentrations (> 50 ppm). The analogue outputs of all above mentioned instruments were recorded by reading them with the help of a Keithley DMM 2000.

The measurement set-up was constructed in a manner that allows to firstly purging either the sensor chambers or the H_2O and O_2 measurements instruments (Figure 23). All the tubing was out of stainless steel to prevent any diffusion. With this set-up it was possible to also estimate the effects of the sensors concerning O_2 and H_2O consumption or generation.
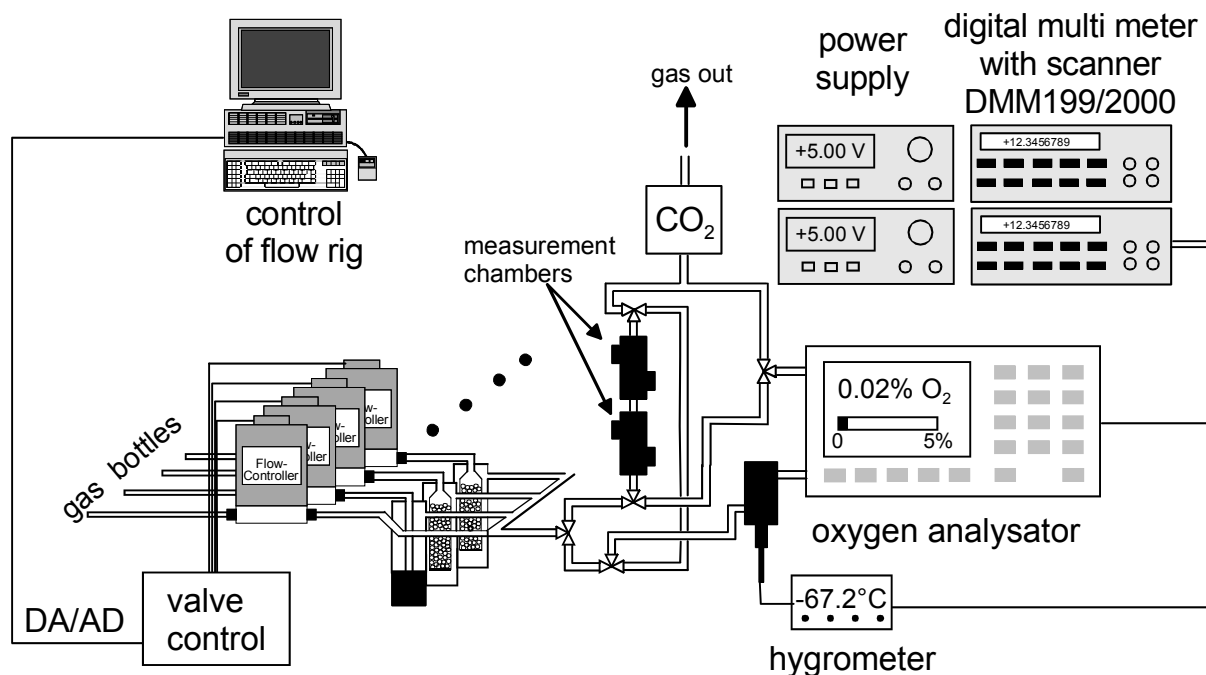
Figure 23: Measurement set-up for monitoring oxygen and water concentration before and after the measurements chambers. A gas mixing system, which is equipped with eight channels, provides gas. One with carrier gas in this case N_2 the second with a bubbler to humidify the carrier as and the other for test gases here CO and propane. The latter were equipped with a vaporizer filled with molecular sieve (∅ = 50 Å) to dry the gas. There are two ways to purge the gas: first through the measurement chambers each equipped with two sensors and than through the dewpoint meter and oxygen analyser and second through the dew-point meter and oxygen analyser and than through the measurement chambers. In the exhaust line, an optical CO_2 sensor was installed to monitor the originating CO_2.

3.2.5.1.1 Determination of the background

For the present work, the dependence of the sensor performance on O_2 and H_2O concentration is of special interest. When operating in the "absence" of both it is important to know the real background concentration. For its determination, the hygrometer of α-Moisture equipped with a capacitive alumina sensor was used to measure the H_2O concentration and the paramagnetic oxygen analysator measured the O_2 concentration. The zero point calibration was carried out by using N_2 as carrier gas (purity 5.6) and therefore an absolute determination of the O_2 concentration was not possible. One has also to add an offset because of the carrier gas (maximal 4 ppm) and small leakages- below the resolution of the instrument - of the gas mixing system. In what follows only relative changes will be given. The O_2 and H_2O background concentration of test gas bottles were measured for three different concentrations by purging the gas flow first through the measurement instrument and subsequently through the measurement chambers.

Figure 24 shows the O_2 concentration, the dewpoint of H_2O and the resistance of a 0.2% w.t. Pd doped SnO_2 sensor upon exposure to $0-500$ ppm CO (left side) respectively $0-100$ ppm C_3H_8 (right side) in "dry" and "zero-oxygen" conditions.
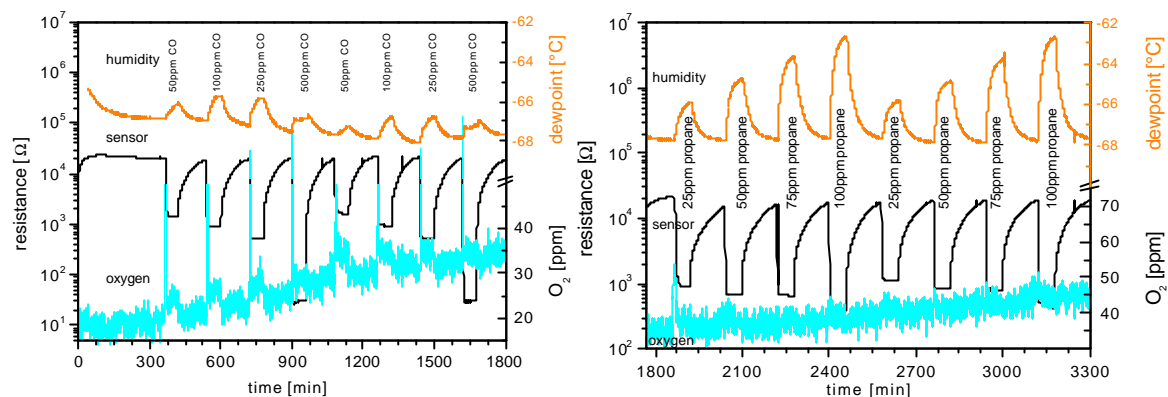

Figure 24: Determination of O_2 and H_2O concentration of the CO (left graph) and C_3H_8 (right) test gas bottles. The dew point of H_2O and O_2 concentration were monitored online in front of the measurement chambers. The sensor resistance of a 0.2% w.t. Pd doped SnO_2 thick film sensor is plotted to indicate the gas concentration.

It results that the CO bottle (1000 ppm) contains around 5 pm H_2O. A value of around 34 ppm H_2O was calculated for the case of C_3H_8 bottle (1000 ppm). The O_2 concentration could not be specified because the measured values are below the 5 ppm resolution of the instrument. The maximum changes in the water vapour concentration are 1.2 ppm for CO tests and 3.4 ppm for C_3H_8 tests.

3.2.5.2   High humidity measurements

The measurements were carried out at the Ford Research Laboratory. The gas mixing system build up there consists of 8 flow controllers (MKS) and the corresponding valves. Each of the two brass measurements chambers was equipped with two sensors. The read out of the sensor resistance was done every 2 s respectively 5 s by a Keithley DM199 driven by a Labview program.

For the measurements at high humidities, a Bronkhorst HIGH-TECH B.V. series CEM system was used to produce mixtures containing up to 5 g/h[1] of water vapour.

The abbreviation "CEM" stands for:

- "C" the control of a flow of gas mixture, gas, liquid or liquid/gas mixture.
- "E" the evaporation of a flow of liquid/gas mixture by means of a temperature controlled heating device.

---

[1] The maximum amount of water that can be vaporised by the system in one hour. The resulting maximum water vapour concentration depends on the adjusted flow.

- "M" the mixing of a gas and liquid (vapour).

The complete system is a combination of a mixing valve, a heating device, a liquid meter with control function and a mass flow controller (MFC) for the carrier gas (Figure 25). The mixing valve controls the liquid flow through the liquid meter. The complete system also incorporates a readout/control unit, including power supply for operation of the different "CEM"-system devices.

Liquid flow

MFC

Controlled Evaporator
Mixer
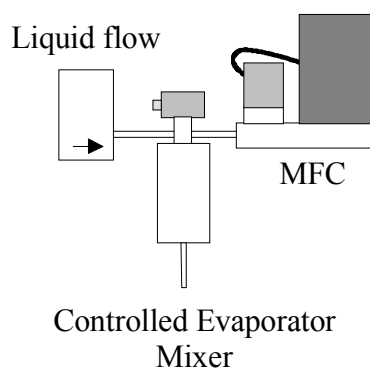
Figure 25: General set-up of a Bronkhorst HIGH-TECH B.V. series CEM (Control, Evaporation and Mixing) system to realise mass flow control of vapour and mixtures.

The operation principle was as follows. The water vapour was generated in the CEM System. The MKS mass flow controller provided a flow of high purity nitrogen (5.9) to the mixer (Figure 26). The water for the liquid mass flow controller (LMFC) was supplied from a vessel containing deionised water, pressurized with $1.4 - 2.8$ bar N_2. The system was filled and the valve on the evaporator opened to allow the gas to escape. The valve was open for 6 - 72 hours before the first use.

When operating the system the liquid reached the CEM system which is built up around 3 different parts; a control valve, a mixing device a heat exchange ring which heat is added to the mixture of fluids for vaporisation and furthermore to prevent condensation. The water was mixed with the gas and consequently evaporated. The flow provided by the gas mixing system (500 ml/min) was mixed with the humidified flow just behind the mixer at the outlet of the CEM system and got in the oven by a heated line.
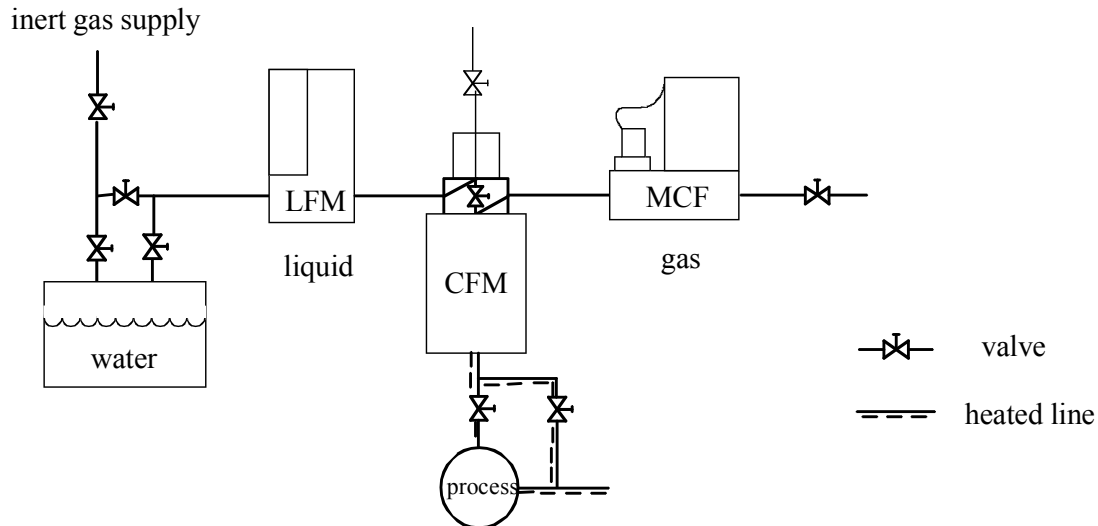
Figure 26: Schematic drawing of the evaporation system. The inert gas (N₂) is purred through the water reservoir and transports the water through the liquid mass flow controller (LFMC) to the mixer of the CEM.

To prevent condensation, made possible due to the high humidities (absolute 2.4 − 10%), the tubing was heated up to 60°C by using heating tape and the sensor chambers were placed in a thermo stated chamber (Environ Cab model 680 heated up to 50°C with an accuracy of about 0.2°C). In that chamber, the 1000 ml/min gas flow was divided by a rotameter into 800 ml/min and 200 ml/min separate flows. The gas flow of 200 ml/min passed the measurement chamber and went to the waste. The 800 ml/min was purged to a chilled mirror hygrometer from General Eastern (model SIM-12H with an M2 controller) to monitor the resulting humidity.

A 6-litre flask was added (Figure 27) after the evaporation system to smoothen out the spikes that were caused by quick changes in the dew point. Thus, the fluctuation of the system was buffered and the humidity control was better than 0.1% mol. In the final measurement set-up, the nitrogen going into the evaporator mixer was flowing at 500 ml/min and the gas mixing system provided 500 ml/min. Because of the large buffering volume of the flask, it takes about 30 to 40 min until the output form this flask has stabilized. The flask in the environmental chamber was maintained at a constant temperature above the highest dew point we measured.

With the buffered system the average accuracy of humidity adjustment is similar to that of the unbuffered system, but the errors are much smaller [Eja01]. In this case, the temperatures of the evaporator were similar to those used in the unbuffered case. Because of the buffering, the sensitivity to changes of the evaporator temperature is almost eliminated.
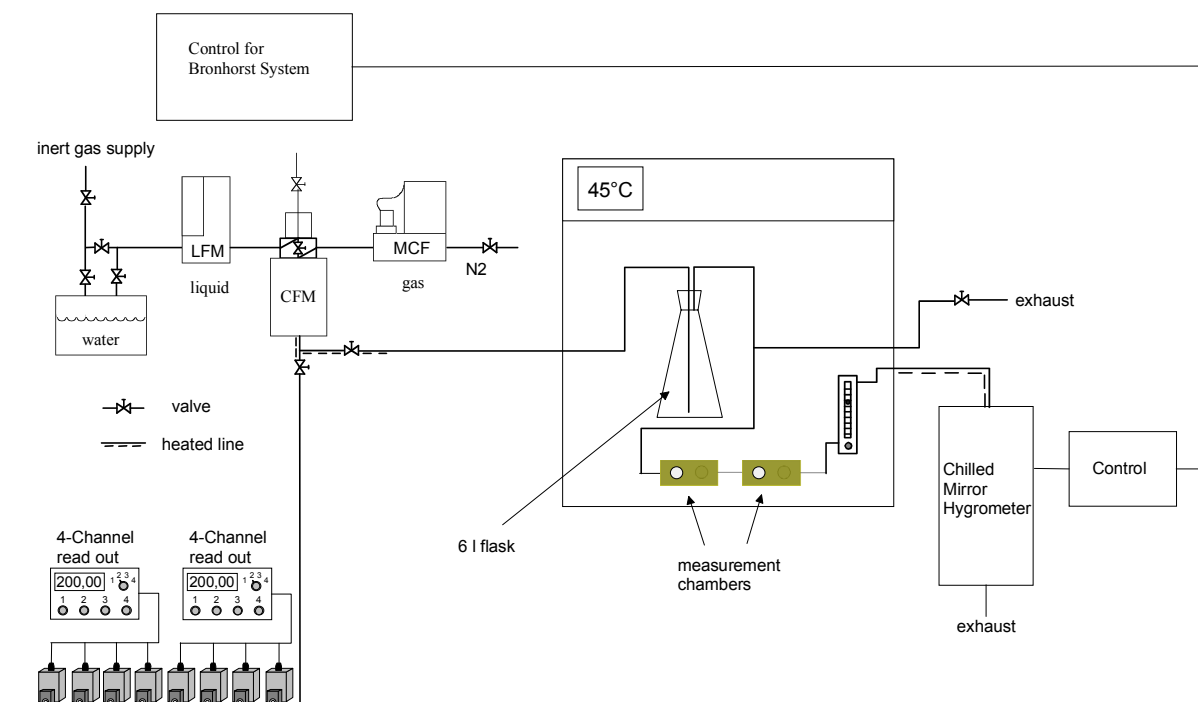
Figure 27: Schematic drawing of the measurement set-up for humidity measurements. Two gas flows are provided: 500 ml/min N_2 were wetted by a Bronkhorst evaporator system, which was controlled by chilled mirror hygrometer at the end of the line, which measured the dew point of the gas. A gas mixing system provided the second gas flow with the analytes to investigate. The two flows were mixed at the outlet of the Bronkhorst evaporation system and got in the oven by a heated line. In the oven, the gas was purged through a 6 l flask to prevent humidity spikes. After this flask, the flow was spitted in front of the measurement chamber. The flow through the measurement chamber was controlled by a rotameter.

3.2.5.3 Set-up for CMOS machined micro sensors

Figure 28 summarizes the above-mentioned components for measuring the CMOS sensors. Because of the high number of instruments for measuring the CMOS sensors with circuitry (Vdd power supply, reference current and voltage) only two sensors with circuitry were measured at once. The rest of the available places in the two measurement chambers were equipped with test structures.
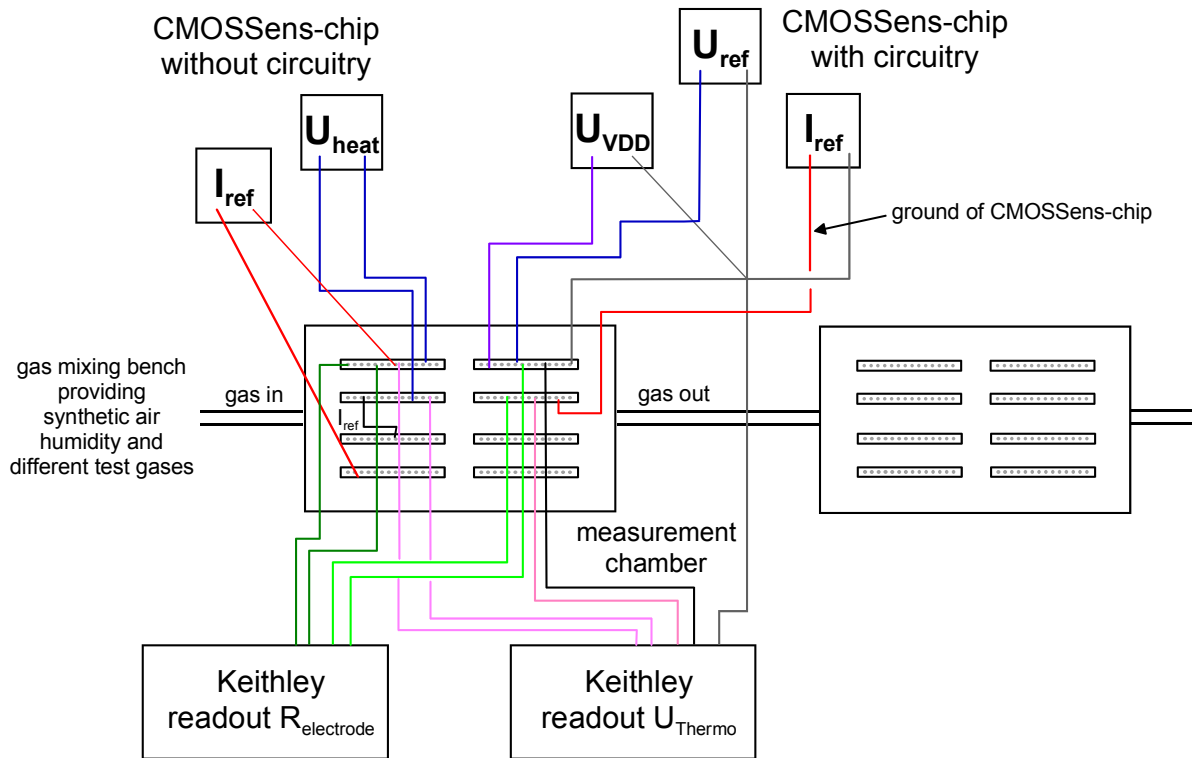
Figure 28: Measurement set-up for measuring CMOS-chips with and without circuitry. The gas, provided by a gas mixing, system flows through two aluminium measurement chamber that holds up to four sensors. The sensor membranes were heated by a voltage source and a reference current was applied. The sensors with circuitry were additionally connected to supply voltage of 5.5 V. The sensor resistance and sensor temperature was read out with two Keithleys DMM199.

3.3   Measurements performed

3.3.1   Alumina substrates

3.3.1.1   Measurements in low oxygen concentrations

In this case a sensor array consisting of a 0.2% w.t. Pd and 3 0.2% w.t. Pt doped SnO_2 sensors was used. Two of the three Pt doped are of a different production run, which have a gab electrode and a smaller size of the area covered with the sensitive layer (type 2).

The investigated gases were CO (50, 100 and 250 ppm) and C_3H_8 (25, 50 and 100 ppm). The oxygen concentrations were ranging from 0, 10, 25, 50 ppm 1 and 5% where N_2 (purity at least 5.5) was used as carrier gas. The applied humidities were 0 and 1020 ppm_v. Different sensor temperatures – 250°C, 300°C and 350°C – were applied to investigate the temperature dependence of the sensors in these conditions.

With the measurement set-up for high humidities concentrations of 0^1, 2.4%, 3.4%, 5% and 10% absolute humidity were measured. The sensors measured in this run were the same 0.2% Pd and Pt doped sensors of type 1 as for the measurements used in low humidity and some undoped sensors based on different grain size materials (T_{cal} = 450°C and T_{cal} = 1000°C). The high humidity measurements were carried out at a sensor temperature of 280°C (U_h = 5.5 V) for the doped sensors and 380°C (U_h = 6.9 V) for the undoped sensors. These temperatures were chosen in order to achieve a highs sensitivity to CO [Kap01].

The analyte exposure times varied from 30 up to 120 min depending on the analyte gas and the measurement conditions. At high oxygen concentrations or humidity equilibrium was reached faster.

3.3.1.2 Discrimination of CO and CH$_4$

The sensors were exposed to CO (0 - 14 ppm), CH$_4$ (0 - 5000 ppm) and mixtures of both in synthetic air at different relative humiditys (0%, 30 and 50% at 25°C).

Each measurement was repeated at least 8 times in order to get an idea about the reproducibility of the sensor signals. This measurement cycle was carried out at two temperatures 350°C and 400°C to obtain more variables for a multivariate data analysis.

In each measurement a five hours preconditioning period (sensors exposed to the carrier gas - synthetic air - at the humidity to be used in the experiment) was allowed. Afterwards, 60 min analyte exposure was alternated with 80 min carrier gas exposures.

3.3.2 Micromachined CMOS sensors

As mentioned in chapter 3.1.2.2, different kind of sensors were used for the first gas measurements. The different characteristics are:

- CMOSSens chips without circuitry, just membrane with electrodes (later reffered as test structures).
- CMOSSens chips with circuitry.
- Electrode structure (gap: 10, 50 or 100 μm).
- Chip metallization (Ni/Au, Au, Rh and Pt).
- Annealing conditions (temperature, background gas: air and nitrogen).
- Design of the membrane (dielectric meander, metal meander, circular ring)
- Different production runs

---

[1] The background H$_2$O concentration was in this case quite high, because the system was not optimised as well as the purging time with dry N$_2$ was too short – 3 day with heating up of the sensors.

The characteristics of the measured sensors are listed in detail in Table 7. The packaging and sensing layer – 0.2% w.t. Pd doped SnO_2 thick film - were the same for all sensors. The packaging was Epotek H72 annealed for one hour at 110°C.

Table 7: List of some sensors and their characterisation based on design, annealing conditions and production run.

Sensor	Annealing	conditions	Design	Run	Generation
	atmosphere	temperature	electrode distance		
Pt1	N_2	400°C	Polyplate 50	1153	1st
Pt5	N_2	400°C	CMOSSens2	1433	1st
Au2	air	400°C	Dielectric ring 50 IsMean 50	1153	1st
Au3	N_2	400°C	IsCir Ring	1433	1st
Rh3	air	400°C	CMOSSens2	CYE 1433	1st
Au II 8	air	400°C	IsMean/ dielectric ring	1153	2nd
NiAu 3+4	air	400°C	CMOSSens CS 1.1c	1433	2nd
NiAu 5+6	air	400°C	IsMean	1433	2nd
Pt II 5+6	air	400°C	CMOSSens CS 1.1c	1433	2nd
Pt II #19	air	400°C	Dielectric Mean 10	1153	2nd
Pt III CS1.2A	air	400°C	DielectricRing 50	1433	3rd
Pt III CS1.2B	air	400°C	DielectricRing 50	1433	3rd
Pt III L/A	air	400°C	DielectricRing 50	1433	3rd
Pt III L/B	air	400°C	DielectricRing 50	1433	3rd
Pt III R/A	air	400°C	DielectricRing 50	1433	3rd
Pt III R/B	air r	400°C	DielectricRing 50	1433	3rd

To characterise the sensor performance of the newly developed CMOS fabricated sensor different gases, temperatures and relative humidity were applied. The test gases are as follows:

- Carbon monoxide (CO), 10 – 100 ppm
- Methane (CH_4), 750 – 10 000ppm
- Octane (C_6H_{14}), 10 – 100 ppm
- Methylcylohexane (C_7H_{14}), 10 – 100ppm
- Toluene (C_7H_9), 10 – 100 ppm

- 1-Propanol (C_3H_7OH), 3 – 50 ppm

- Propanal (C_3H_6O), 10 – 100 ppm

- Ethylacetate ($CH_3COOC_2H_5$), 10 – 100 ppm

The test gases were chosen like this in order to cover a wide range of chemical compounds.

The measurements were carried out at three different relative humidities: 0%, 30% and 50% at room temperature; and three different sensor temperatures: 250°C, 300°C and 350°C.

Before the first measurements, the sensors were exposed to the carrier gas for 2 – 3 hours to reach a steady state. After that equilibration time, they were exposed to the analyte gas for 30 min and than purged with air for another 30 min before the next concentration was applied.

4 Results and Discussion

This chapter is divided in three parts: The first one deals with measurements performed in conditions, which can be found in the automotive field; in the absence and at low O_2 concentrations the sensor responses of differently doped and undoped SnO_2 thick film ceramic sensors operated at different temperatures were measured in different CO and C_3H_8 concentrations. Humidity was also applied ranging from 1020 ppm$_v$ to 10% absolute humidity. It will be shown that the sensing characteristics depend significantly on O_2 and H_2O concentration and an influence of the operating temperature and the dopant was also found. On the basis of experimental results, different sensing mechanisms are suggested.

In the second part measurements are presented of CO, CH_4 and their mixtures at different humidities and temperatures. Here the discrimination power of a sensor array of 5 differently doped SnO_2 thick film sensors were tested. The application condition in view is natural gas leakage detection.

The third part deals with the sensor performance of newly developed CMOS micromachined hot plates that were coated with Pd doped thick film SnO_2 layers. Three design generations were tested and characterised. An extensive investigation was carried out at different temperatures, humidity levels and test gases that cover a broad range of application. The CMOS microsensor system will offer the advantages of on chip electronics, low power consumption, and low costs.

4.1 Sensor performance at low oxygen concentrations

As already shown in the experimental part (Figure 24), one obtains high sensor signals for doped SnO_2 thick film sensors exposed to CO and C_3H_8 even if nearly no O_2 and H_2O are present. In Figure 29, typical signals to CO and C_3H_8 in the absence of O_2 and H_2O are displayed for all investigated sensors (for details see chapter 3.3.1.1). For sake of clarity, in the left side of Figure 29 only one of the sensors used for the measurements in the absence of H_2O and low O_2 concentration is shown. The set of sensors also measured at high absolute humidities are shown in the right side. In the latter set-up, also undoped sensors were investigated. The measurements at high humidity were carried out first and at that time, no appropriate hygrometer and oxygen analyser were available. In that condition, it would anyhow not bring additional information because small changes in O_2 and H_2O concentration would hardly be detectable in the background of high humidities.
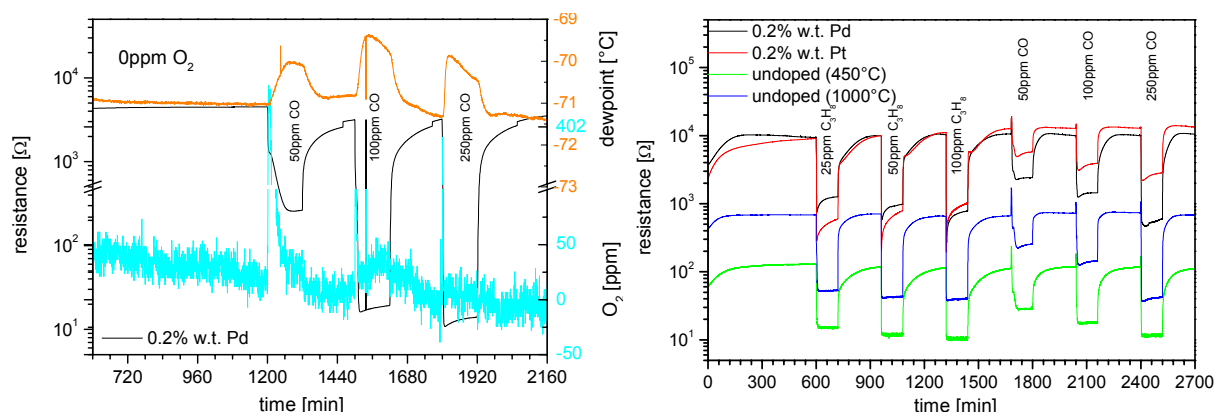
Figure 29: Sensor response of the investigated Pd and Pt doped and undoped SnO₂ thick film sensors in the absence of O₂ and H₂O. The different doped sensor (0.2% w.t Pd and 0.2% w.t. Pt) were operated around 300°C and the 2 undoped (calcinated at 450 and 1000°C) at 350°C. The left side shows the sensor resistance of one sensor (0.2% w.t. Pd) with online monitoring of H₂O and O₂ concentration. The undoped sensors in the right side were measured before appropriate hygrometer and oxygen analyser were available.

It is clearly seen in Figure 29 that for all sensor types one obtains a remarkably high sensor response for CO and C_3H_8 in the absence of O_2 and H_2O.

In the following, the measurement results are presented for the sensor resistance and the sensor signal (R_0 / R). With the help of this information, it is possible to derive a sensing mechanism valid for different presented sensors in changing O_2 and H_2O concentration; the mechanisms are presented in the discussion part.

4.1.1 O_2 dependence in the absence of H_2O

Four SnO_2 thick film sensors – 1 doped with 0.2% w.t. Pd and 3 doped with 0.2% w.t. Pt but of two different electrode designs (1x type 1 and 2x type 2 for details see chapter 3.3.1.1) - were exposed to CO and C_3H_8 at different concentrations of O_2 and in the absence of H_2O at three different temperatures (250°C, 300°C and 350°C). A special measurement set-up described in chapter 3.2.5.1 provided online monitoring of O_2, H_2O and CO_2 concentrations. Detailed results are presented for 300°C. At the end of each section the temperature dependence of two selected sensors is shown for a constant test gas concentration. The mean values and the standard deviations of at least three measurements are displayed in all the graphs.

4.1.1.1 Propane (C_3H_8)

The results obtained for C_3H_8, resistance and sensor signals (R_0 / R) are shown in Figure 30 for a 0.2% w.t. Pd doped SnO_2 thick film sensor and in Figure 31 for a 0.2% w.t. Pt doped sensor.

As expected, the base line sensor resistance of the Pd doped sensor increases with increasing O_2 concentration because of the adsorption of O_2 related species, which act as electron acceptors and by that increasing the resistance (for details see chapter 2.2.1 and the references therein).

In the absence of oxygen upon exposure to C_3H_8, the sensor resistance decreases more than one order of magnitude. The decrease is non-linear and leads to saturation at higher C_3H_8 concentrations. By increasing the O_2 concentration up to 50 ppm O_2, one just observes a small shift of the sensor resistance towards higher values. At higher O_2 concentrations - 1% and 5% - the resistance increases significantly in the range of one order of magnitude. For all O_2 concentrations, the trend of the curve is the same.
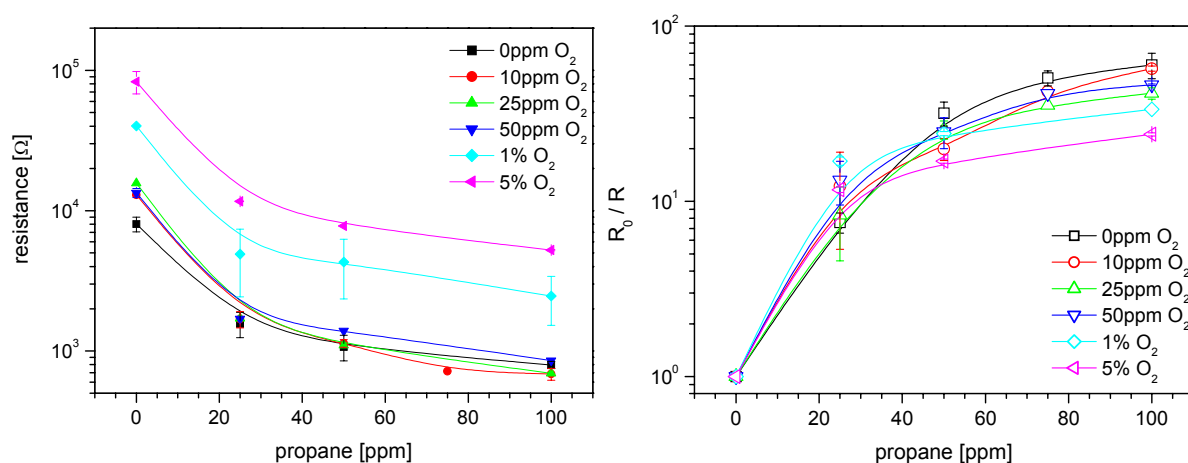

Figure 30: Sensor resistance (left) and sensor signal (right) of a 0.2% w.t. Pd doped SnO₂ thick film sensor measured for C₃H₈ (0 – 100 ppm) in the presence of different O₂ concentrations (0, 10, 25, 50 ppm, 1 and 5%) and in the absence of water. The sensor temperature was 300°C.

This behaviour is even more recognisable in the graph showing the sensor signal vs. C_3H_8 concentration (Figure 30 right side). Here, one observes that the sensor signal is almost the same for all O_2 concentrations. This indicates that adsorbed oxygen does not influence significantly the interaction of C_3H_8 with the SnO_2 surface. O_2 only moves the baseline of the sensor.

In the case of a 0.2% w.t. Pt doped SnO_2 thick film sensor the C_3H_8 sensing characteristic is quite different (in left side of Figure 31). At 0 ppm O_2 upon exposure to 25 ppm of C_3H_8 the resistance of the Pt doped sensor decreases more than two of orders magnitude. An additional increase of the C_3H_8 concentration does not result in a further resistance decrease; the Pt doped sensor is saturated. By increasing the O_2 concentration to 10 ppm O_2, the saturation of the sensor resistance takes place at a higher C_3H_8 (50 ppm) concentration. At a further increase of the O_2 concentration to 25 ppm no saturation is observed and at 50 ppm O_2 one obtains a nearly linear decrease of the logarithm of the resistance. The increase of the O_2

concentration to 1 and 5% again changes the shape of the resistance depending on C_3H_8 concentration and dramatically decreases the sensor signal. The curves obtained for 1 and 5% are very similar with the one measured for 5% shifted as expected upwards.

Looking at the sensor signals in the right side of Figure 31 one clearly observes the trends described for the sensor resistance: high sensitivity and rapid saturation at 0% O_2, an increased "linearity" at low O_2 concentrations and a "normal" behaviour at high O_2 concentrations. The sensor signal decreases more than an order of magnitude at high O_2 concentrations. Online monitoring of O_2 and water vapour shows no significant changes due to the sensing. It appears that the O_2 influences the reaction and it is expected that adsorbed oxygen take an active role in the sensing.
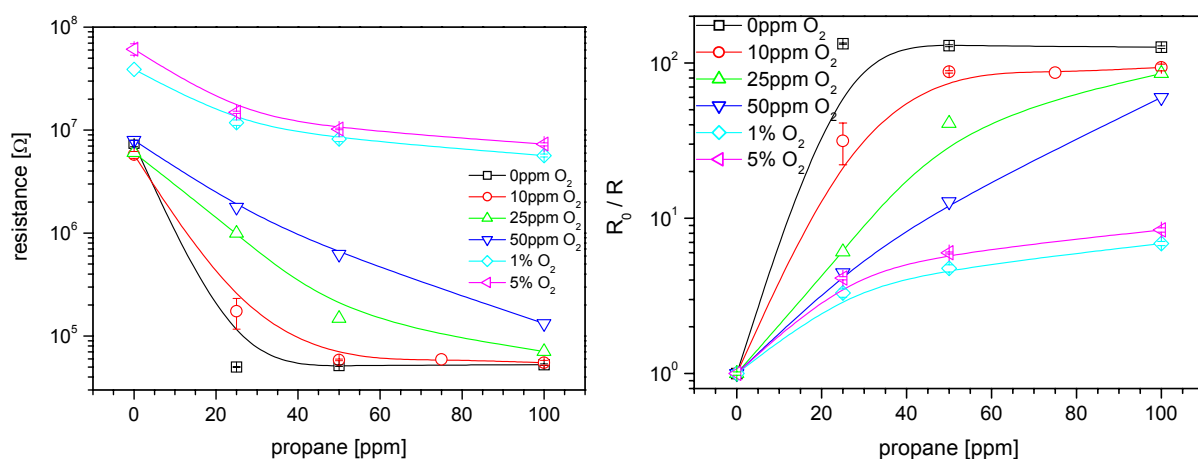

Figure 31: Sensor resistance (left) and sensor signal (right) of a 0.2% w.t. Pt doped SnO$_2$ thick film sensor measured for C$_3$H$_8$ (0 – 100 ppm) in the presence of different O$_2$ concentrations (0, 10, 25, 50 ppm, 1 and 5%) and in the absence of water. The sensor temperature was 300°C.

Comparing the different dopants – Pd and Pt – one realize that their presence induces a difference in the sensing characteristics related to the influence of O_2. Also, the maximum sensor signals at 300°C operating temperature in the absence of O_2 are comparable.

At high temperature – 350°C – it was observed that a significant concentration of H_2O – 12 ppm[1] - is generated in the presence of high O_2 concentration. That indicates that in the sensing mechanism H_2O is generated.

---

[1] From this value the max. background concentration of C_3H_8 has already been subtracted.
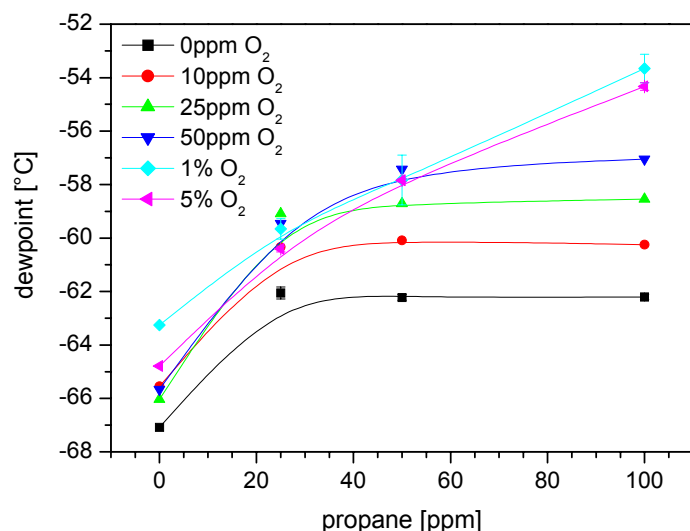
Figure 32: Generation of H₂O in the presence of different C₃H₈ concentrations for sensors operated at 350°C. For high O₂ concentrations (1 and 5%), the H₂O concentration increases about 12 ppm[1].

The temperature dependence of the sensor signal of Pd and Pt doped sensors are shown in Figure 33 for 25 ppm C_3H_8. The lowest C_3H_8 concentration was chosen because the biggest differences were found at this concentration.

One observes for the Pd doped sensor (Figure 33, left side) that in the presence of O_2 the differences are small at a certain temperature. In the absence of O_2, the sensor signal is nearly the same at 250°C and 300°C but increases dramatically[2] at temperatures above 300°C. At low O_2 concentrations (10 ppm), a small increase in the sensor signal is visible. At 25 ppm and 50 ppm O_2, the sensor signal slightly decreases. At high O_2 concentration (1% and 5%) the sensor signal increases with increasing sensor temperature and O_2 concentration.

---

[1] From this value the max. background concentration of C_3H_8 has already been subtracted.

[2] The resistance for the Pd doped sensor at 350°C was to low to be measured by the Keithley DMM199 (at least below 10 Ω), which was operated at fixed range. In this case all the sensor signals were set to 10 000.
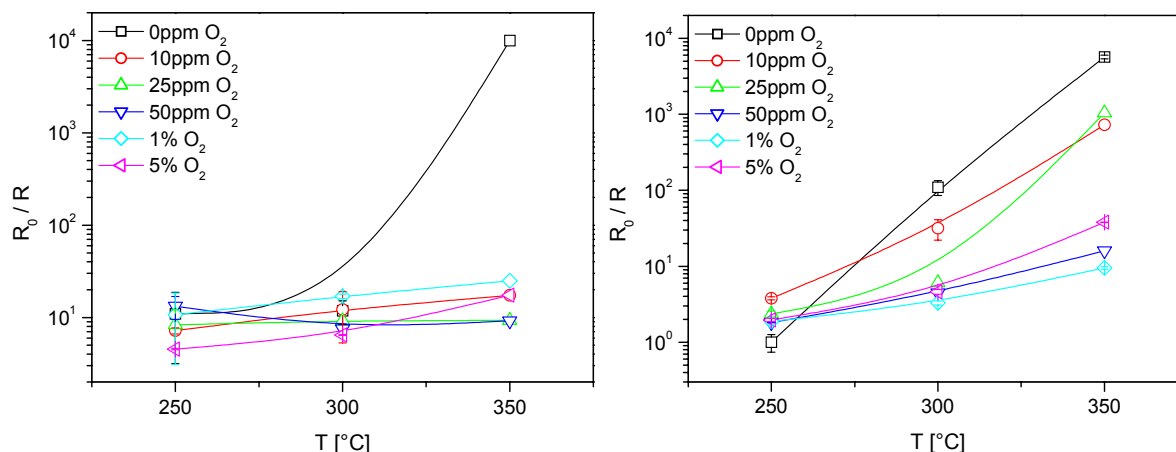
Figure 33: Temperature dependence of the sensor signal measured with 0.2% w.t. Pd (left) and 0.2% w.t. Pt (right) doped SnO_2 thick film sensors for 25 ppm C_3H_8. The applied O_2 concentration were: 0, 10, 25, 50 ppm, 1% and 5%. No H_2O was present.

The temperature dependence of the 0.2% w.t. Pt doped SnO_2 sensor is shown in the right part of Figure 33. One observes that the sensor signal increases significantly for increasing temperature in all different O_2 concentrations. The steepest slope (high sensitivity) is observed at 0% O_2 and it decreases with increasing (high) O_2 concentration. Above 50 ppm O_2 signals are almost similar. Having a close look one can suggest that the sensitivity decreases with increasing O_2 concentration, with a minimum at 1% O_2.

Summarizing the temperature dependence of the sensor signal for the differently doped SnO_2 sensors one can conclude that the performance in terms of resolution will be provided by a Pt doped sensor operated at different temperatures.

4.1.1.1.1 CO

The sensor resistance and sensor signal obtained upon CO exposure are presented in Figure 34 for the Pd doped SnO_2 thick film sensor and in Figure 35 for the Pt doped one. In Figure 34 one observes for CO a quite different O_2 dependence of the response of the Pd doped sensor in comparison to the case of C_3H_8; the behaviour is similar to the one obtained for the Pt doped sensor. At 0 and 10 ppm O_2 one records a very high sensitivity and fast saturation at low CO concentrations; the resistance values are nearly identical for 100 and 250 ppm CO. The increase of the O_2 concentration leads to a "linearity" of the sensor resistance dependency. A normal behaviour is again observed at high O_2 concentrations. All that is more clearly seen in the plot of the sensor signal for the Pd doped sensor (right part of Figure 34). One obtains a remarkably high sensitivity to CO in the absence of O_2 or at very low concentrations of O_2. By increasing the O_2 concentration, nearly the same sensor signal are obtained for 50 and 250 ppm CO but the ones at 100 ppm are an order of magnitude lower. At

high O_2 concentrations the sensor signal at 100 and 250 ppm are one half order of magnitude lower and tend to saturate.

For a good resolution between different CO concentrations, operation at 25 and 50 ppm of O_2 would provide the best performance.
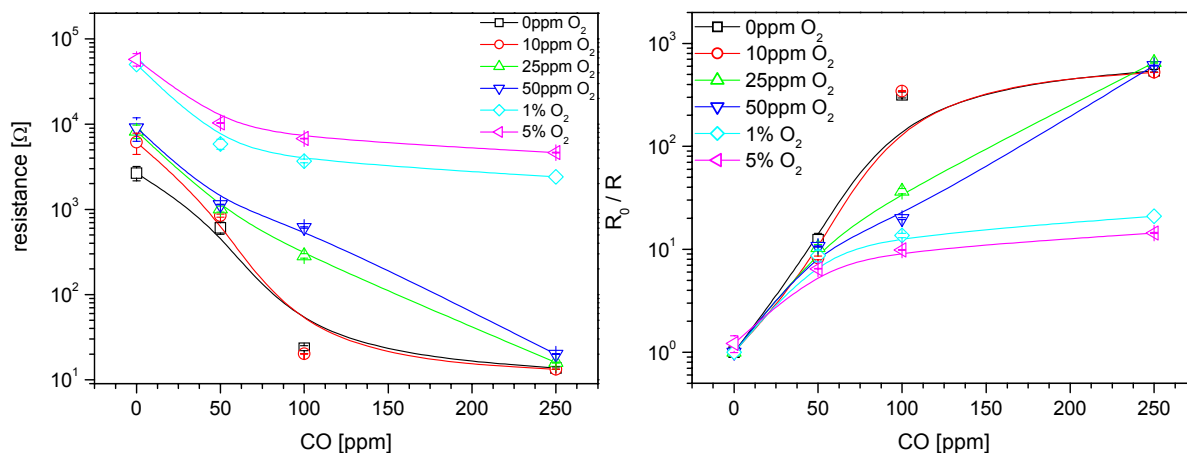

Figure 34: Sensor resistance (left) and sensor signal (right) of a 0.2% w.t. Pd doped SnO_2 thick film sensor is measured for CO (0 – 250 ppm) in the presence of different O_2 concentrations (0, 10, 25, 50 ppm, 1 and 5%) and in the absence of water. The sensor temperature was 300°C.

The results obtained for the CO exposure o f the Pt doped thick film sensor show, again, a different behaviour compared to the Pd doped one but with the same trends as in the case of C_3H_8 exposure. There are differences in the small CO – 50 ppm – concentration, where the values measured for the Pt are spread over a large resistance range of more than two orders of magnitude. Saturation occurs already at 50 ppm CO in the absence of O_2. By increasing the O_2 concentration, saturation is reached at higher CO concentrations. The "normal" sensor behaviour is again observed for high O_2 concentrations.

Looking at the sensor signals in Figure 35 one observes again remarkable high sensor signals about four orders of magnitude at low O_2 concentrations. At high O_2 concentrations the sensor signals are almost identical.
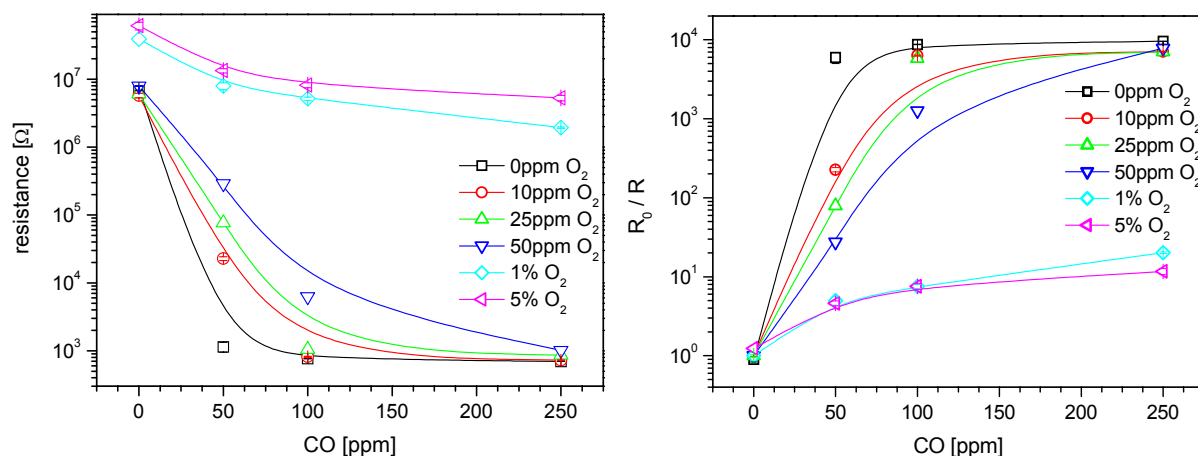
Figure 35: Sensor resistance (left) and sensor signal (right) of a 0.2% w.t. Pt doped SnO$_2$ thick film sensor is measured for CO (0 – 250 ppm) in the presence of different O$_2$ concentrations (0, 10, 25, 50 ppm, 1 and 5%) and in the absence of water. The sensor temperature was 300°C.

Summarising, for both Pd and Pt doped sensors O$_2$ plays a role in the sensing mechanism of CO. In the absence of water the sensitivities are reduced in the presence of O$_2$.

The temperature dependence of the sensor signals of the Pd and Pt doped sensors is shown in Figure 36 for the case upon exposure to 50 ppm CO. Again, the lowest CO concentration was chosen because the main differences of the sensor performances are obvious at low concentrations. Additionally, in most applications 50 ppm CO is the relevant concentrations.

For the Pd doped sensor one observes that in the absence of O$_2$ there is nearly no temperature dependence of the sensor signal. At low O$_2$ concentrations, the sensor signal decreases half an order of magnitude when the temperature increases. In the presence of high O$_2$ concentrations and opposite behaviour is observed: The sensor signal increases half an order of magnitude when the temperature increases.

For the Pt doped sensor – right side in Figure 36 – one observes that the sensor signal increases slightly with the temperature in the absence of O$_2$. Again, the sensor signal decreases when the temperature increases for low O$_2$ concentrations. Because of the, in general, higher sensor signals obtained for Pt doped SnO$_2$ also the decrease is higher than for Pd doped SnO$_2$. There is also a decrease in sensitivity in the low O$_2$ concentration range, when the O$_2$ concentration increases. At high O$_2$ concentrations, the opposite is again observed by increasing the sensor temperature increases the sensor signal.
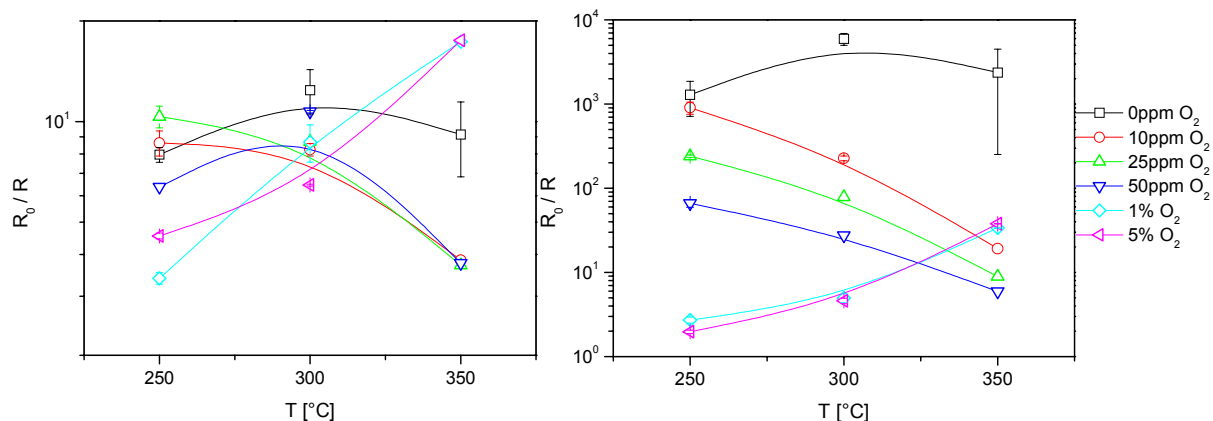
Figure 36: Temperature dependence of the sensor signal measured with 0.2% w.t. Pd (left) and 0.2% w.t. Pt (righ) SnO$_2$ thick film sensors for 50 ppm CO. The applied O$_2$ concentration were: 0, 10, 25, 50 ppm, 1% and 5%. No H$_2$O was present.

4.1.2 Low humidity (1020 ppm$_v$)

This section describes the influence of a background of 1020 ppm$_v$ H$_2$O (4.4% r.h at 20°C and 0.76 g / m^3) on the response to CO and C$_3$H$_8$ of Pd and Pt doped sensors recorded at different O$_2$ concentrations.

In the presence of H$_2$O the sensor resistance decreases. Therefore, the interaction will take place at higher free electron concentration (for details see 2.2.2 and the references therein).

4.1.2.1 Propane (C$_3$H$_8$)

Figure 37 and Figure 38 show the influence of O$_2$ concentration on sensor resistance and sensor signal dependence on C$_3$H$_8$. The Pd and Pt doped SnO$_2$ thick film sensors were operated at 300°C in a background of 1020 ppm$_v$ H$_2$O. One notices that the shapes of the sensor resistance and sensor signal of the Pd doped sensor (Figure 37 right side) are qualitatively the same like in the absence of H$_2$O; the sensor resistance is only shifted to lower values. The low sensor signal values at 50 ppm O$_2$ are due to the low baseline resistance, which is probably an error in the measurement of the baseline resistance.

One can conclude that O$_2$ does not play an important role besides changing the baseline. The presence of 1020 ppm$_v$ H$_2$O decreases the sensitivity in the range of an order of magnitude.
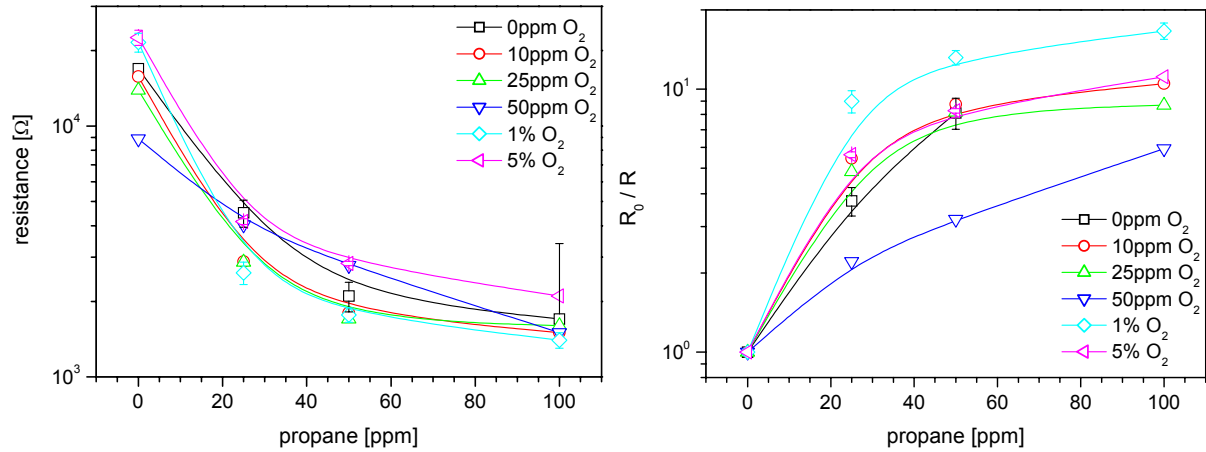
Figure 37: Sensor resistance (left) and sensor resistance (right) of a 0.2% w.t. Pd doped SnO$_2$ thick film sensors are plotted vs. C$_3$H$_8$ concentration for different O$_2$ concentrations (0, 10, 25, 50 ppm, 1 and 5%) in the presence of 1020 ppm$_v$ H$_2$O. The sensors were operated at 300°C.

Again, the results obtained for the Pt doped sensor are quite different (Figure 38). In the absence of O$_2$ there is just a shift of the baseline resistance to a lower value in the range of one order of magnitude. Saturation of the sensor occurs again at 25 ppm C$_3$H$_8$. Comparing the results with the one obtained in the absence of O$_2$ and H$_2$O one observes that there is no influence of H$_2$O on the trend and sensor signal values. At low O$_2$ concentrations the "linearity" is basically lost but the sensitivity remains practically the same. At high O$_2$ concentrations, there is only a small decrease of the sensor resistance and the sensitivity of the Pt doped sensor towards C$_3$H$_8$ is nearly completely killed.

Summarising, one can state that there is a collective effect of O$_2$ and H$_2$O in the sensing mechanism of C$_3$H$_8$ for Pt doped sensors. Comparing the data obtained at 1020 ppm$_v$ H$_2$O with the one measured in the absence of H$_2$O it results that the sensing characteristics for a Pd doped sensor is not changed; the sensor signal is only decreased in the presence of H$_2$O in the range of one order of magnitude.
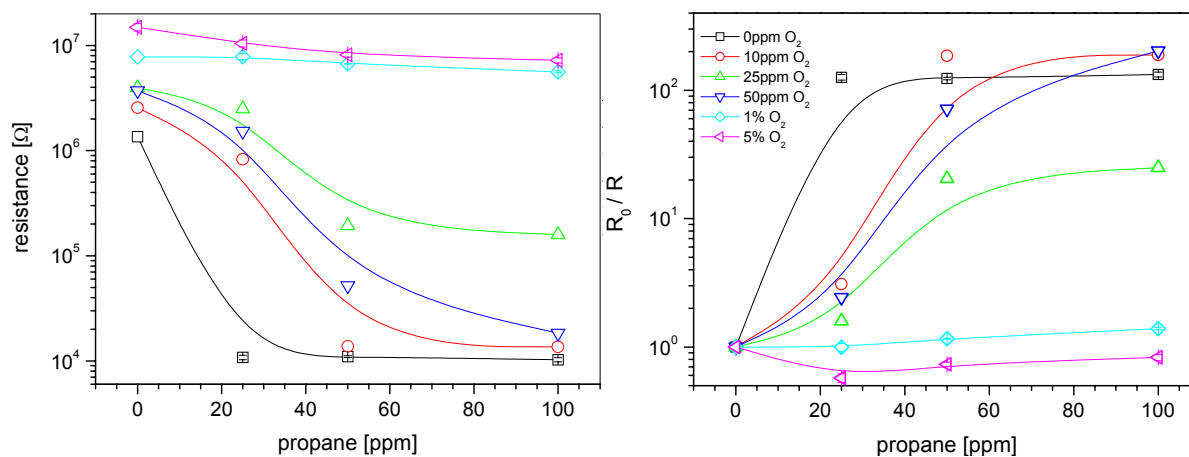
Figure 38: Sensor resistance (left) and sensor resistance (right) of a 0.2% w.t. Pt (2nd design) doped SnO_2 thick film sensors are plotted vs. C_3H_8 concentration for different O_2 concentrations (0, 10, 25, 50 ppm, 1 and 5%) in the presence of 1020 ppm_v H_2O. The sensors were operated at 300°C.

The temperature dependencies of the sensor signal of the Pd and Pt sensors upon exposure of 25 ppm C_3H_8 are shown in Figure 39. On the left side of Figure 39, the temperature dependence of the Pd doped sensor is plotted. It can be seen that the sensor signal obtained at 25 ppm C_3H_8 generally increases with increasing sensor temperature. The slope, which characterises the sensitivity, is nearly the same at the different O_2 concentrations. One can also see that there is nearly no sensitivity for C_3H_8 at 250°C in the absence of O_2. The latter indicates that the reaction needs a higher activation energy when no oxygen is present.

In the case of the Pt doped sensor, shown on the right side of Figure 39, one observes that at really low O_2 concentrations (0 and 10 ppm) the sensor signal increases with increasing temperature. When the temperature is increased up to 350°C the sensor signal increases two orders of magnitude. At higher O_2 concentrations (25 ppm – 5%) there is nearly no change in the sensor signal by increasing the temperature from 250°C to 300°C and up to 350°C only a small increase is visible. Comparing these results with the ones obtained in the absence of H_2O one observes that the differences only occur at low 0% O_2 and at 350°C sensor temperature where a higher sensor signal was measured in the absence of O_2.
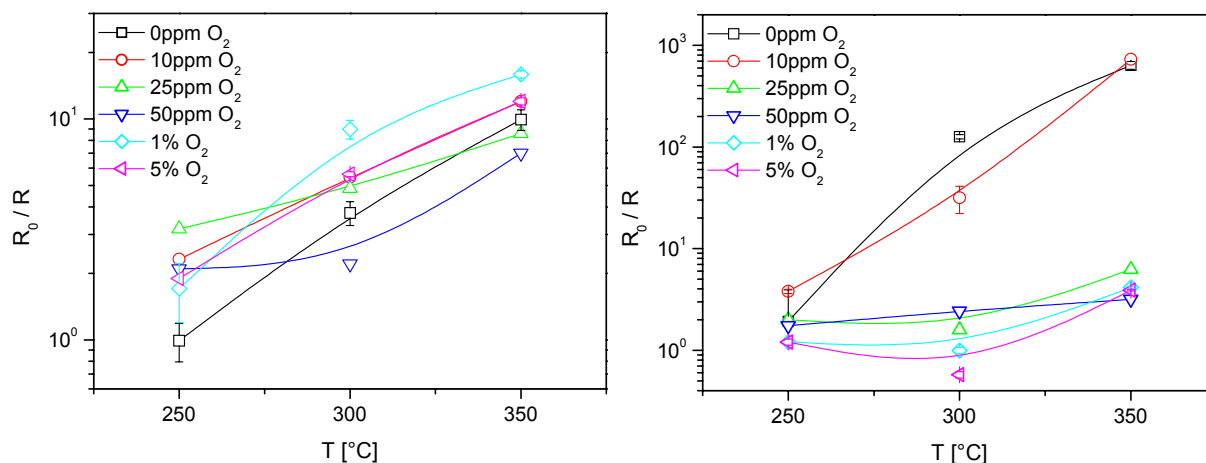
Figure 39: Temperature dependence of the sensor signal measured for 25 ppm C_3H_8 with 0.2% w.t. Pd (side) and 0.2% w.t. Pt (right side) SnO_2 thick film sensors. The H_2O concentration was 1020 ppm_v and applied O_2 concentration were: 0, 10, 25, 50 ppm, 1% and 5%.

One can conclude that in the presence of low H_2O concentrations the sensor signal of the Pd doped sensor increases with increasing temperature but shows no dependency on the O_2 concentrations. The Pt doped sensors show generally higher sensor signals and a different dependency on the O_2 concentration in the presence of H_2O than in the absence of H_2O.

4.1.2.1.1 CO

Measuring CO in the presence of 1020 ppm_v H_2O (see Figure 40) one observes a very strong decrease of the sensor resistance. Some values were so low that the Keithley DMM199, which was operated at a fixed measurement range, could not measure them. For low O_2 concentrations – 10 ppm – one obtains nearly the same sensor response, so H_2O brings together the zero and low O_2 concentration effects but that can be also due to artefacts because in this condition the multimeter is operated at the limit of its resolution. By a further increase to 25 ppm O_2 it is possible to measure 50 ppm CO but at 100 ppm the measurable limit is again reached. At high O_2 concentrations[1] the qualitative behaviour is not changed in the presence of H_2O, only the baseline is moved to lower values.

Looking at the sensor signal one observes that its value in the presence of H_2O is significantly increased for 0, 10 and 25 ppm O_2. For high O_2 concentration, only a small increase is recorded.

In the CO interaction with Pd doped sensors, it is still the O_2, which plays the main role; H_2O merely adjusts the offset.

---

[1] 250 ppm CO in 50°ppm O_2 could not be measured because of the flow limitations of the gas mixing system.

Figure 40: Sensor resistance (left) and sensor resistance (right) of a 0.2% w.t. Pd doped SnO₂ thick film sensor vs. CO concentration for different O₂ concentrations (0, 10, 25, 50 ppm, 1 and 5%) in the presence of 1020 ppmᵥ H₂O. The sensor temperature was 300°C.

In the case of the Pt doped sensors (Figure 41), H_2O pushes the values obtained for low O_2 concentrations towards the one obtained for 0 ppm O_2 and does not have a big influence on the values obtained for high O_2 concentrations. The trends for all curves are the same for all O_2 concentrations.

The sensor signal is increased by one order of magnitude at low O_2 concentration and no notable increase is observed at high O_2 concentration.
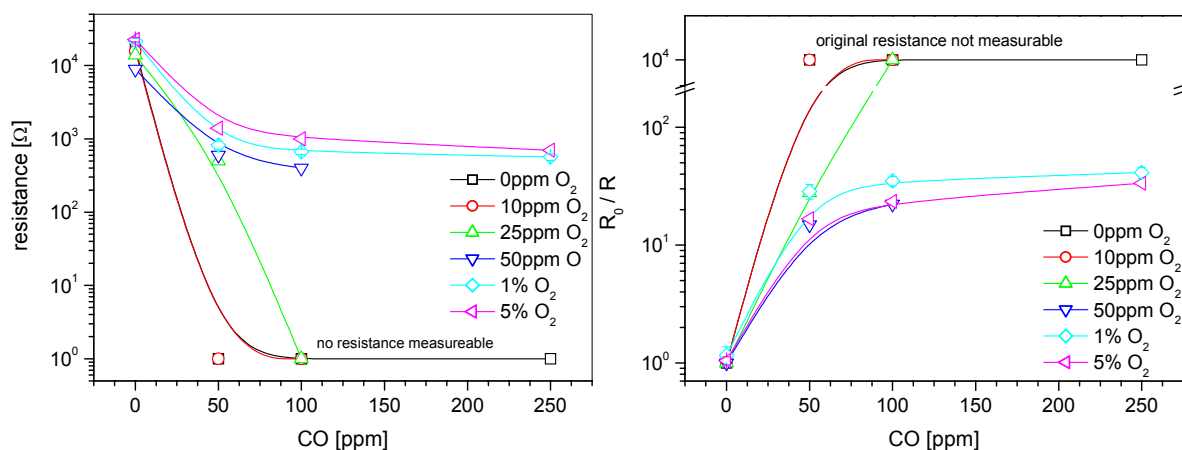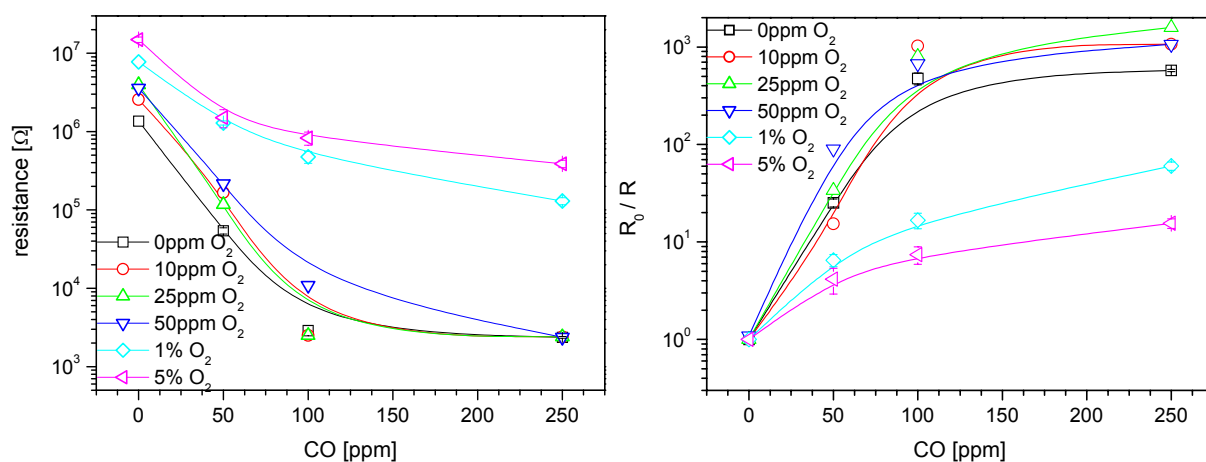

Figure 41: Sensor resistance (left) and sensor resistance (right) of a 0.2% w.t. Pt doped SnO₂ thick film sensor vs. CO concentration for different O₂ concentrations (0, 10, 25, 50 ppm, 1 and 5%) in the presence of 1020 ppmᵥ H₂O. The sensor temperature was 300°C.

The temperature dependence of the Pd and Pt doped sensors upon exposure to 50 ppm CO at different O_2 concentrations are shown in Figure 42. At low O_2 concentrations, the sensor signal of the Pd doped sensor generally decreases with increasing temperature (Figure 42 left side). At 0 and 10 ppm O_2, a pronounced maximum of the sensor signal was observed at 300°C. At 50 ppm there is only a slight decrease due to the relatively high value obtained at

250°C. At high O_2 concentration, a not so spectacular maximum in the sensor signal is also observed at 300°C. A further increase to 350°C leads to a small decrease in the sensor signal, where nearly the same values were obtained for 1 and 5% O_2. From this one can conclude that the O_2 concentration and the sensor temperature influence the CO sensing with Pd doped sensor in the presence of low H_2O concentrations. Comparing the temperature of the sensor signal at 1020 ppm_v H_2O to "0 ppm[1]" H_2O one observes that the sensor signals of the Pd doped SnO_2 thick film sensor are quite the same except for the extremely high sensitivity obtained at 0 and 10 ppm O_2 at 300°C.

In the case of the Pt doped sensor (Figure 42 right side) one observes that the sensor signal decreases for all O_2 concentrations by increasing the temperature from 250°C to 300°C. A further temperature increase to 350°C leads to O_2 dependent behaviours. For low O_2 concentrations (0 – 25 ppm) the sensor signal is nearly constant, for 50 ppm there is a further decrease and at high O_2 concentration one observes an increase in the sensor signal.
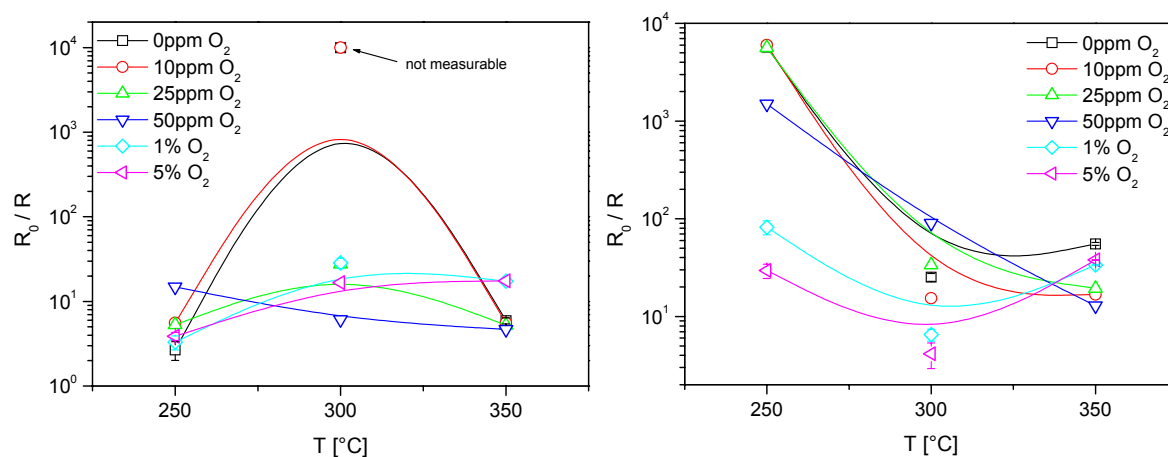
Figure 42: Temperature dependence of the sensor signal measured for 50 ppm CO with 0.2% w.t. Pd (left graph) and 0.2% w.t. Pt (right graph) SnO_2 thick film sensors in the presence of 1020 ppm H_2O. The applied O_2 concentration were: 0, 10, 25, 50 ppm, 1% and 5%.

Comparing the temperature dependence of the sensor signal at 1020 ppm_v H_2O and at "0 ppm_v" H_2O one observes that the H_2O related change of the sensor signals for Pt doped sensors is much higher than the ones observed for Pd doped sensors. The sensor signals are generally higher in the presence of H_2O: one order of magnitude for high O_2 concentrations (1% and 5%) and half an order of magnitude for low O_2 concentration. The temperature dependence of the sensor signal is also different. In the absence of H_2O a steady decrease of the sensor signal was observed at low O_2 concentrations and an increase at high O_2

---

[1] One have to keep in mind, that there is still a H_2O background concentration of the system, but that is for CO below 2 ppm H_2O.

concentrations. H_2O changes it in the way that there is a comparable decrease at 0, 10, and 25 ppm O_2, a linear decrease at 50 ppm O_2 and a slight decrease at high O_2 concentrations. One can conclude that a different influence of O_2 is seen for Pd and Pt doped sensors in the presence of 1020 ppm_v H_2O, and that the sensor temperature also plays a role in the CO, O_2 and H_2O interaction with the SnO_2 surface.

4.1.3 Measurements at high humidity

The following set of measurements was carried out by using a different measurement set-up than the one used in the experiments presented in chapter 4.1.1 and 4.1.2 (for detailed description see chapter 3.2.5.2). Four SnO_2 thick film sensors were measured in the same two measurement chambers, which were used for the measurements discussed above. One of the chambers was equipped with the same sensors – 0.2% w.t. Pd and 0.2% w.t. Pt doped SnO_2 (type 1 provided with interdigitated electrodes, see chapter 3.3.1.1) - and the other with two undoped sensors of the same fabrication type but calcinated at different temperatures. The doped sensors were operated around 300°C and the undoped sensors at 380°C.

In contrast to the previous measurements, only three O_2 concentrations: 0, 1 and 5% were used. It has to be mentioned that the measurements carried out at 0% O_2 and 0% H_2O have not the same quality (background concentration of O_2 and H_2O) as the measurements discussed in chapter 4.1.1 and 4.1.2 and because limited availability of the set-up. Improvements were not possible. Also the CO and C_3H_8 concentrations of reference gas bottles were higher and so accordingly, the errors in the low concentration range were also higher.

Here, results are presented for Pd and Pt (type 1) doped SnO_2 thick film sensors and for the undoped SnO_2 sensor calcinated at 450°C. The latter shows the same effects as the one calcinated at 1000°C. It also offers a better reference for the doped sensors, because of t he similar grain size (same calcination temperature).

4.1.3.1 Propane (C_3H_8) in the absence of oxygen (O_2)

The sensor resistance and sensor signals of three different sensors – Pd, Pt doped and undoped SnO_2 – for different absolute humidities (0 – 10%) are plotted in Figure 43 vs. the C_3H_8 concentration (0 – 100 ppm).

Figure 43: Influence of the ambient humidity on the sensor resistance in nitrogen for 0.2% w.t. Pd (a) and 0.2% w.t. Pt (b) doped (operation temperature 300°C) and undoped (c, operated at 380°C) SnO₂. The sensor resistance (left side) and the sensor signal (right side) are plotted vs. C₃H₈ concentration (0, 25, 50 and 100 ppm) in 0% O₂ and changing absolute humidity (0 - 10%).

One observes that for Pd doped SnO_2 sensor the changes of the sensor resistance are not significantly influenced by exposure to different high H_2O concentrations. A nearly saturated sensor response is nearly observed at 50 ppm C_3H_8 for all H_2O concentrations.

The Pt doped sensor (type 1) shows a significant change in the sensing mechanism in the absence of H_2O of compared to the pressure of high concentrations of H_2O[1]. One can suggest that there is a kind of threshold for low C_3H_8 concentrations, which was also found for CO (will be presented later). For the undoped sensors, the decrease of the resistance with increasing humidity looks like the behaviour observed for the Pd doped sensor but the smallest sensor signal is measured in the absence of H_2O. The changes for the sensor calcinated at 1000°C[2] – which is not shown in Figure 43 - are twice as big as for the one calcinated at 450°C. For the sensor signals the differences in the presence of high humidity concentrations are, for both undoped sensors small.

One can conclude that in the absence of O_2 for Pd doped sensor and for the undoped sensors, H_2O does not change qualitatively the aspects of the sensing process (at medium temperatures). In the case of Pt doping, one observes a change of slope at 25 ppm C_3H_8 induced by the presence of H_2O.

4.1.3.2   CO in the absence of oxygen (O_2)

Figure 44 shows the sensor resistance and sensor signal for the same sensors at different H_2O concentrations (up to 10% absolute) vs. the CO concentration. One observes in all cases that the differences in the sensing are just between very low and high H_2O concentrations (see also chapter 4.1.2.1.1). For all types of sensors, the sensor resistance is quite low for high CO concentrations in the presence of H_2O. Accordingly, the Keithley DMM199 could hardly resolve changes. In the absence of H_2O nearly saturation is reached for all sensors at around 250 ppm CO.

However, differences in the sensing can be observed depending on the dopant and the presence of H_2O. The resistance (logarithmic scale) of the Pd doped sensor decreases nearly linear with increasing CO concentration (Figure 44a). The curve shapes between no H_2O and high H_2O concentration differ for the Pd doped and undoped sensor only in this way that in the absence of H_2O saturation of the undoped SnO_2 occurs at higher CO concentrations.

---

[1] The sensor resistance of the Pt doped sensor of the type 1 shown for the high humidity measurement show the same trend also in 0 and 1020 ppm_v H_2O. At 0 and 1020 ppm it has a lower sensor resistance decrease for C_3H_8 as propane but shows the same trend. It was not presented because the type 2 shows this trend more pronounced.

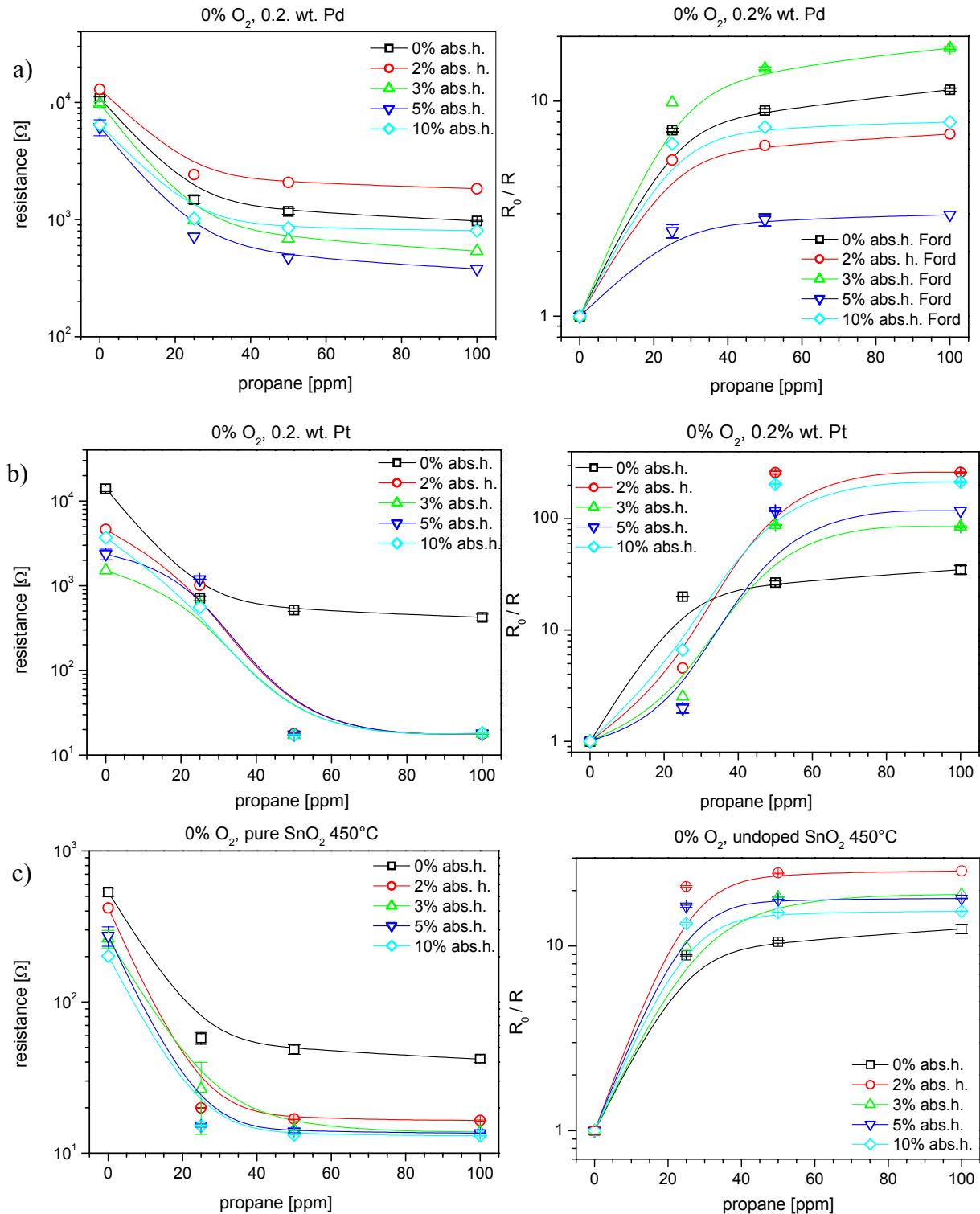[2] Higher calcination temperatures result in a larger grain size.
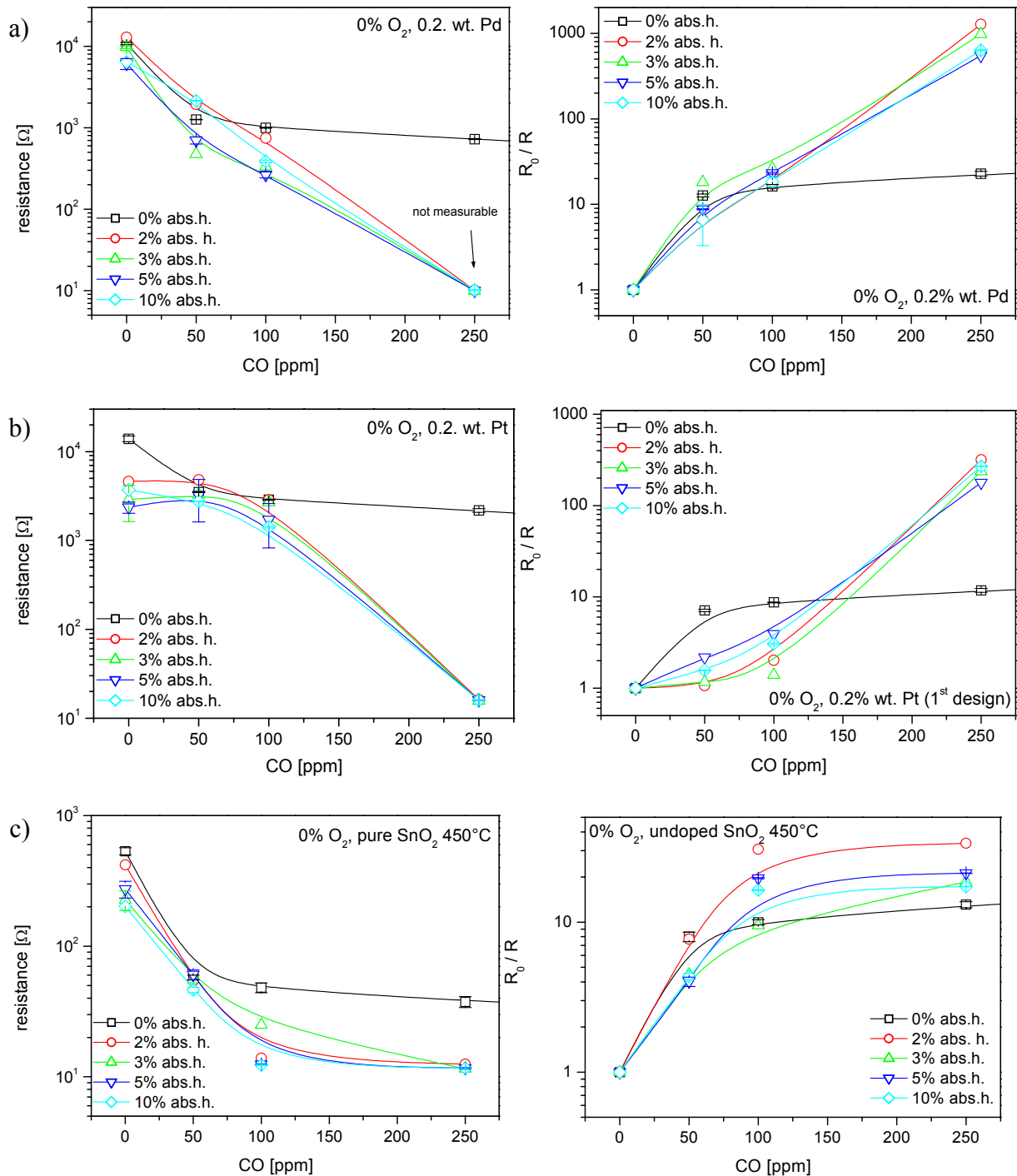
Figure 44: Influence of the ambient humidity on the sensor resistance in nitrogen for 0.2%
w.t. Pd (a) and Pt (b) doped (operation temperature 295°C) and undoped (c,
operated at 350°C) tin dioxide. The sensor signal (left graph) and the sensor
signal (right graph) is plotted vs. CO concentration (0, 50, 100 and 250/500 ppm)
in 0% O_2 and changing absolute humidity (0 - 10%).

Again, for the Pt doped sensor one observes the appearance of a threshold if humidity is present (Figure 44b).

In the case of undoped sensor (Figure 44c) the presence of H_2O did not significantly influence the sensor performance.

4.1.3.3   Propane (C_3H_8) at different oxygen concentrations

Hence, additionally to what was already presented in chapter 4.1.2.1, the influence of different O_2 concentrations on the sensor signals is presented. In Figure 45 the mean values of the sensor signal at 25 ppm C_3H_8 are plotted vs. the absolute humidity for 0, 1 and 5% O_2 (25 ppm was chosen because the differences are especially observed at low concentrations).

One observes again that the sensor signal of the Pd doped sensor is barely influence by the H_2O concentration in the absence of O_2 (Figure 45a). In the presence of O_2, the sensor signal decreases by increasing the H_2O concentration. The sensor signals are higher at higher O_2 concentrations. The lower resistance values compared to the ones shown in chapter 4.1.3.1 are possibly due to the higher H_2O background, which exists because of the shorter purging periods.

The Pt doped sensor (type 1, Figure 45b) shows the same humidity dependence for all O_2 concentrations. The sensor signal measured at 0% O_2 is lower than in the presence of O_2. This was only observed for 25 ppm; at higher C_3H_8 concentrations one obtains the common picture that the highest sensor signal were recorded in the absence of O_2. A possible explanation is maybe again the higher background concentration of O_2 that influences the sensing characteristics at low C_3H_8 concentrations more than at high.

In the case of the undoped sensor (Figure 45c), an increase of H_2O concentration barely changes the sensor signal in the absence of O_2. In the presence of O_2 it is dramatically decreased and there is no visible difference between the amounts of O_2 applied.

For 50 and 100 ppm C_3H_8, the sensor signals measured in the absence of O_2 are generally higher than in the presence of O_2, id est the values obtained at 0% O_2 for doped sensors increases significantly for higher C_3H_8 concentrations. The undoped sensors do not show any change. For all sensor types, between the humidity dependence obtained upon exposure to 50 ppm and 100 ppm C_3H_8 in the presence of O_2 there are no visible differences.

One can conclude that in the case of C_3H_8 the doping material only changes the sensing characteristics in a high humidity background only in the absence or at low O_2 concentrations.

Figure 45: The sensor signal of a 0.2% w.t. Pd (a), 0.2% w.t. Pt (b) doped and undoped (c)
SnO₂ thick film sensor for 25 ppm C₃H₈ is plotted vs. abs. humidity (0 – 10%) at
different O₂ concentrations (0, 1 and 5%). The sensor temperature was 300°C for
the doped and 380°C in case of the undoped sensors.

4.1.3.4 CO at different oxygen concentrations

The dependence of the sensor signals upon exposure to 50 ppm CO and different O_2 concentrations on absolute humidity is shown in Figure 46. No clear trend can be observed for the Pd and Pt doped sensor.

In the case of the undoped sensor (Figure 46c) one clearly observes that the sensor signal decrease with increasing humidity and O_2 concentration. The shapes of the graphs obtained for different O_2 concentrations are identical, which leads to the conclusion that the O_2 does not change the H_2O / CO interaction for undoped SnO_2 sensors. By increasing the CO concentration to 100 and 250 ppm, the differences between sensor signals at different humidity disappear.
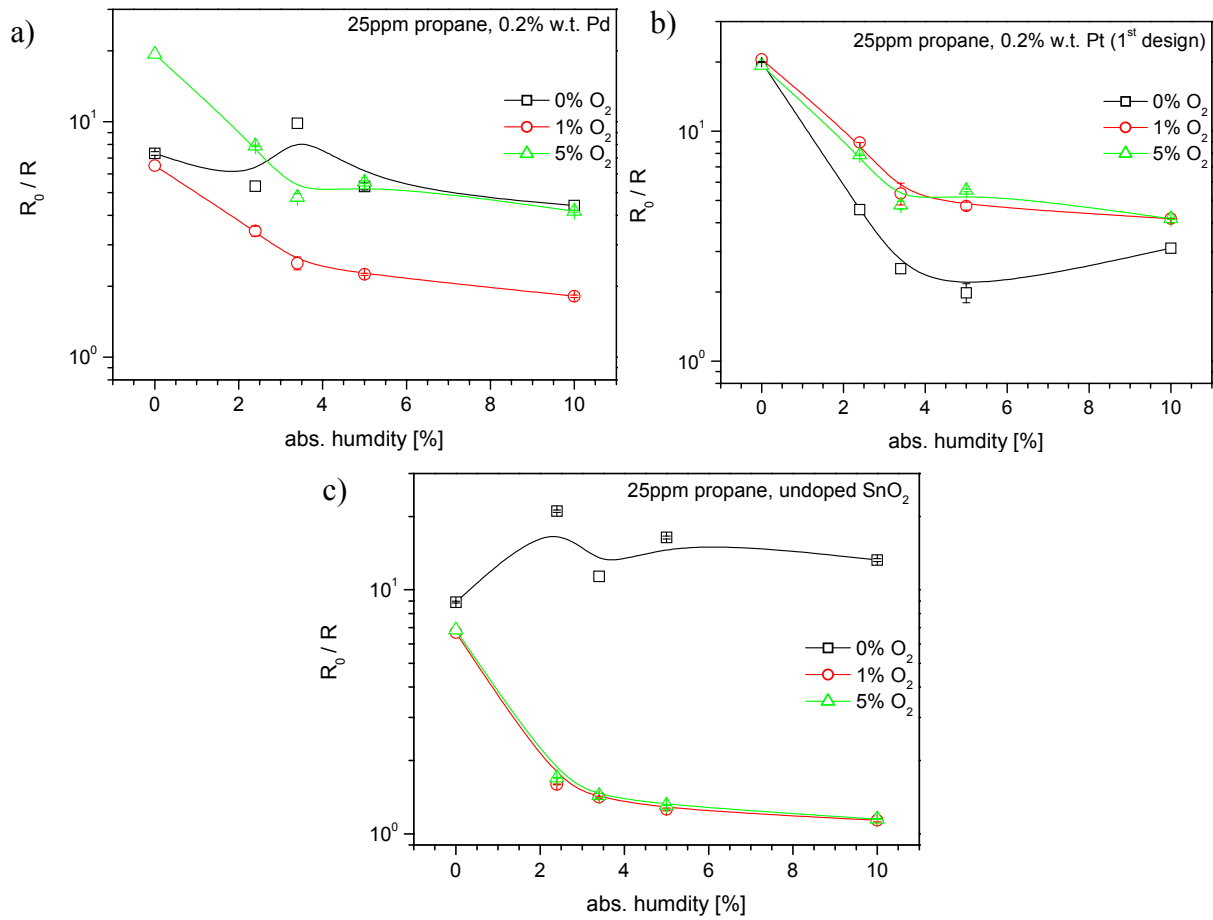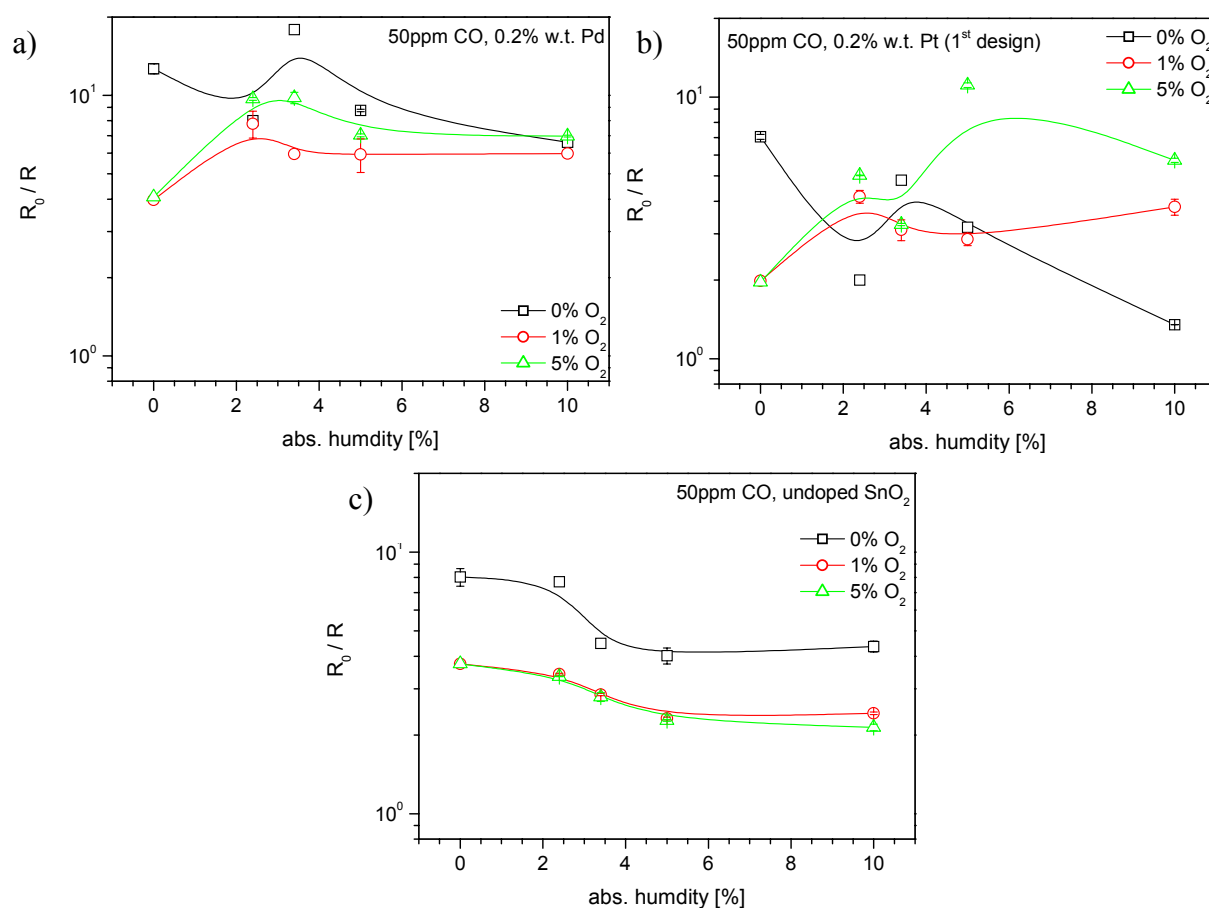
Figure 46: The sensor signal of a 0.2% w.t. Pd (a), 0.2% w.t. Pt (b) doped and undoped (c) SnO$_2$ thick film sensor for 50 ppm CO is plotted vs. abs. humidity (0 – 10%) at different O$_2$ concentrations (0, 1 and 5%). The sensor temperature was 300°C for the doped and 380°C in case of the undoped sensors.

4.1.4 Discussion

In the previous section results were presented obtained upon exposure to CO and C$_3$H$_8$ of differently doped SnO$_2$ thick film sensors at various concentrations of O$_2$ and H$_2$O and at different sensor temperatures. Here, a modeling of the reactions of C$_3$H$_8$ and CO at the SnO$_2$ surface is proposed; the goal is the explanation of the above-mentioned experimental facts. One has to remember that the information contained in the available data is just phenomenological and related to the changes of the free charge carriers; no information about the microscopic interaction is available. Therefore, one needs spectroscopic methods like IR related methods or TDS, MS, etc. to identify the reaction paths. In the following, information obtained from CO and CH$_4$ mechanistic studies (for details and references see chapter 2.2) is used to explain the sensors behaviour in the above-mentioned conditions. Further measurements will have to be carried out to confirm the proposed mechanisms.

4.1.4.1   Propane (C₃H₈) sensing mechanism

At the beginning, a short summary of the empirical findings for C_3H_8 is presented in Table 8. The sensor signal trends are given for Pd (type 1 interdigitated electrodes), Pt doped (type 2, gap electrodes) and undoped SnO_2 sensors. In the table there are rows and lines with the same captions (e.g. O_2). The relations shown in the cells indicate how the sensor signal is changed in the presence e.g. O_2 with increasing O_2 concentration.

Table 8: Dependence of sensor signal for <u>increasing</u> O_2, H_2O concentration and temperature upon C_3H_8 concentration. "I" will indicate an increase in sensor signal, "D" a decrease and for "-", no clear dependency of the sensor signal could be observed. The H_2O concentration was 1020 ppm_v and high H_2O concentration refers to the measurements up to 10% abs. humidity.

	Pd doped SnO₂		Pt doped SnO₂		undoped SnO₂	
	O₂	**H₂O**	**O₂**	**H₂O**	**O₂**	**H₂O**
No O₂	—	D	D	—	I	small I
low/high O₂	—	—	D	—/D	D	D
No H₂O	—	D	D	—	D	small I
High H₂O	small D	small D	—	small D	D	—
Temperature low /high O₂	small I	I/small I	I	I/small I		

4.1.4.1.1   Sensing mechanism in the absence of O₂ and H₂O

By assuming an ideal SnO_2 surface without defects, steps, etc., which can by highly reactive but uncontrollable sites, one has only lattice tin (Sn_{lat}) and lattice oxygen (O_{lat}) atoms. In the case of doped sensors there are deposited noble metal atoms and for clusters present on the surface. As SnO_2 is known to be a weak basic oxide [Mun87] it is assumed that C_3H_8 dissociates to a propyl group and hydrogen either on the SnO_2 surface or on the surface of the deposited noble metal clusters:

$$C_3H_{8,gas} \rightleftharpoons C_3H_{7,ads} + H_{ads} \qquad (19)$$

This dissociation was observed for CH_4 and in the case of C_3H_8 it should be even easier because of the lower bond energies of the CH-bonds (CH_4 431 kJ / mol to C_2H_6 / C_3H_8[1] 410 kJ / mol [Mor86]). H_{ads} acts as donor in combination with lattice oxygen O_{lat} one obtains

---

[1] Higher hydrocarbons posse differently types of CH groups: primary, secondary and tertiary due to the number of C bonded neighbours. The bond energy decreases with increasing number of bonded C groups to the CH bond, e.g. 397 kJ/mol for a secondary bonded H atom.

rooted OH groups (equation 20) or it is possible that a reduction of lattice oxygen takes place at higher temperature (equation 21):

$$H_{ads} + O_{lat} \rightleftharpoons (O_{lat}H)^+ + e^- \qquad (20)$$

$$2H_{ads} + O_{lat} \rightleftharpoons H_2O_{ads} + V_O \qquad (21)$$
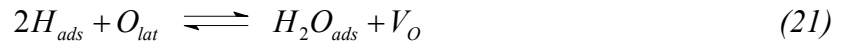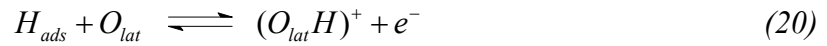
The reaction described in equation 20 introduces electrons in the conduction band leading to a conductance increase respectively a decrease of the sensor resistance. In equation 21 oxygen vacancies are produced, which can diffuse into lattice planes below the surface, acting there as subsurface donors again providing electrons [Mun87]; This mechanism is not considered to play an important role at temperatures around 250°C – 350°C.

The propyl groups adsorbs on a lattice oxygen forming a rooted propoxy-like species and a hydrogen atom (for illustration see Figure 47):

$$C_3H_7 + O_{lat} \rightleftharpoons C_2H_5CH_2O_{lat} + H_{ads} \qquad (22)$$
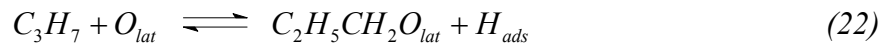
This oxidative coupling was first proposed for CH_4 by Lunsford and it is extensively discussed in reference [Hin84] and [Byt86].
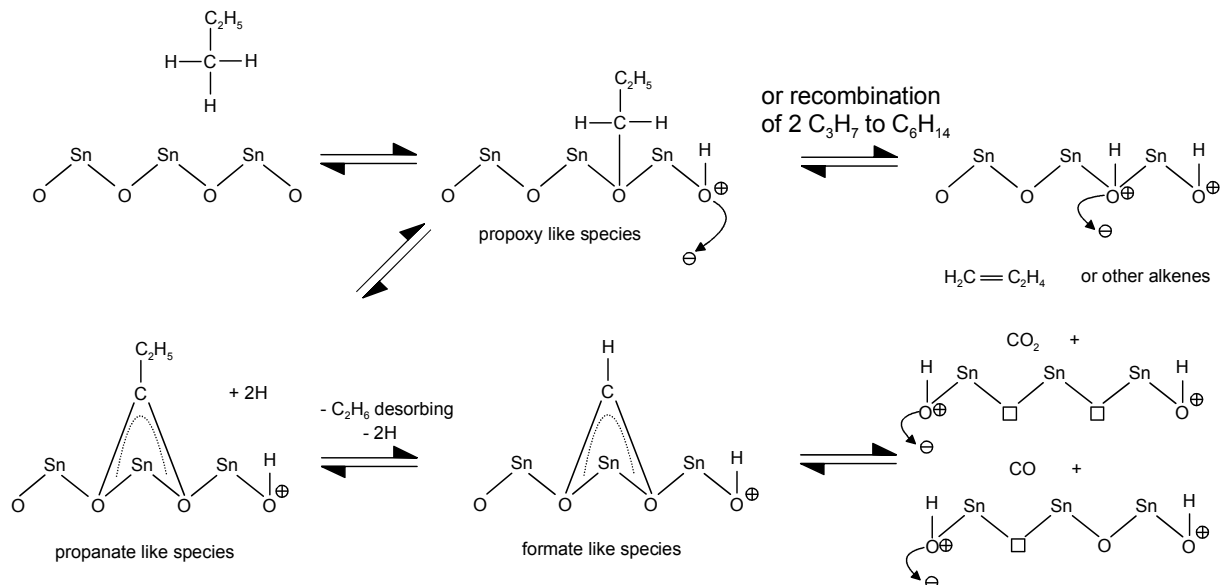
Figure 47: Proposed reaction path of C_3H_8 sensing mechanism on SnO_2 surface in the absence of O_2. C_3H_8 adsorbs on O_{lat} as $C_3H_{7,ads}$ by a homolytic dissociation of the CH bond (primary or secondary). The H atom can adsorb on another lattice oxygen releasing an electron in the conduction band and thus decreasing the resistance. In the following, alkanes can desorb or the propoxy-like species forms with further lattice oxygen rooted propanate – and under ethane desorption a formate-like species can emerge that can be further oxidised to CO or CO_2 leaving oxygen vacancies.

In the case of methane, two adjacent methyl groups combine to form an ethoxy-like species. In the case of higher hydrocarbons this combination is not stringently necessary for a further

reaction or decomposition. In a dehydration process propene can be formed and the remaining hydrogen can remain as adsorbed water or desorb forming an oxygen vacancy:

$$C_2H_5CH_2O_{lat} + H_{ads} \rightleftharpoons H_2O_{lat} + C_3H_{6,gas} \tag{23}$$

$$\rightleftharpoons H_2O_{gas} + C_3H_{6,gas} + V_O$$
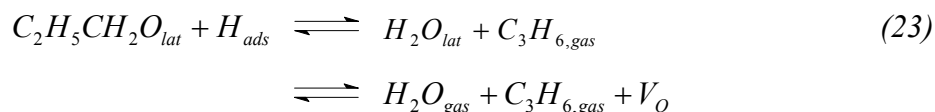
It is also possible that a recombination of two surface propylene groups occurs forming hexylene:

$$2C_3H_7 \rightleftharpoons C_6H_{12,gas} + 2H_{ads} \tag{24}$$

It is also possible that one observes a comparable reaction as mentioned for CH_4 (see Figure 14), combination of two propyl groups forming a hexoxy-like species with lattice oxygen:

$$2C_3H_7 + O_{lat} \rightleftharpoons C_5H_{11}CH_2O_{lat} + H_{ads} \tag{25}$$
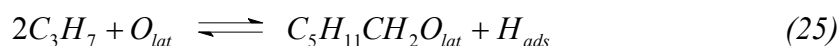
However, it is regarded that its contribution plays only a minor role.

It is also possible that a secondary H atom is separated, if steric hindrance is not too big. This will result in the case of proxy-like intermediate species to the same reaction product – propene - if mainly the formation of alkenes takes place (Figure 48).
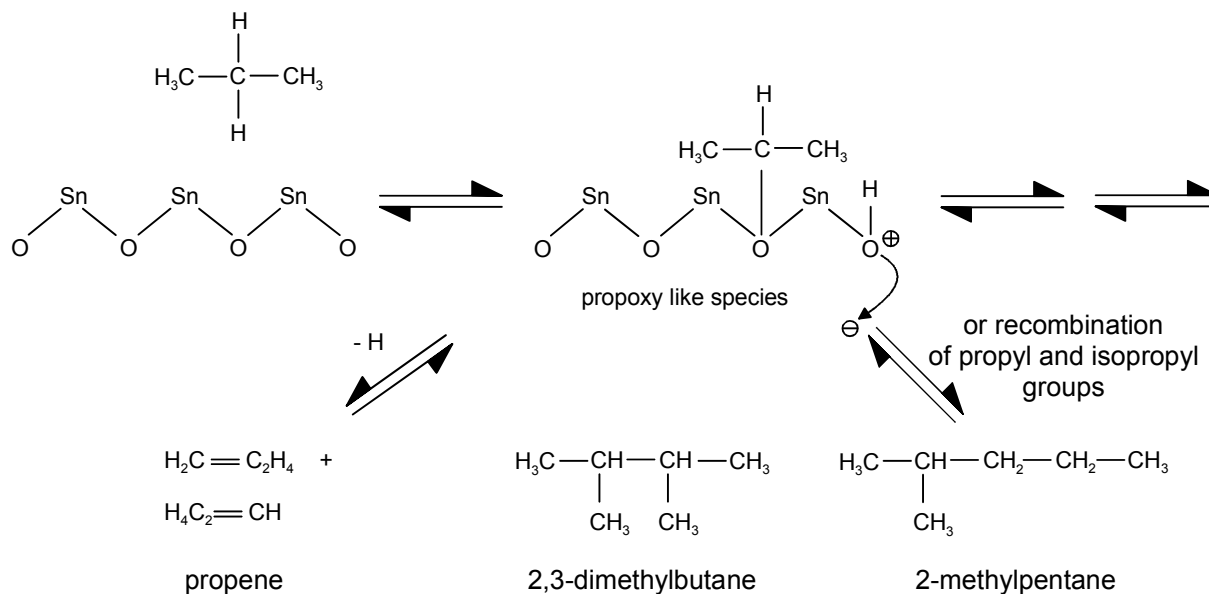
Figure 48: Dissociation of propane to an isopropyl group and a hydrogen atom. The isopropyl group adsorb on lattice oxygen forming a propoxy-like species. In dehydration process propane is formed or the isopropyl group can recombine with another isopropyl group to 2,3-dimethylbutane or with a propyl group to 2-methylpentane. The propoxy-like species can form the propanate-like species already shown in Figure 47.

In the case of recombination – equation 25 – one obtains 2,3 - dimethylbutane or 2-methylpentane. The first appears by a recombination of two isopropyl groups and a propyl and isopropyl group; propyl and isopropyl groups form the second.

In the case of CH_4 the corresponding ethoxy-like species can desorb or react with further lattice oxygen forming acetate- and formate-like species (for CH_4, see Figure 14 (right part) and for C_3H_8, see Figure 47). In this reaction schemes lattice oxygen is removed leaving oxygen vacancies, which can contribute to a conduction increase by diffusing into the bulk and becoming donors. However, it is considered that these mechanisms do not play a mayor role in the gas sensing mechanism below 350°C.

By increasing the sensor temperature the adsorption of propyl groups should be facilitated. The sensor results shown in Figure 33 support this argumentation because by the increase of the temperature from 300°C to 350°C, in the absence of O_2, leads to a strong decrease of the sensor resistance of Pd and Pt doped SnO_2 thick film.

4.1.4.1.2 *Presence of O_2 and H_2O*

In the presence of O_2 the conductance is decreased because of O_2 adsorption on lattice tin that acts as electron acceptor (see chapter 2.2.1):

$$\frac{1}{2}O_2 + Sn_{lat} + e^- \; \rightleftharpoons \; (Sn_{lat} - O)^- \qquad\qquad (26)$$

The presence of adsorbed O_2 also contributes to the sensing mechanisms proposed for CH_4 (see Figure 14 left reaction scheme). Propane can adsorb on O_{ads} forming propoxy-like species. From the propoxy-like species propane can be separated providing another hy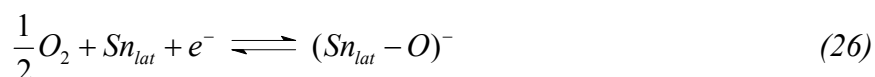drogen atom that can adsorbs on O_{ads}^- or on hydroxyl group/adsorbed water forming adsorbed water or protonated water. The propoxy-like species is able to form with an adjacent O_{ads} a propanate-like species that can desorb by taking back of an adsorbed hydrogen atom (e.g. from a hydroxyl group) or they can decompose completely to CO or CO_2 (Figure 49).

In this reaction a smaller number or no oxygen vacancies are formed. So, in the presence of O_2 a complete decomposition is imaginable. It is however observed that the sensor signal decreases in the presence of O_2. In the latter condition, the hydrogen generated by the adsorption of propane can react with O_{ads} forming hydroxyl groups. These hydroxyl groups can desorb as H_2O if another hydrogen atom is present. The hydrogen atom can be provide by desorption of C_3H_6 or adsorption of another C_3H_8 molecule. This reaction path provides only one electron for the conduction band, whereas in the absence of O_2 two electrons – generated by H adsorption on lattice oxygen can be generated for each C_3H_8 reaction at the surface. The experiment shows that significant amounts of H_2O desorption are found at high O_2 concentrations and temperatures (350°C, see Figure 32). At lower temperatures, the H_2O can be still present, as coordinated water and desorb slowly when the system is purged with N_2.
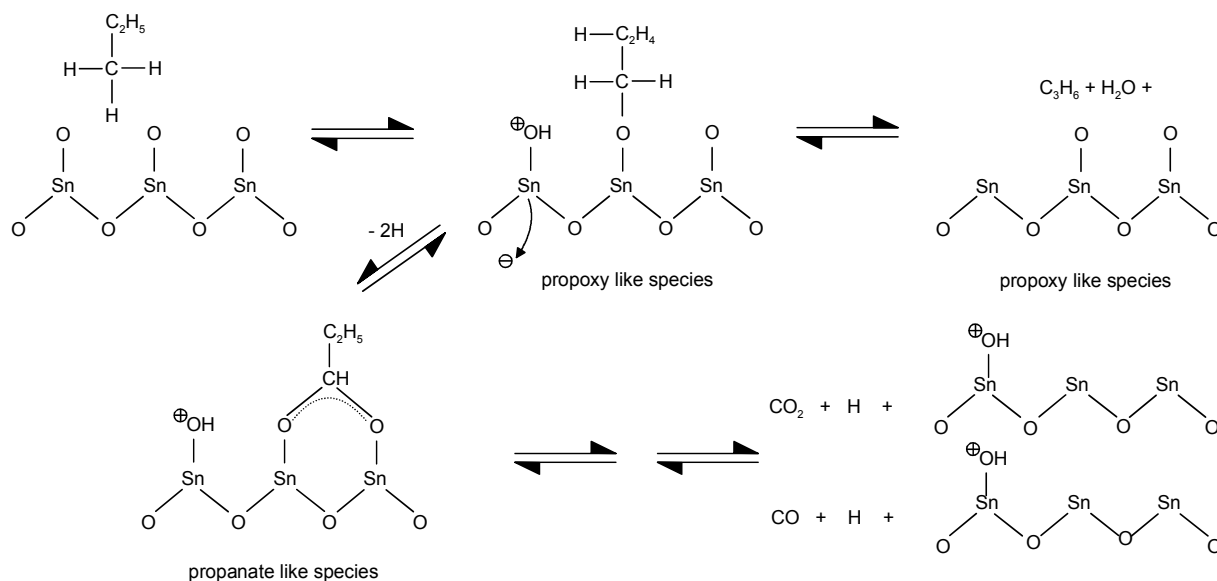
Figure 49: Proposed reaction path of C_3H_8 sensing mechanism on SnO_2 surface in the presence of O_2. C_3H_8 adsorbs on O_{ads} as $C_3H_7O_{ads}$ by homolytic dissociation of the CH bond. The H atom can react with adsorbed oxygen forming a hydroxyl group and releasing an electron in the conduction band and thus decreasing the resistance. In the following alkanes can desorb by dehydrogenation or propanate-like species can be formed with a second O_{ads} under further dehydrogenation. The formate-like species can be further oxidised to CO or CO_2 as shown in Figure 49.

The doping metal also plays a significant role. For undoped and Pt doped sensors no influence of O_2 was observed. For Pt doped SnO_2, it was found that O_2 decreases the sensitivity to C_3H_8.

Gaidi et al. [Gai00] found by means of Auger spectroscopy that the amount of adsorbed oxygen increases with Pt concentration. The measurements indicate that the surface oxygen concentration is even greater than the maximum values that should be obtained if the whole platinum would be oxidized. They also presented results of X-Ray Adsorption Spectroscopy (XAS) measurements where Pt aggregates could be oxidised or reduced depending on the aggregate size and on the gas with which films are put in contact. The larger number of adsorbed oxygen and therefore a higher amount of H_2O generation would explain the decreasing sensitivity in the presence of an increasing O_2 concentration.

The temperature dependence of the sensor signal displayed in Figure 33 for Pd and Pt doped sensor shows that for all O_2 concentrations the sensor signal increases with increasing sensor temperature. That can again be easier attributed to dehydrogenation of C_3H_8 at high temperatures and the generation of a higher amount of oxygen vacancies, which could contribute – as donors - to the conductivity.

In the presence of H_2O the sensor signal decreases for the Pd and undoped sensors. For Pt doped sensors, the signal decreases just at high oxygen concentrations. For all sensors, the water exposure decreases the resistance. This happens due to the forming of two types of hydroxyl groups out of which the rooted one is a donor.

$$H_2O + Sn_{lat} + O_{lat} \rightleftharpoons (OH - Sn_{lat}) + (O_{lat}H)^+ + e^- \qquad (27)$$

As shown in equation 27, H_2O adsorbs on lattice tin and O_{lat}, where the latter is also the reaction site for the C_3H_8 adsorption. Consequently, one can state that the sensor signal decreases with increasing H_2O concentration because of a smaller number of possible adsorption sites (competitive absorption between water and propane)

This doesn't work for the Pt doped sensors at low O_2 concentrations. In the case of Pt doped SnO_2 sensor the presence of H_2O does not have a significant influence on the sensor signal at low O_2 concentrations but at high O_2 concentration the sensitivity is nearly cancelled. A possible explanation therefore is that in the case of Pt, the activation of the C_3H_8 adsorption on adsorbed oxygen is – from the energetic point of view – no longer so advantageous because of the formation of hydroxyl groups in the presence of H_2O.

Summarizing, it is proposed that the sensor signal for C_3H_8 is derived by C_3H_7 adsorption and a further recombination or dehydrogenation generating alkanes and alkenes. In the presence of O_2 the sensor signal is decreased due to H_2O formation. In the case of H_2O one obtains the same picture for Pd doped and undoped SnO_2 sensors as for the presence of O_2, but the Pt doped sensors show a different sensing trends in the presence of O_2, H_2O and mixtures of both.

4.1.4.2 CO sensing mechanism

A short summary of sensor signal dependencies upon CO exposure in the presence of different O_2 and H_2O concentration is given in Table 9 for Pd, Pt doped and undoped SnO_2 thick film sensors. The trends are given for the same sensors and are presented in the same way as for C_3H_8.

Compared to C_3H_8, the sensing characteristics of CO are better investigated. Most results were obtained by using UHV methods, which identified the reactive species of CO interaction with the SnO_2 surface (see 2.2.3), but as already mentioned, measurements carried out in the absence of O_2 on SnO_2 sensors at normal pressure are rare.

In the following, the possible sensing mechanism in the absence respectively presence of O_2 and H_2O are discussed. It was already pointed out in chapter 4.1.1 that the influence of the dopant plays an important role especially at low O_2 concentrations (ppm range). Firstly, a

general sensor mechanism common for all sensors will be proposed and than, as far as possible, the interaction with Pd and Pt as noble metal dopants will be discussed.

Table 9: Dependence of sensor signal for <u>increasing</u> O_2, H_2O concentration and temperature upon CO concentration. "I" will indicate an increase in sensor signal, "D" a decrease and for "-", no clear dependency of the sensor signal could be observed. The H_2O concentration was 1020 ppm_v and high H_2O concentration refers to the measurements up to 10% abs. humidity.

	Pd doped SnO_2		Pt doped SnO_2		undoped SnO_2	
	O_2	H_2O	O_2	H_2O	O_2	H_2O
No O_2	D	I	D	I	D	D
low/high O_2	D	D	D	D	—	D
No H_2O	D	D	D	—	D	D
Hihgh H_2O	D	—	D	—	D	—
Temperature low /high	D/I	D/I	D/I	D/D		

4.1.4.2.1 Sensor mechanism in the absence of H_2O and O_2

The CO interaction with SnO_2 has been widely studied by means of UHV methods (see [Koh88] and the references therein). Thoren et al [Tho85] showed with the help of TDS studies that CO desorbs from SnO_2 mainly as CO; only a small fraction forms CO_2 by consuming lattice oxygen:

$$CO + O_{lat} \rightleftharpoons CO_2 + V_O \qquad (28)$$

No CO_2 desorption maximum appears up to 800°C and conductance measurements were not performed. As mentioned before, the formation of oxygen vacancies do not match with the fast response and recovery times observed in the measurements. Another reason is that no large amounts of CO_2 were detected in the absence of O_2.
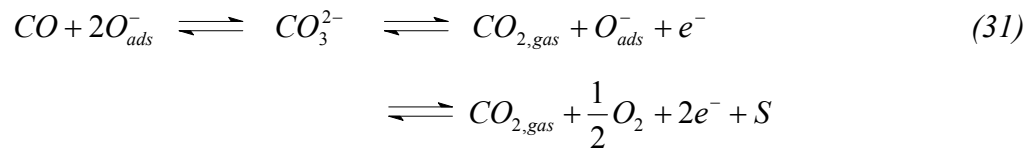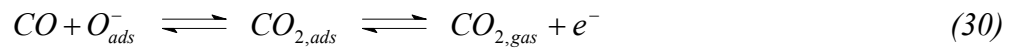
In order to explain the high sensitivities found in the absence of O_2 one has to consider another interaction of CO with the SnO_2 surface, which increases the conductivity. The most probable explanation is the adsorption of CO as a donor causing the resistance decrease:

$$CO_{ads} \quad \rightleftharpoons \quad CO_{ads}^+ + e^- \qquad\qquad (29)$$

4.1.4.2.2 Sensor mechanism in the presence of H_2O and O_2

In the presence of O_2, O_{ads}^- is found as main adsorbed species at operation temperatures above 200°C (see chapter 2.2.1). It is generally accepted that CO interacts with O_{ads}^- to carboxylate (equation 30) and bidententate carbonate (equation 31) releasing electrons in the conduction band and thus decreasing the conductance of SnO_2 [Koh88][Bâr93]:

$$CO + O_{ads}^- \quad \rightleftharpoons \quad CO_{2,ads} \quad \rightleftharpoons \quad CO_{2,gas} + e^- \qquad\qquad (30)$$

$$CO + 2O_{ads}^- \quad \rightleftharpoons \quad CO_3^{2-} \quad \rightleftharpoons \quad CO_{2,gas} + O_{ads}^- + e^- \qquad\qquad (31)$$

$$\rightleftharpoons \quad CO_{2,gas} + \frac{1}{2}O_2 + 2e^- + S$$

The results show that the sensor signal decreases in the presence of O_2, which was also found by Giber et al. [Gib94] for high temperature semiconductor gas surfaces like $SrTiO_3$ operated at 550 – 850°C. They investigated CO interaction dependence at "lower" O_2 (1 and 5%) and H_2O (3% r.h.) concentrations. They also found that upon exposure to a 1% CO the measured sensor resistance is a function of the O_2 concentration.

According to this observation, described in chapter 4.1.1.1.1, one can suggest that at low O_2 concentration, where only a small number of possible oxygen adsorption sites are occupied, CO still reacts with SnO_2 in the same way as in the absence of O_2 (see Figure 50). At 250 ppm CO, saturation occurs because all sites are occupied. At higher ppm O_2 concentrations CO can not occupy all possible sites and the sensor signal is composed out of the direct chemisorption of CO and the reaction of CO with adsorbed oxygen. The result is a "linearity" of the sensor signal and a net decrease of the sensor signal below 250 ppm CO. This fact is not easy to explain, because both reactions release one electron. One reason could be that the activation energy for CO_2 formation (equation 31 and 32) is higher than for the CO adsorption directly on SnO_2 (equation 30) and in this way some of the CO that reacts with adsorbed oxygen is blocked from "electrical" point of view.

By increasing the O_2 concentration to 25 or 50 ppm, the same sensor signal is measured as at 0 or 10 ppm, this allows for the conclusion that CO occupies all possible adsorption sites and, additionally, a reaction takes place with adsorbed O_2. At high O_2 concentration, CO reacts mainly with adsorbed oxygen to CO_2 – a CO_2 IR device monitored this – and only small amounts are adsorbed at the surface.
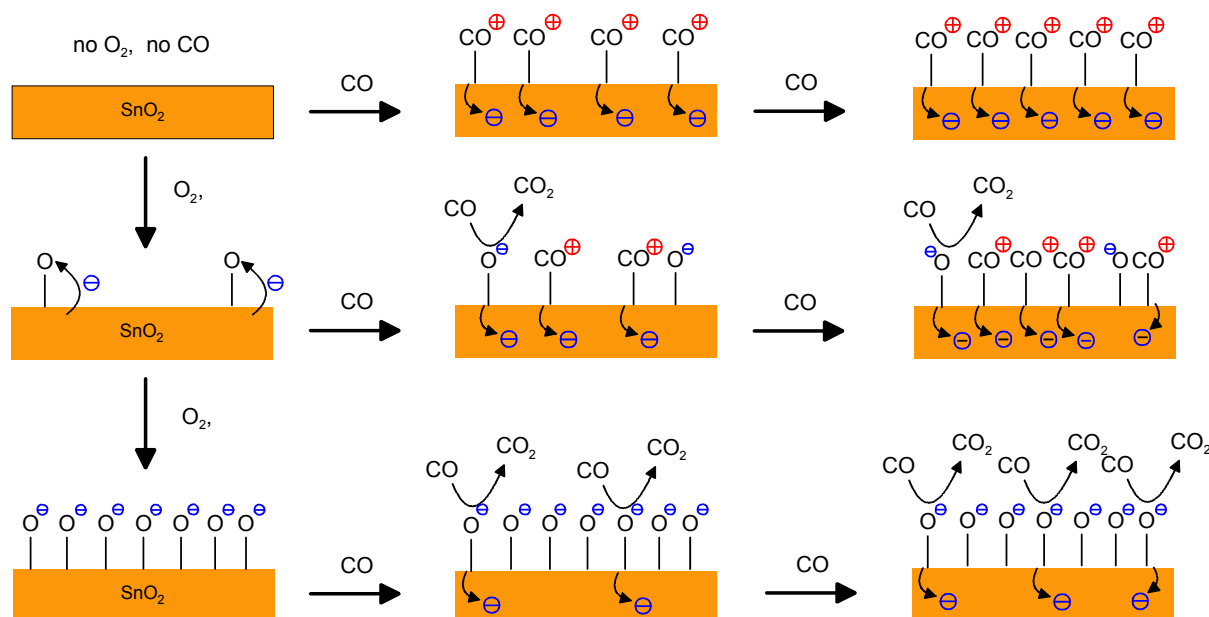
Figure 50: Schematic representation of the oxygen dependence of the sensor signal. In the absence of O_2, CO adsorbs as electron donor and leads to a decrease of the sensor resistance. In the presence of O_2, O_2 adsorbs by increasing the resistance. By exposure to CO, some CO molecules react with adsorbed oxygen and some are adsorbed depending on the O_2 and CO concentration. At high O_2 concentration the sensor signal decrease significantly and large amounts of CO_2 are detected.

From this, one can conclude that the sensing behaviour of CO can, in a simple way, be explained by parallel and competitive reaction with SnO_2 and with adsorbed O_2. The mechanism is further backed by the temperature dependence recorded at high O_2 concentration. There, the sensor signal increases nearly "linear" for both sensor with about one order of magnitude by increasing the sensor temperature from 250°C to 350°C (see Figure 36). At 350°C the values measured for 1 and 5% are identical, which suggests that the maximum number of oxygen adsorption sites are occupied.

For Pt doped sensor the same trends are visible but with higher sensitivity. Small differences are observed at 25 and 50 ppm O_2 where the rate of CO adsorption or conversion[1] is increased, no "linearity" is reached as in the case of the Pd doped SnO_2 sensor. Thus, one can conclude that the Pt activates the reactants differently so that the reaction with O_{ads} is energetically advantageous. This would also explain the difference observed in C_3H_8 sensing. Gaidi et al., who investigated the role played by the Pt aggregates, describe the CO oxidation in terms of a catalytic processes [Gai00]. They report that in the system air/CO(in air), which is the normal condition of the sensor working, a spillover and an electronic effect are

---

[1] The measurement set-up used could not specify this. Usage of separate sensor chambers equipped Pt doped sensor and a sensitive CO_2 would identify the reaction products.

responsible for the electrical response, respective at high and low temperature. In the system with lower O_2 concentration (reduced by applying CO in N_2), they proposed that, firstly, a spillover effect occurs between CO, chemisorbed oxygen and PtO_y aggregates, and, secondly after a period of time that depends on the temperature, the platinum is reduced. Additionally it was shown by Yamazoe and Matsushima et al. [Yam91] and [Mat88a] that for Pt interaction, the spillover process (for detailed information see chapter 2.3.5.1) dominates. Pd on the opposite acts – according to this investigation - mainly by electronic interaction, id est. by Fermi level control.

In the presence of H_2O, hydroxyl groups (Sn-OH and HO_{lat}) and H_{ads} are present at the sensor surfaces that serve as additional reaction sites for CO interaction:

$$CO + HO_{ads} \; \rightleftharpoons \; HCOO_{ads} \; \rightleftharpoons \; CO_2 + H_{ads} \qquad\qquad (32)$$
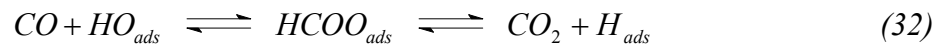
CO can interact with HO_{ads} and be oxidized to formate ($HCOO_{ads}$) [Koh89] but this reaction does not change the conductivity. Formate is known t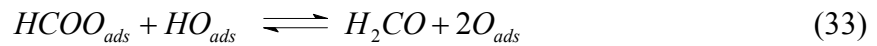o be stable on polycrystalline SnO_2 up to 230°C [Har85]. Above 230°C the formate can decompose to CO_2 and hydrogen and hence increase the conductivity (see equation 20) or react with another hydroxyl group to formaldehyde [Voh86] providing in this way two adsorbed oxygen atoms:

$$HCOO_{ads} + HO_{ads} \; \rightleftharpoons \; H_2CO + 2O_{ads} \qquad\qquad (33)$$

Equation 33 leads to a sensor conductivity decrease and not to an increase that was observed in the absence of O_2.

It is also interesting that in the presence of water there is a difference of the doped sensor. The Pd doped sensor generally shows, in the absence of O_2, higher sensor signals as the Pt doped one. At 250°C there is a threshold for Pd doped sensor while for the Pt doped sensor there is the maximum sensor signal. It is striking that the sensor signal trends for Pd and Pt doped sensors are different in the presence of water; this can explained by their different way of influencing the SnO_2 electrical properties. Yamazoe et al. reported that Pd and not Pt affect the work function of SnO_2 (increase of around 0.3eV) that leads to a strongly electron-depleted space charge layer inside the semiconductor [Yam91].

In the presence of both O_2 and H_2O one observes that the sensor signal decrease with increasing O_2 concentration. The trends in the graphs of Pd and Pt doped sensors (Figure 40 and Figure 41) did not change significantly, which suggest that reactions analogue equations 30 and 31 take part to a larger extent. It also possible that formyl groups react with adsorbed oxygen or lattice oxygen to form formate. A bigger rate of equation 33, which takes place at

higher temperature, would explain the decrease of the sensor signal with increasing temperature.

4.2   Discrimination of CO or CH$_4$ mixtures in varied relative humidity

CO, CH$_4$ and their mixtures were measured with a sensor array consisting of different SnO$_2$ gas sensors operated at different temperatures and measured with varying humidities (see 3.3.1.2). The obtained data – id est sensor resistance values and sensor signals (R$_0$ / R) - are presented first. Based on this – in respect of sensor measurements - relatively huge data set, different multivariate data evaluation methods have been carried out to qualify and quantify CO, CH$_4$, and their concentrations. For data discrimination, Principle Component Analysis (PCA) was used. Determination of the concentration was first performed by a linear regression method (Principle Component Regression, PCR) and by other regression methods like Fuzzy Inference Systems (FIS) to try to improve the results.

The aim was to determine the possibilities of discrimination/quantification of CO or CH$_4$ in the presence of the other and within an interfering water background.

4.2.1   Sensor performance

The graphs measured in **air** for CO and CH$_4$ look like the ones already presented in chapter 4.1 (high O$_2$ concentrations) and later in chapter 4.3. Therefore, only one graph is shown for CO and CH$_4$, which presents the measured resistance respectively conductance (G = 1 / R) of CO and CH$_4$ mixtures at different humidities. In Figure 51 the conductance (G = 1 / R) of a sensor type 3 (2% wt. Pd, C3.0) is plotted versus the CO concentration measured in the presence of different CH$_4$ concentrations (400, 1500 and 5000 ppm) and relative humidity levels (0, 30 and 50%). The sensors shown here were operated around 400°C.

In the diagrams, the average conductance of 8 measurements and their standard deviations are plotted.

One observes that the sensor conductance in air increases by:

- Increasing the relative humidity, because the number of available reaction sites/partners for CO increases and so an enhancement of the sensor signal is observed [Kap99].
- Increasing the background concentration of CH$_4$, because more analyte will react on the sensor surface.

As it can be seen in Figure 51, the reproducibility – indicated by the standard deviation - of the sensor signal is very good in all cases. The behaviour of the sensor conductance at a sensor temperature of 350°C is similar, but the absolute values are smaller.

Figure 51: Mean of conductance of sensor type 3 (C3.0, 0.2% w.t. Pd doped) operated at 400°C. The sensor was exposed to a mixture of CO and CH₄ (0, 3, 7 and 14 ppm CO and 0, 400, 1500 and 5000 ppm CH₄) in different relative humidities (0, 30 and 50%).

The calibration curves (sensor signal R_0 / R) of 2% w.t. Pd doped sensor in different conditions are shown in Figure 52. The sensor signals increases by increasing CH_4 and CO concentration. For CH_4 the sensor signal decreases when the relative humidity increases. This results from competitive reactions between CH_4 and H_2O (see chapter 4.1.2.1). The increasing amount of water decreases the probability for a reaction between CH_4 and surface lattice oxygen.

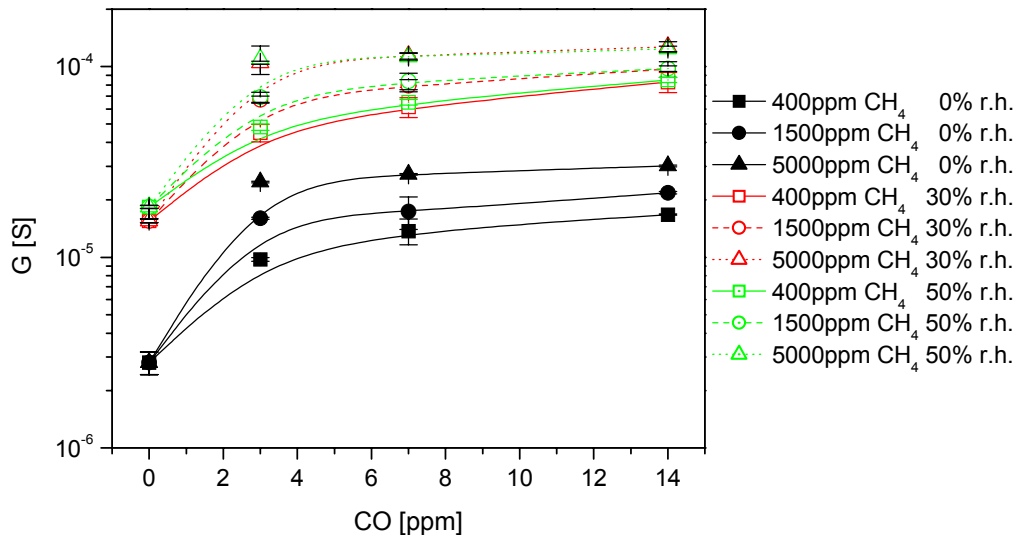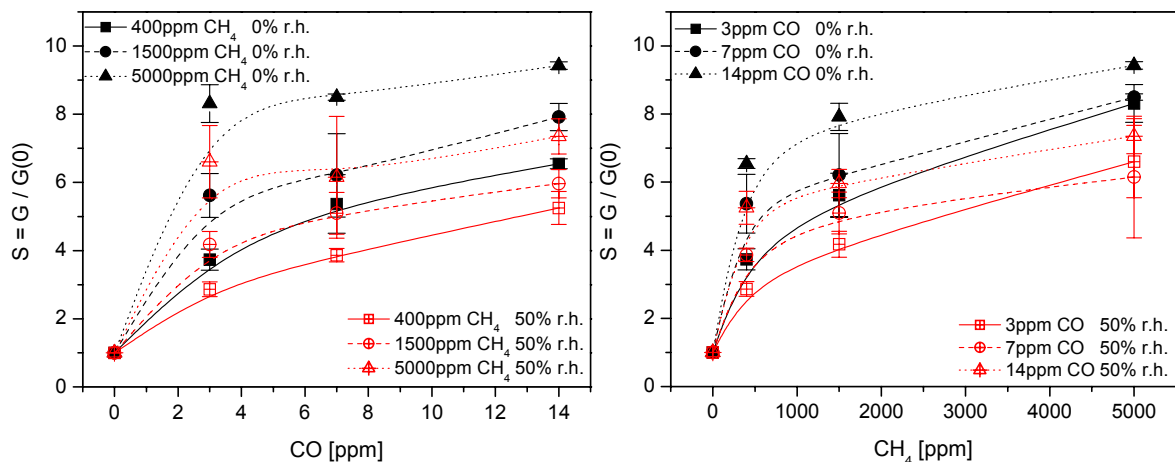*Figure 52: Mean of sensor signal of sensor type 3 (C3.0, 2% w.t. Pd doped) operated at 400°C. The sensor was exposed to a mixture of CO and CH₄ (0, 3, 7 and 14 ppm CO and 0, 400, 1500 and 5000 ppm CH₄) in different relative humidities (0 and 50%). On the left side, the dependency of the CO concentration on CH₄ is shown and there is the same plot on the right side for CH₄ with CO background.*

4.2.2 Multivariate data analysis

4.2.2.1 Classification by Principle Component Analysis (PCA)

The performance of the sensor array was checked using a <u>P</u>rinciple <u>C</u>omponent <u>A</u>nalysis (PCA) [Man86]. In the PCA a full cross validation was done on all 8 data sets for different mixtures and relative humidities at one sensor temperature.

The results of a PCA (feature: conductance) are shown in Figure 53 for different CO (left side) and CH_4 (right side) concentrations at different humidities. This kind of investigation – discrimination and prediction of single compounds - has been carried out for some sensor systems several numerous times [Hah99]. In the following, the results are presented in a very compact manner. The focus is put on the discrimination of mixtures with humidity as interfering gas. The scores[1] plots in Figure 53 show that for both compounds data measured in the presence of humidity can be clearly discriminated from data measured in the absence of humidity. It can be seen that low CO concentrations are better discriminated than higher ones. For CH_4 it is the opposite, a better discrimination is obtained at high concentrations. This is due to the different slopes of the calibration curves.
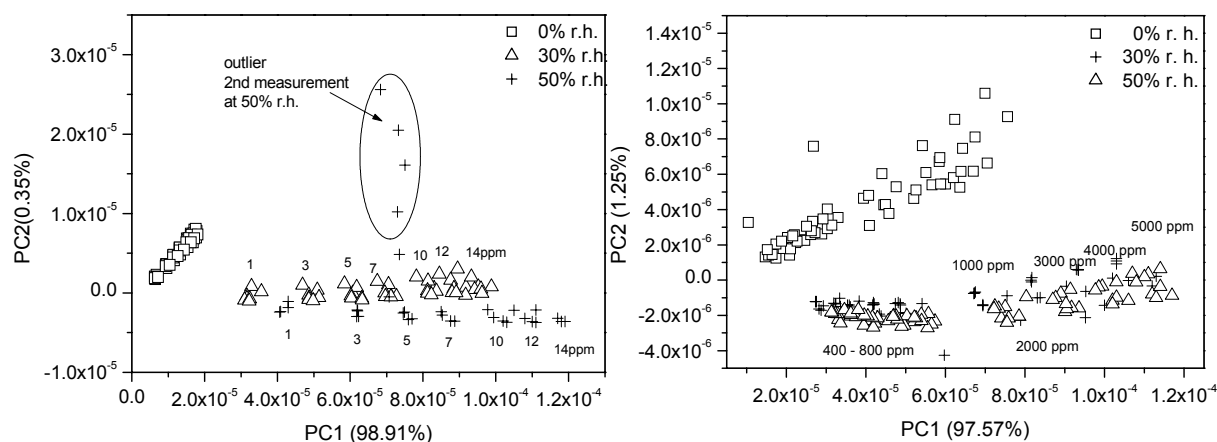
Figure 53: PCA (full cross validation; feature: conductance) of different CO (left) and different CH_4 (right) at different relative humidities (0, 30 and 50%).

Another PCA was carried out using CO as well as CH_4 data. A relative conductance – G_{CO} / G (7 ppm CO) and G_{CH4} / G (1500 ppm CH_4) – was chosen as feature, in order to have comparable values for CO and CH_4 sensing in the different humidities. A clear discrimination of the CO and CH_4 by the PC2 (5.27%) was found (Figure 54). In the case of CO, the sensor array is able to discriminate 0% r.h. values from 30 and 50% r.h. Reminding the results and discussion in chapter 4.1.2.1.1, dealing with the humidity dependence of the CO sensing

---

[1] The scores describe the data structure in terms of sample patterns (here the conductance of the different mixtures), and more generally show sample differences or similarities.

mechanism in contrast to CH_4, this finding is reasonable. This holds especially having in mind that the sensor with the main influences are heavily doped (2%w.t.) Pd, a doping material that showed an increase in the sensor signal in the presence of H_2O
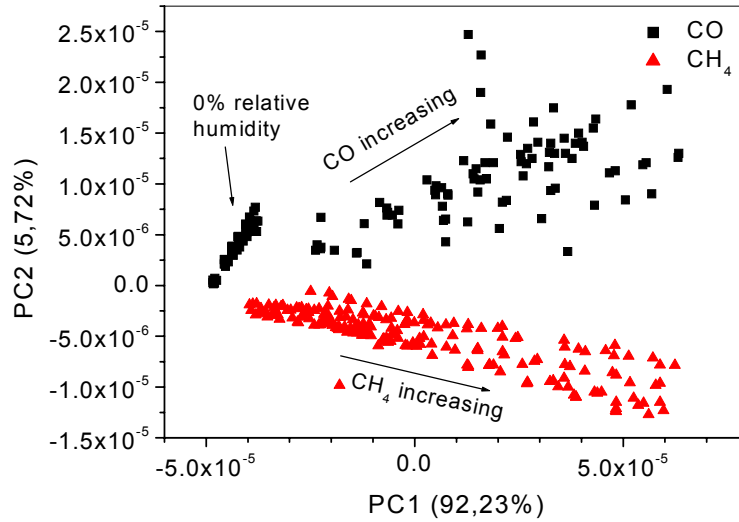
Figure 54: PCA of relative conductance of all CH_4 (400 - 5000 ppm) and CO (1 - 14 ppm) concentrations in 0%, 30% and 50% r. h. (sensor temperature: 350°C).

The scores plot of a PCA carried out on the datasets of the CO/CH_4 mixtures at a sensor temperature of 350°C is shown in Figure 55. Again, the conductance was chosen as feature for the PCA.

The discrimination between the different CO concentrations is mainly done by the PC1 (91,9%), but the information of the PC2 is additionally needed to improve the results. The same is valid for CH_4. The values measured at 0% relative humidity are more clustered together than the ones obtained at a certain relative humidity. The discrimination of CO is the best in low CH_4 background (0, 400 and 1500 ppm) and 30% or 50% relative humidity. In the presence of a high CH_4 background (5000 ppm), the calibration curve shows already a tendency of saturation and therefore the discrimination is poor.
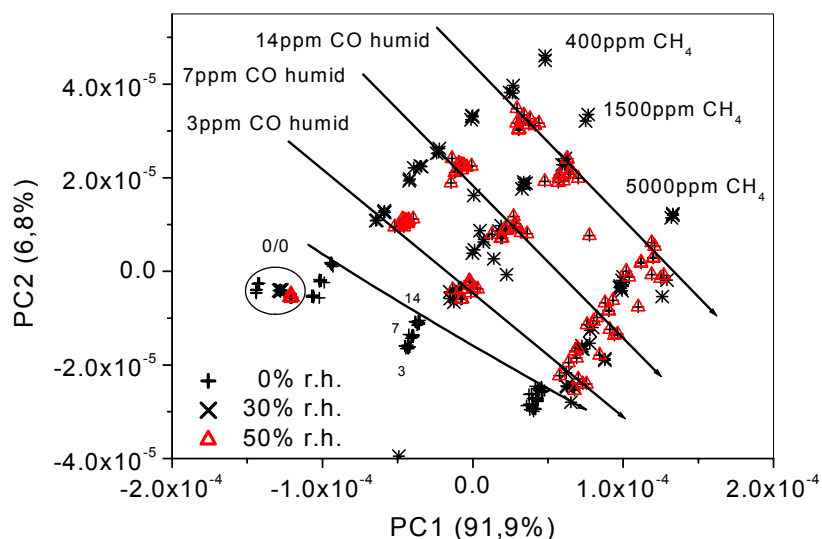
Figure 55: PCA (full cross validation; feature: conductance) of mixtures of CO and CH$_4$ (0, 3, 7 and 14 ppm CO; 0, 400, 1500 and 5000 ppm CH$_4$) at different relative humidities (0, 30 and 50%).

The loadings of the different sensors are specified in Table 10. They describe the data structure in terms of correlations of variables (here sensors). Each variable/sensor has a loading on each principle component (PC), which shows both: how much the variable contributed to that PC; how well that PC takes into account that variable.

Table 10: Sensor loadings obtained by a PCA of conductance data measured for CO (3, 7 and 14 ppm) and CH$_4$ (400, 1500 and 5000 ppm) mixtures at a sensor temperature of 350°C.

Sensor	PC1 (91,9%)	PC2 (6,8%)
C1.1[1]	0,171	0,339
C3.1	0,520	0,759
C2.1	0,705	-0,526
C3.0	0,450	-0,181

Table 10 shows that sensor C2.1 (0.2% w.t. Pd) and sensors C3.x (2% w.t. Pd) contribute the most information for the PC1. One has to mention that sensors 3.0 and 3.1 have the same coating, but were operated at different temperatures (temperature difference around 50°C). Sensor C1.1 (0.2% w.t. Pd without calcination procedure) has only a little influence on the PC1 and some on the PC2. By calculating the PCA again without sensor C1.1 one gets nearly the same results.

---

[1] The 1st number indicate the type of sensor, the 2nd is the individual one.
C1.x is 0.2% w.t. Pd doped, C2.x and C2.x are 0.2% w.t. and 2% w.t. Pd doped followed by calcinations.

The results obtained for a sensor temperature around 400°C look fairly the same; the only change was found in the loadings: The influence of sensor C2.1 on the PC2 is negligible (-0.08) and sensor C3.0 has a larger influence on both PCs.

4.2.2.2   Quantification by Principle Component Regression (PCR)

One of the most popular regression methods for multivariate data analysis is the Principal Component Regression (PCR) [Mas65], because of its straight forward application and interpretation of the results.

A PCR was carried out in order to determine the amount of CO or CH_4. Five datasets were used for calibration (full cross validation) and three independent datasets for prediction. Here, the squared conductance (G^2) was used as feature, since the conductance is proportional to the square root of the partial pressure. All sensor signals were set as 1st variable and the concentrations of CO and CH_4 were set as 2nd variable. The samples chosen for evaluation were measured at the same humidity level. Including all the humidity data, especially 0% r.h., the results were not that good. An overview is given in Table 11. The best results were obtained by using the data measured at 30 or 50% relative humidity.

Table 11: Mean prediction error of different CO or CH_4 concentrations in varying CH_4/CO and humidity (0%, 30 and 50%) background.

CH_4 [ppm]	Error of CH_4 prediction			CO [ppm]	Error of CO prediction		
	0% r.h.	30% r.h.	50%r.h.		0% r.h.	30% r.h.	50%r.h.
400	31.1%	5.5%	7.2%	3	9.9%	12.9%	9.4
1500	8.5%	7.4%	13.4%	7	149%	24.9%	0.97%
5000	2.8%	6.0%	3.7%	14	378%	55.5%	11.8%

The mean predicted CH_4 concentrations and their standard deviations of CH_4 in a varying CO background are shown in Figure 56 (left side) at 50% relative humidity. The standard deviations are small for 0, 400 and 1500 ppm CH_4. The larger standard deviation at 5000 ppm is probably due to the fact that the sensors are nearly saturated and one faces a saturation effect.
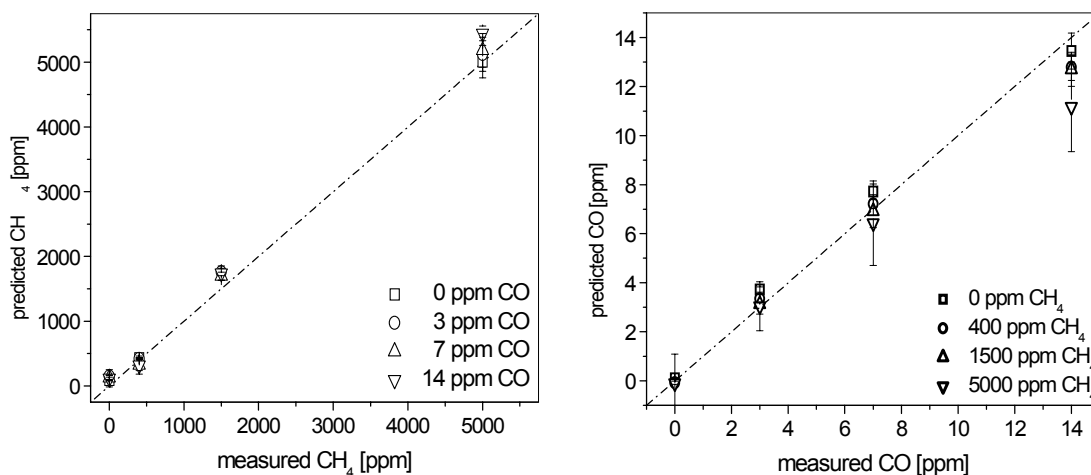
Figure 56: Prediction of 3 independent test datasets of CH$_4$ in the background CO (left) and for CO in the background CH$_4$ (right). The PCR was carried out by a full cross validation (with 5 datasets) with the G^2 as feature. The sensor temperature was 400°C and the relative humidity 50%.

The prediction of CO in a varying CH$_4$ background at 50% relative humidity is shown in right side of Figure 56. The results for low CH$_4$ background are quite good and gets worse when the CH$_4$ concentration is higher than 1500 ppm. In Table 11 the mean prediction errors are listed.

The best results for the prediction of CO were obtained at a relative humidity of 50%. Water adsorption provides a larger number of reaction sites for CO and thus increasing the sensitivity to CO (see chapter 2.2.3.1) in a synthetic air background. The presence of water reduces the sensitivity to CH$_4$ because of the competitive adsorption of H$_2$O and CH$_4$, thus the cross sensitivity for CO sensing is decreased. Therefore, the mean errors at 30% r.h. are generally lower for CH$_4$ and higher for CO if they are compared to the values obtained at 50% r.h. The values for CH$_4$ are acceptable but for CO they are not acceptable and are even getting worse in dry synthetic air (Table 11). In the latter case, the higher sensor signals for CH$_4$ dominate. In the PCR plot, one gets three parallel graphs for the different relative humidities, with distances of 1.5 ppm CO (0% r.h. $\Rightarrow$ 30% r.h.) and 6 ppm (30% r.h. $\Rightarrow$ 50% r.h.). The prediction results for CH$_4$ in the presence of changing CO concentrations is generally good in all conditions (on an average around 10%).

4.2.2.3   Quantification by other methods

The research group of De Marco (Instrumentation and Communications Systems of the Electronics department at the University of Barcelona, Spain) carried out a comparison of different regression methods based on the same data sets [Sun02]. The input data sets consisted of all CO, CH$_4$ concentrations, mixtures, humidities and temperatures (5 sensors at

two different temperatures $\Rightarrow$ 10 variables). They used the three most common linear regression methods: Partial Least Squares (PLS) [Wol75], PCR and Multivariate Linear Regression (MLR) and methods based on Fuzzy Inference Systems (FIS [Glo99], [Llo99], [Ron00], [Tak85], [Lan97]). Fuzzy inference systems like Artificial Neural Networks (ANN) are universal approximators, which are able to handle non-linear data very well and are also quite robust to noise. Two kinds of FIS were carried out: a grid FIS and a free FIS. In the grid FIS a prediction model is built for each gas, which is used to determine concentration of the test data set. In a free fuzzy FIS no conditions are given [Chi94].

The results obtained for the different regression methods are contrasted in Table 12. There, the absolute Root Mean Square (RMS) errors calculated for the whole measurement range (CO 0 - 14 ppm, CH_4 0 – 5000 ppm) are listed for an optimised training data set[1] and an independent test data set. It can be clearly seen, that the prediction is improved for CO as well as for CH_4 by using non-linear regression methods. The errors obtained in a changing humidity background are still higher than the ones obtained at constant humidity background, so that there is still a need for improvements. Optimising the material and measurement parameters for this application or evaluation method can do this.

Table 12: Absolute root means square errors in % for CO and CH_4 prediction for an optimised training data set and test data set obtained by linear (PLS, PCR an MLR) and non-linear (grid/free fuzzy) regression methods. The input data sets contain all mixtures and humidity concentrations [Sun02].

	PLS	**PCR**	**MLR**	**Grid Fuzzy**	**Free Fuzzy**
CO, Training set	25%	24%	21%	15%	3%
CO, Test test set	36%	34%	64%	27/	22%
CH_4, Training set	25%	27%	13%	34%	16%
CH_4, Test test set	33%	37%	30%	26%	24%

4.2.3 Summary

With the presented sensor array one obtains reproducible sensor signals. The differences in the sensor signal between 30% and 50% relative humidity are small. The array is able to discriminate between CO and CH_4 in varying relative humidity backgrounds. By exposing the array to mixtures of CO and CH_4, one could see by using a PCA that the pattern of the sensor signals is different for different mixtures. The pattern for different relative humidities is the

---

[1] The optimised training data set consists of a selection of variables (here sensors and their operation temperature) to reduce the noise.

same with a large difference between 0 and 30/50% relative humidity. For a good classification, only C2.1 and C3.x are needed. The C1.x sensors has no significant influence on the first Principle Component (PC1), which carries the most information (> 90%).

For quantifying CO, CH_4 and their mixtures in varying humidity background linear and non-linear regression methods have been carried out. PCR delivers good results if the humidity background was constant. The prediction error for CH_4 was typically lower than 10%. The prediction error of CO strongly depended on the measurement conditions; it is low for high relative humidities - >30% - and unacceptable for relative humidities below that value. Nevertheless, poor results were obtained for quantification in varying humidity. The uses of non-linear regression methods like Grid and Free (here cluster estimation) Fuzzy Inference Systems lead to better results for mixtures as well as for the single components.

4.3   CMOS micromachined sensors

Results of the newly developed CMOS micromachined sensor measurements are presented in this chapter. During the preparation of this thesis, different design generations of CMOS sensors were tested in respect of sensor performance and stability.

In section 4.3.1, results for temperature stability at varying humidity levels for the micromachined sensors are discussed. With a set of eight sensors, an extensive characterisation was performed (building up a gas database) and in the following results obtained for two representative sensors will be presented. The sensor resistance and the sensor signal of two sensors (one with circuitry and one without) upon exposure of two target gases – CO and methylcyclohexane – are presented as a function of gas concentration, humidity and temperature.

CO was chosen because it is the standard test gas used for characterisation of the sensor performance and therefore comparisons to other sensors are facilitated. As second test gas, typically, a hydrocarbon is used but with methylcyclohexane, a less common representative was chosen. It is found in petroleum and is one main component found in the vapour phase of engine lubricating oils. The data of the other sensors (4 sensors were still working by the end of the measurement run) and gases will be shortly presented by showing temperature performance. The remaining four – Pt III CS1.2B, Pt III L/B, Pt III R/C and Au2is – broke down during the measurements. The reasons have not yet been fully clarified yet but it is indicated that the operation at high temperature lead to failures of the conducting pads.

4.3.1   Temperature stability

The stability of the sensor temperature is shown for 4 sensors in Figure 57, where two sensors – Pt III CS series – are equipped with on-chip electronics for control and regulation of the temperature. In the graph the sensor temperature measured by the temperature sensor placed in the middle of the membrane, is plotted versus the operation time. At day 1 the sensor temperature was adjusted to a temperature of 250°C. The values of the sensor temperature are collected during the purging times before another test gas was measured. The short time period is due to the measurement condition of 0% r.h that last 8 days.
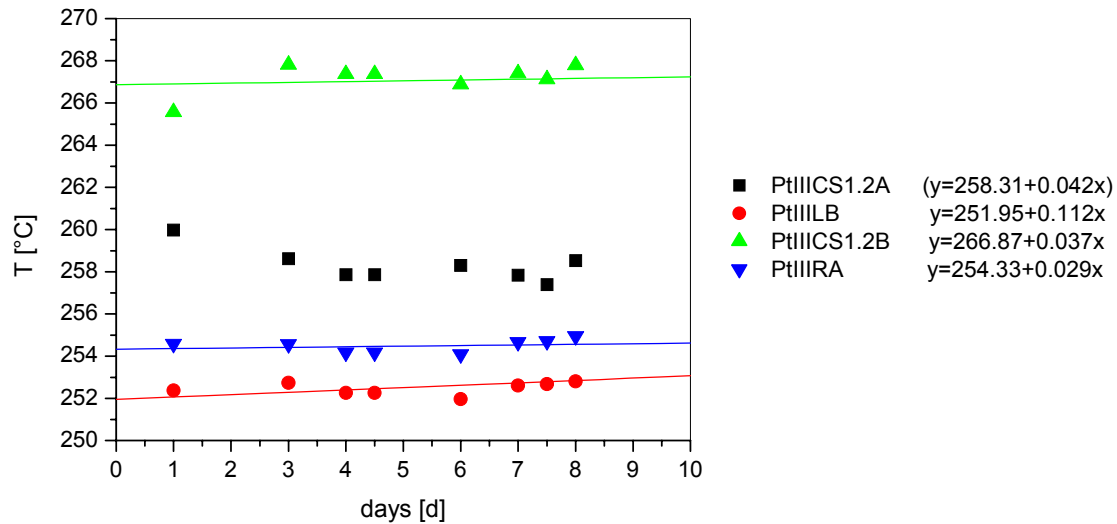
Figure 57: Change of sensor temperature measured by the temperature element in the centre of the membrane with time by applying a constant heating voltage. The data of a linear fit is displayed in the legend for the different sensors. The measurements conditions were 250°C sensor temperature and 0% r.h.

As it can be seen in Figure 57, the thermo voltage and thus the sensor temperature is stable for all sensors over the measurement period. The linear fit of the data over the time shows that there is only a small drift of 0.002% - 0.0043% for the CMOS sensors with temperature control and a temperature increase of 0.004% - 0.010% for the other test structures. The deviations are more likely fluctuations than drift. The data of the CMOS sensor Pt III CS1.2A shows a kind of equilibration/adjustment time typical for first operation condition.

Figure 58 shows the sensor temperature measured in different relative humidities (0, 30 and 50% r.h.). The adjusted sensor temperature was again around 250°C and the exposure to different humidities was performed successively starting with 0% r.h. For a better visualization of differences and similarities, the data are plotted by starting at "day 1" for every applied humidity. The results show that the sensor temperature varies only to a minor degree that is more related to fluctuations than to drift. As a consequence, the temperature element is independent of changing relative humidity and stable over a time period of at least 35 days. This, in fact, result was expected for the CMOS chips with circuitry where the electronics regulates the membrane temperature with the help of a reference voltage.
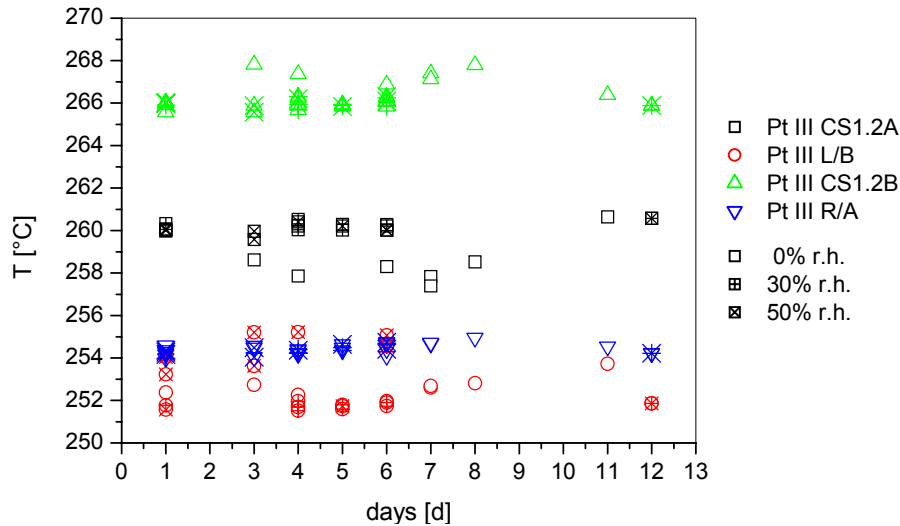
Figure 58: Sensor temperature of the temperature sensor at the centre of the membrane versus the measurement time. Data is shown for a sensor temperature of 250°C in different relative humidities (0 – 50% r.h.), which was recorded successively, but plotted by starting always with day 1 if the humidity was changed.

By exposure to test gases, a small decrease – below 0.5°C - in the sensor temperature could be observed for the test structures; the change is related to sensing. This temperature variation is not present for chips with circuitry because of the temperature control. The additional voltage/current for temperature control of CMOS sensors with circuitry can provide an additional feature for later data evaluation.

4.3.2 Sensor performance

The sensor performance is shown in Figure 59 as a typical example. There, the sensor resistance of all 8 sensors over the time is plotted for different methylcyclohexane (MCH) concentrations ranging from 0 – 100 ppm. The relative humidity was 50% and the sensor temperature 300°C. It can be seen that the sensor response – including the concentration adjustment by the gas mixing system - is quite fast (< 30 s) and the recovery time is sufficiently fast. The gas mixing system and the measurements chambers – equipped with bulky DIL28 socket – have a large death volume. By optimising the set-up, definitely lower values can be reached. There are no visible differences in the sensor response if the purging step is left out.
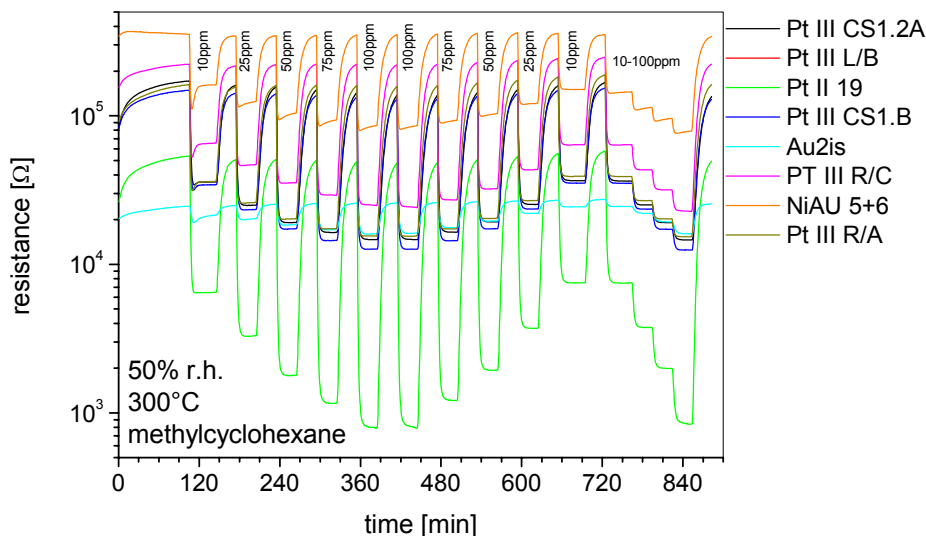
Figure 59: Typical sensor measurement with CMOS sensor. The resistance of the 8 different sensors (2 CMOS sensor with circuitry: Pt III CS1.2A and B and 6 test structures) recorded by applying three cycles of 10 – 100 ppm methylcyclohexane. The sensor temperature was 300°C and the relative humidity 50%.

Other gases like carbon monoxide, methane, octane, propanol, ethylacetate show the same good sensor performance. In the case of toluene and propanal, the response times are comparable but the recovery times are in the range of hours. This long recovery times are due to the period needed to remove these compounds with higher boiling points from the system/sensor surface.

An unexpected sensor behaviour was observed for Au sputtered sensors in the absence of humidity. There, a resistance increase occurs upon the exposure to CO. As it can be seen in Figure 60 the effect increases by increasing the temperature to 300°C. The same effect appears extremely reduced, for the NiAu plated sensor. Nothing similar is reported in literature and no explanation can be given at the moment. For an explanation, additional information will have to be derived from work function measurements and by spectroscopic tools.
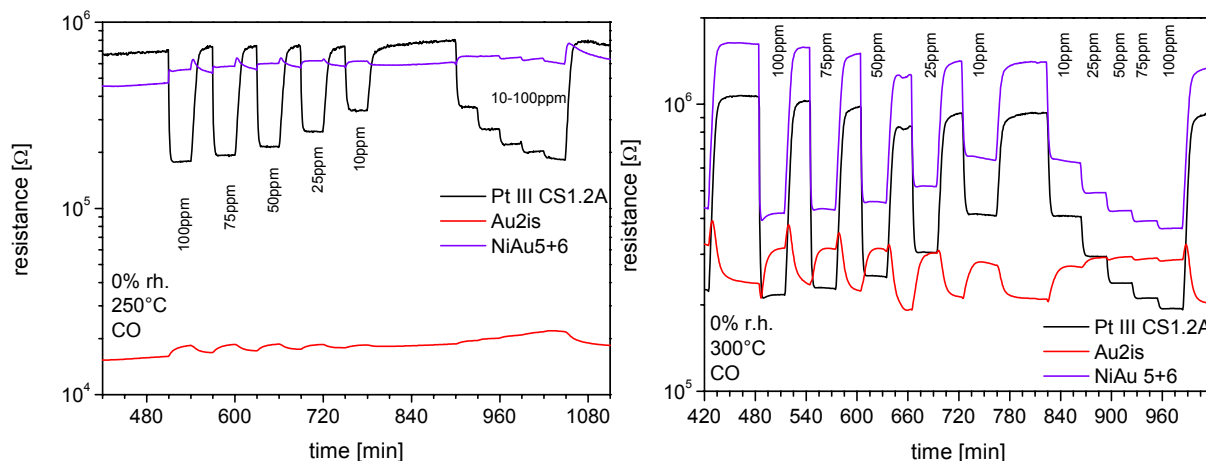
Figure 60: Sensor response of the Au, NiAu and Pt metallized sensors for CO in the absence of humidity at two different sensor temperatures (250°C left side and 300°C right side).

4.3.2.1 Sensor characterisation for selected test gases

In the following, the results of two selected gases – CO and methylcyclohexane (MCH) – are presented for two sensors: Pt III CS1.2A (CMOS chip with circuitry, later referred as CMOS chip) and Pt III R/A (CMOS chip without circuitry, later referred as test structure).

In the following graphs, the mean and the standard deviation out of three measurements are plotted versus the test gas concentration or the sensor temperature.

In Figure 62 - Figure 65 the resistance respectively the sensor signal (R_0 / R) is plotted vs. the CO concentration at different humidities (0, 30 and 50%) and operation temperatures (250°C, 300°C and 350°C). The left part of the graph shows the sensor performance of the CMOS sensor – Pt III CS1.2A – and the right part the results obtained for a test structure – Pt III R/A. Both sensors show a good reproducibility, which is indicated by small standard deviation. As already mentioned in chapter 4.1.4 and 4.2.1 one also observes upon synthetic air exposure for this type of sensor (Figure 61) that:

- The base line sensor resistance decreases with increasing temperatures, because the temperature increases the probability of electrons transfer into the conduction band.

- In the presence of humidity, the sensor resistance decreases in the range of one order of magnitude. This is due to water adsorption in a molecular form or as hydroxyl species [Koh89]. Water acts as electron donor and releases a negative charge to the conduction band.

- With increasing temperature the baseline resistance measured at 0% r.h. decreases stronger than the ones measured in the presence of humidity. In the latter condition, H_2O adsorption determines the conduction and changes in the sensor temperature diminish the temperature dependence.

- At a constant temperature, the sensor base line resistance at different humidities does not differ significantly from each other, which is due to the fact that the maximum adsorption of H_2O is already reached at low humidity values [Kap01]. It can also be seen that the solute values for the different sensors are quite the same – especially at low temperatures-, which point out the good reproducibility of the sensor preparation even if the way in which the sensors were operated was different.
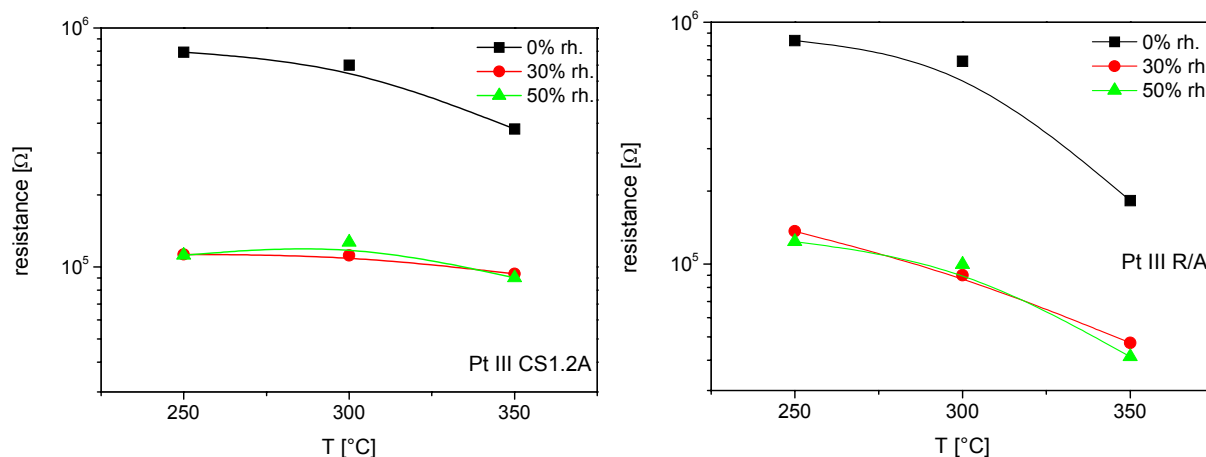
Figure 61: Mean sensor resistance of the baseline of a CMOS chip (left) and a test structure (right) is plotted vs. the different sensor temperatures (250°C, 300°C and 350°C) in the presence of different relative humidities (0%, 30% and 50%).

The results obtained for CO are shown in Figure 62 - Figure 64. Figure 62 and Figure 63 show the sensor resistance/signal dependence upon CO concentration. In Figure 64, the sensor resistance/signal for 50 ppm CO is plotted vs. the different temperatures. Upon CO exposure (0 – 100 ppm) one observes (Figure 62 - Figure 64) that:

- Good reproducibility of the sensors indicated by the low values of the standard deviation (Figure 62 and Figure 63).

- The sensor signal increases with increasing humidity (Figure 63 and Figure 64) because in the presence of H_2O the number of reaction sites and therefore the probability of a CO oxidation to CO_2 is increased (see chapter 2.2.3, [Koh89]).

- The sensor signal decreases with increasing temperature (Figure 64). This is to a large extent observed in the presence of humidity, because the coverage with water-related surface species decreases with increased temperature (as discussed in chapter 2.2.3).

- The differences in the humidity level (30% or 50%) at a constant operation temperature are small especially at low temperatures (Figure 62 and Figure 63). This is observed for the sensor resistance as well as for the sensor signal.

Figure 62: The sensor resistance (mean and standard deviation out of three measurement points) in different relative humidities (0, 30 and 50%) and different temperatures (250°C, 300°C and 350°C) is plotted vs. the CO concentration (0 – 100 ppm). The left side shows the response of a CMOS sensor and a test structure on the right side.

Figure 63: The sensor signal (mean and standard deviation out of three measurement points) in different relative humidities (0, 30 and 50%) and different temperatures (250°C, 300°C and 350°C) is plotted vs. the CO concentration (0 – 100 ppm). The left side shows the response of a CMOS sensor with circuitry and a test structure on the right side.

Figure 64: Temperature dependence of the sensor signal of the CMOS sensor (left) and test structure (right) upon exposure of 50 ppm CO in different relative humidities (0%, 30% and 50%).

The differences of the two types of sensors – temperature controlled or not – are quite small if one compares the sensor performance shown in Figure 63. Some differences are observed in the resistance plots (Figure 62) are can be related to differences in the temperature, which occur upon CO exposure. These differences are enhanced by the sensor signal calculation, where changes in the base line sensor resistance lead to a strong influence.

The results obtained for methylcyclohexane MCH (0 – 100 ppm) are shown in Figure 65 - Figure 69. Figure 65 and Figure 66 show the sensor resistance/signal dependence upon MCH exposure. In Figure 67 and Figure 68, the sensor resistance/signal for 50 ppm MCH is plotted vs. the different temperatures. Upon MCH exposure one observes that:

- The presence of humidity decreases the sensor signal. This is due to a competitive adsorption of H_2O and hydrocarbons (HC) at the same reaction sites on the SnO_2 surface. Therefore, H_2O inhibits to a certain degree the HC interaction with the SnO_2 surface (Figure 66 and Figure 68).

- The differences in the sensor resistance and sensor signal in the presence of a constant humidity level are small for different temperatures (30% or 50% r.h.,). Differences are mainly induced by the value of the baseline resistance (Figure 61, Figure 65 – Figure 68).

- The sensor signal generally increases with increasing temperature (Figure 68). This is clearly observed in the absence of humidity and for the temperature controlled sensor (left side of Figure 66).
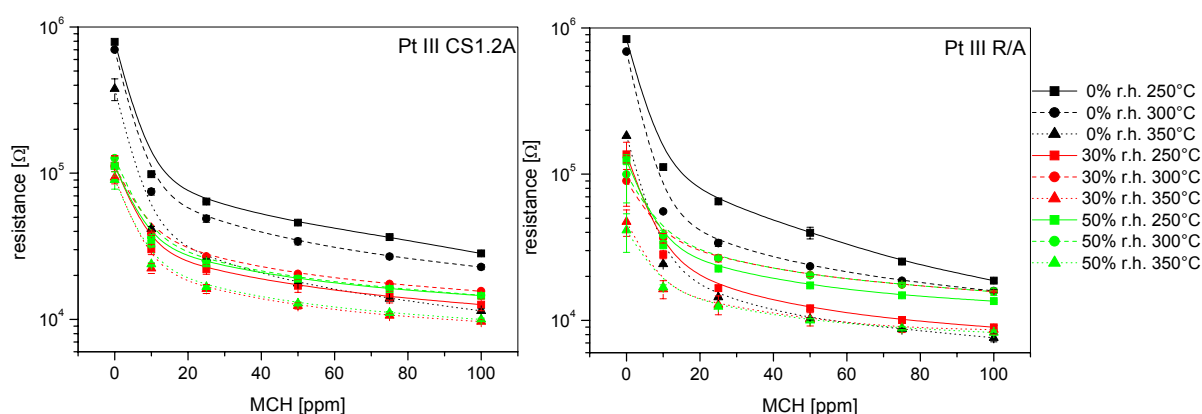
Figure 65: The sensor resistance (mean and standard deviation out of three measurement points) in different relative humidities (0, 30 and 50%) and different temperatures (250°C, 300°C and 350°C) is plotted vs. the methylcyclohexane concentration (0 – 100 ppm). The left side shows the response of a CMOS sensor and a test structure on the right side.
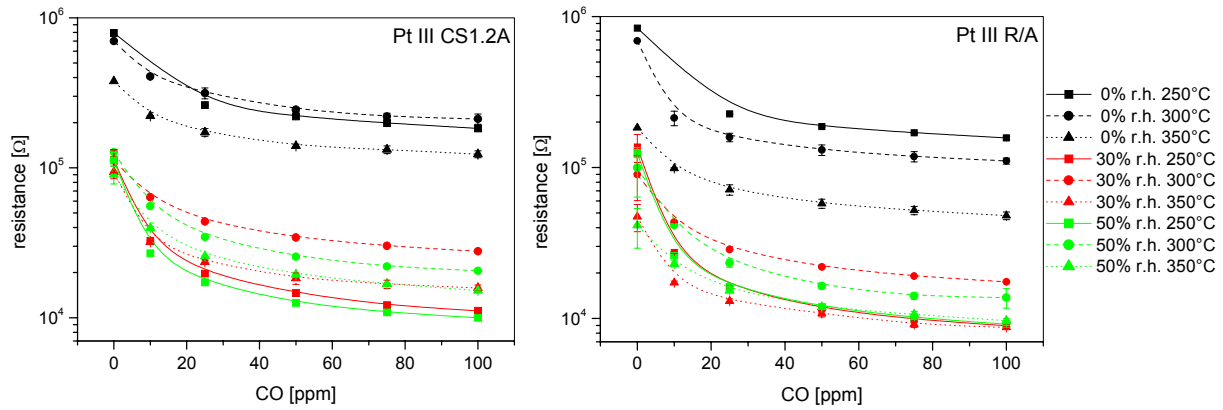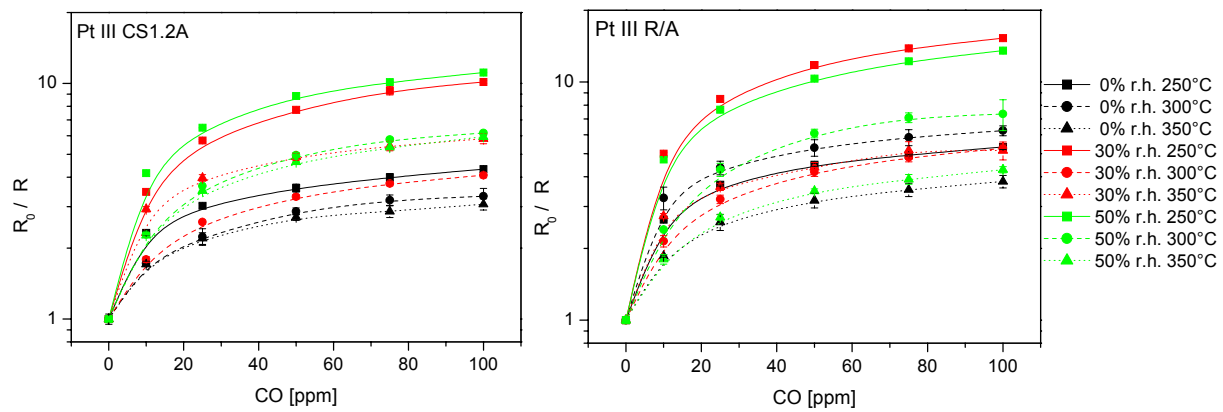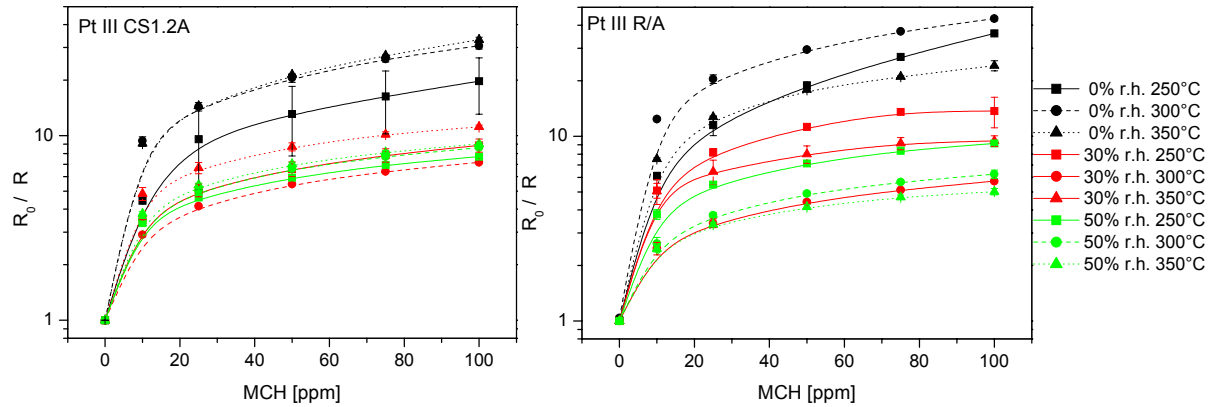
Figure 66: The sensor signal (mean and standard deviation out of three measurement points) in different relative humidities (0, 30 and 50%) and different temperatures (250°C, 300°C and 350°C) is plotted vs. the methylcyclohexane concentration (0 – 100 ppm). The left side shows the response of a CMOS sensor with circuitry (Pt III CS1.2A) and a test structure (Pt III R/A) on the right side.
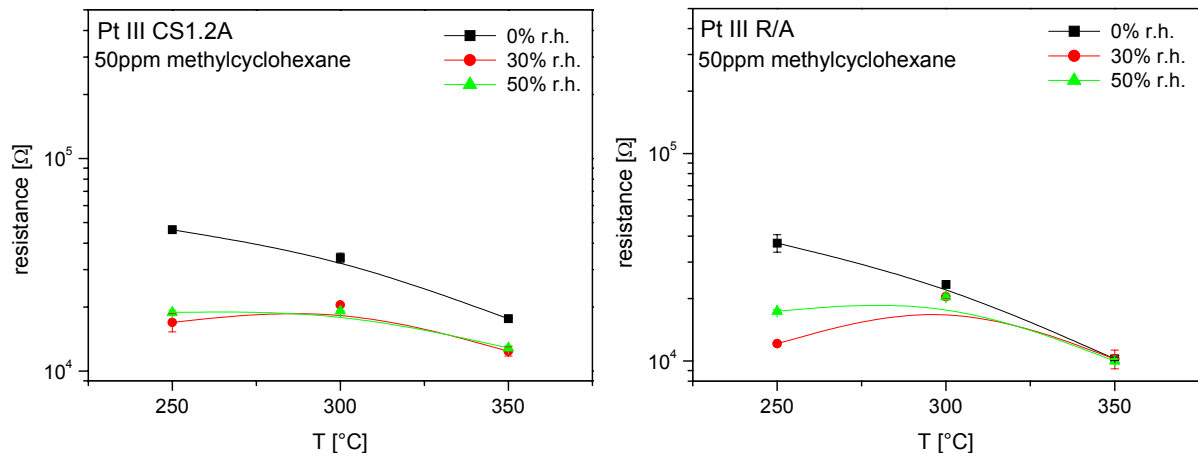
Figure 67: Temperature dependence of the sensor resistance of the CMOS sensor (left) and test structure (right) upon exposure of 50 ppm MCH in different relative humidities (0%, 30% and 50%).
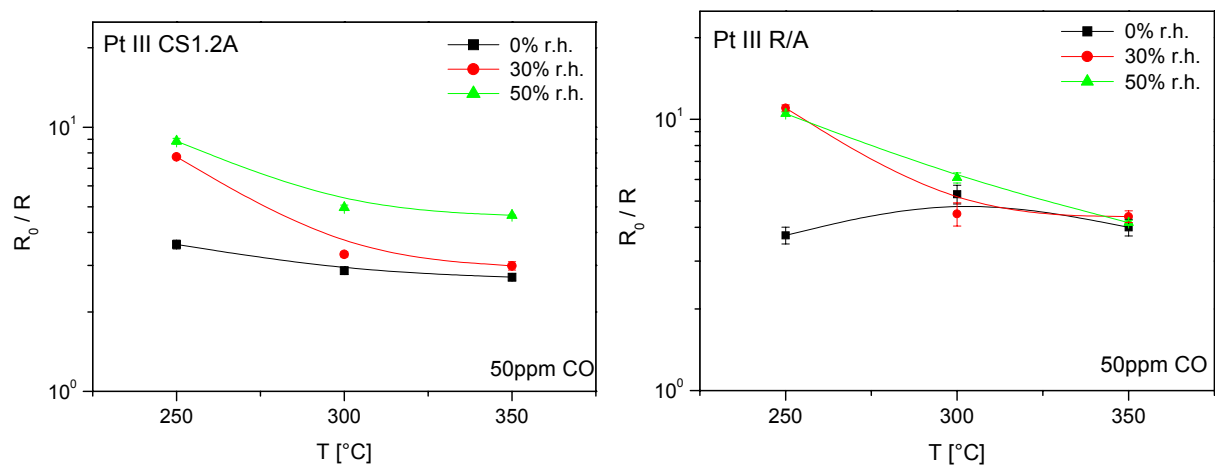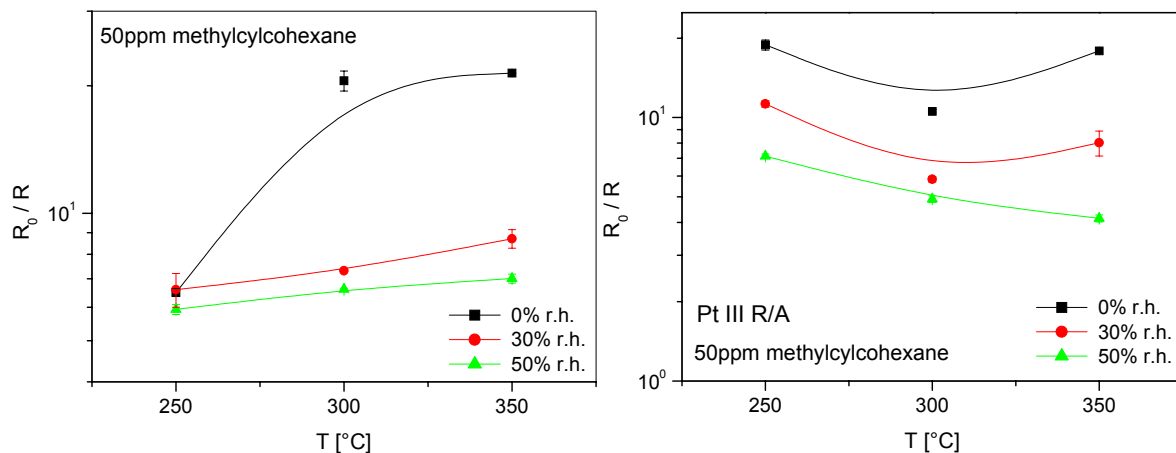

Figure 68: Temperature dependence of the sensor signal of the CMOS sensor (left) and test structure (right) upon exposure of 50 ppm MCH in different relative humidities (0%, 30% and 50%).

In the case of MCH sensing, more differences between the two types of sensor can be observed. There is a larger variation in the sensor resistance for the sensor without temperature control (Pt III R/A, Figure 65 right side). This one is enhanced by the sensor signal calculation, where even small changes in the base line sensor resistance lead to a strong influence. That explains the quite low sensor signal values for 350°C at 0% r.h. (right side of Figure 66) Only for CH_4 sensing, the decrease of the sensor resistance at 350°C is so high it compared to 250°C and 300°C, that the calculated sensor signals have the highest values.

4.3.3 Comparison of all test gases measured by a CMOS sensor

The complete picture of the gas sensing characteristics of the CMOS micromachined sensors is given in Figure 69 for all test gases in the absence of humidity and in Figure 70 for 50% r.h. Examples of the sensor signal measured for the medium test gas concentration - 50 ppm except for propanol (25 ppm) – are plotted vs. sensor temperature ranging from 250°C to 350°C.

Generally, a good sensitivity to all test gases was found. The sensor signals of the compounds containing an oxygen atom are generally higher than for the hydrocarbons. Especially at low temperatures and no humidity, the sensor signal difference is in the range of one order of magnitude. In the absence of humidity, the response to CO is, the lowest. The high values for propanol, propanal and ethylacetate are related to their special chemical structure. They can be bond to the SnO_2 surface via the oxygen atom of the OH, aldehyde, or acetate group and dissociate to form propoxy, formate acetate carboxylate like species [Koh89]. Additionally, they can react according to the hydrocarbon pathway described in chapter 2.2.4. They can be fully decomposed to CO, CO_2 and H_2O, which determines a large resistance decrease because of the consumption of adsorbed oxygen atoms and the generation of adsorbed hydrogen atoms.

With increasing temperature, the sensor signal for propanal, ethylacetate and CO decreases relatively strongly whereas the sensor signal for propanol does not change significantly.

The hydrocarbons also show multifaceted spectra of sensing characteristics. The highest sensor signals are, all the time, obtained for toluene, which is an aromatic hydrocarbon. In the case of the other, the sensor signal decreases with decreasing number of carbon atoms. The lowest values were measured for CH_4, which was expected because highest activation energies are necessary to break the strong C-H bond. With increasing number of carbon atoms and branching of the carbon change the dehydrogenation is facilitated (see chapter 2.2.5). Also, methylcyclohexane posses a tertiary C atom, which has the lowest bonding energies of a linear hydrocarbon. The values of sensor signals are smaller than for octane, probably,

because of the smaller number of hydrogen atoms. Additionally, one has to keep in mind the different molecule structure, which is a ring where more sterically hindrance can occur. The ring structure by itself is energetically more stable.

Toluene reveals the highest sensitivity among the presented hydrocarbons because the aromatic ring stabilizes to a great extend radicals, which are formed by hydrogen separation at the methyl group.
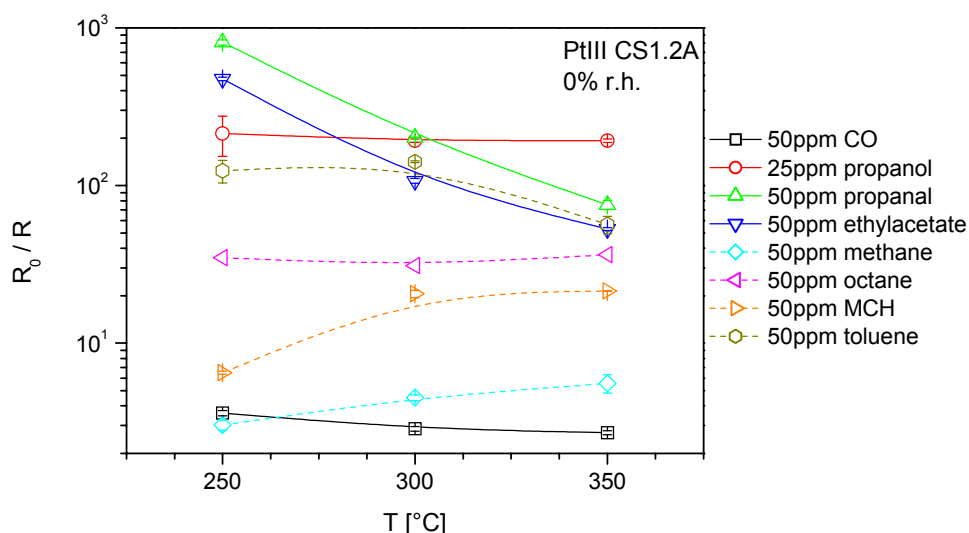
Figure 69: Temperature dependence of the sensor signal of the CMOS sensor Pt III CS1.2A upon exposure to 8 different test gases. The compounds with functional groups are plotted with a straight line and the hydrocarbons with a dashed one. No relative humidity was applied.

The temperature dependence is slightly different for the hydrocarbons. The sensor signals increase with temperature for CH_4 and MCH where more energy is needed for activation. In the case of octane, no dependence on the temperature is visible in this temperature range. For toluene the sensor signal decreases at temperatures around 350°C. This is probably due to a increased desorption of water as it was already mentioned in chapter 4.1.4.

The sensor performance of the CMOS micromachined sensor Pt III CS1.2A in the presence of 50% relative humidity is shown again - by using means the sensor signal - in Figure 70. Nearly for all test gases, the sensor signal decreases in the presence of humidity. For propanal und ethylacetate, it is in the range of one order of magnitude and for the others, only half as much. CO is the only one that shows an increased sensitivity with increasing humidity, which is related to a reaction mechanism involving hydroxyl groups between the gas and water vapour. In the case of the other gases, there is a competition for reaction sites.
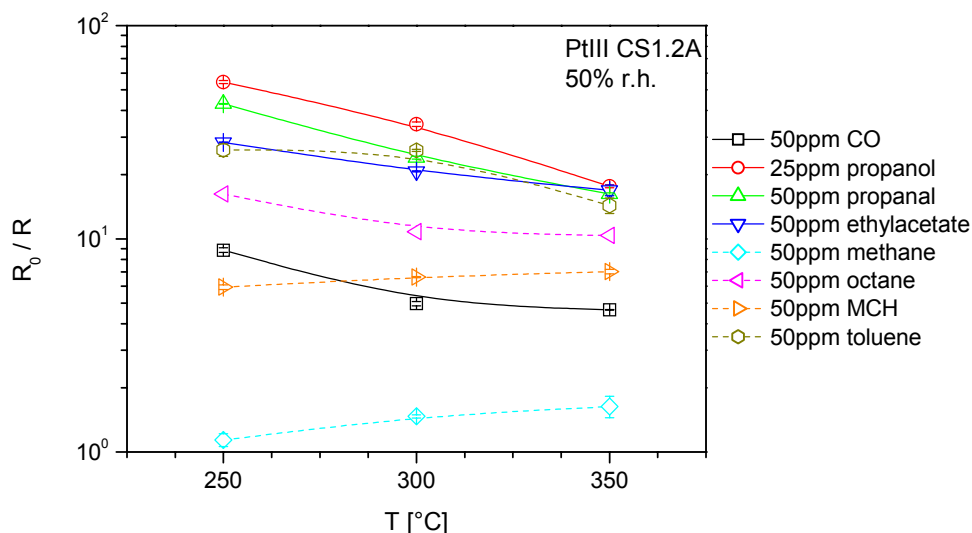
Figure 70: Temperature dependence of the sensor signal of the CMOS sensor Pt III CS1.2A upon exposure to 8 different test gases. The compounds with functional groups are plotted with a straight line and the hydrocarbons with a dashed one. The sensor was measured in background of 50% r.h.

The temperature dependence did not change significantly in the presence of water. Only in the case of propanol, a stronger decrease in the sensor signal is observed than in the absence of water.

4.3.4   Comparison of different CMOS micromachined sensors

In the following, the sensor performance of different sensor generation is compared. In the first section, the characteristics of the sensor used for building the above mentioned gas database are compared, in respect to their temperature dependence, upon CO and methylcyclohexane (MCH) exposure. The second section contains a comparison of all measured CMOS micromachined sensors belonging different design generations.

4.3.4.1   Sensors used for building the gas database

In Figure 71 the temperature dependence of the eight sensors is plotted for 50 ppm CO at 0% and 50% r.h. Some data points are missing, because only four of the sensors were still working at the end of the measurements. Three sensor failures out of the four happened at high temperature operation (350°C) that was closed to the maximum possible temperature of 400°C[1].

In the absence of humidity, one observes different dependencies of the sensor signal. The sensors of the Pt III series (3rd generation) show a small decrease of the sensor signal with

---

[1] The annealing temperature was 400°C. Higher operation temperatures will change the sensor material irreversibly.

increasing temperature. This is typical for CO and was already discussed in detailed in chapter 4.1.4. Different sensing characteristics are observed for the sputtered Au (Au2is) and NiAu plated sensor (NiAu 5+6).

The Au one shows a sensor signal decrease by increasing the temperature followed by an increase by an additional temperature increase of 50°C. The NiAu plated sensor did not show such clearly the effect at low temperature (see Figure 60) but it shows an enhancement of selectivity with increasing temperature. Measurements with newly prepared Au sputtered or NiAu plated sensors will have to show if this effect is reproducible.

In the presence of 50% r.h. (Figure 71 right side), all CMOS micromachined sensors behave more or less in the same way: The sensor signal decreases with increasing humidity. The exception is, again, the sputtered Au sensor.
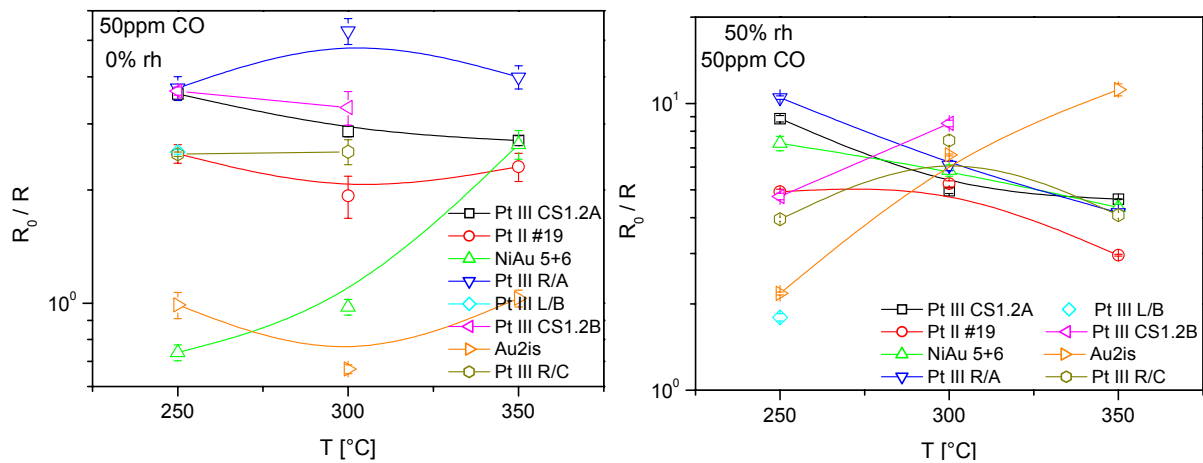
Figure 71: Comparison of the temperature dependence of the different CMOS micromachined sensors. The sensor signal at 50 ppm CO is plotted vs. temperature for 0% r.h. (left) and 50% r.h. (right).

By looking at the same results obtained for MCH sensing one observes in general that all sensors show a higher sensor signal at 0% r.h compared to 30% and 50% r.h (Figure 72 left side). The Pt II #19 shows the highest sensor signals in all conditions but it shows the same qualitative behaviour.

At 50% r.h. (Figure 72 right side), the performance of the individual sensors is different. For most sensors, the sensor signal increases slightly with increasing temperature. The resistance value for Pt II #19 decreases so much that the measurement instrument could not measure it. A small decrease, which was already explained in chapter 4.3.2.1, was also observed for sensor Pt III R/A.
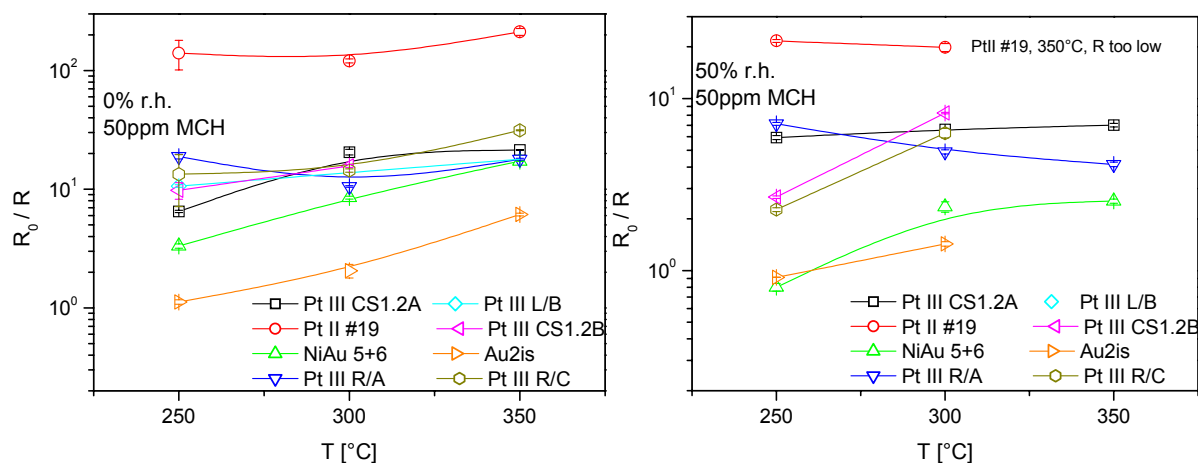
*Figure 72: Comparison of the temperature dependence of the different CMOS micromachined
sensors. The sensor signal at 50 ppm methylcyclohexane is plotted vs. temperature
for 0% r.h. (left) and 50% r.h. (right).*

By looking at the sensor temperature and humidity dependence one observes that in the case
of CO and hydrocarbon (here MCH) sensing both gases could be discriminated by changing
the sensor temperature or the humidity conditions (e.g. different trends of Pt III CS1.2A and
NiAu in the presence of humidity). Applying a multivariate data analysis on the data of all the
sensors would enable discrimination or even a reasonable prediction.

4.3.5 Comparison of different generations of CMOS sensors

In Figure 73 are displayed the sensor signals for 0 – 100 ppm CO for all CMOS
micromachined sensors, which were measured/worked at least 1 month. The left side shows
CMOS micromachined chips with circuitry and the right side test structures (for details in
design see chapter 3.1.2.2). The sensors originate from the following generations:

- 1st generation: Pt5, Rh3, Au2is, Au3
- 2nd generation: Pt 5+6, NiAu3+4, AuII is, Pt II #20, NiAu5+6
- 3rd generation: Pt III CS 1.2A & B

One observes for the CMOS micromachined chips with circuitry that the sensor signals for
the first two generations are quite similar and reproducible. For the 3rd generation the values
are smaller because of a different batch of paste was used for the sensor preparation.
Differences in the choice of the metallization metal were not noticeable.

The variation in the sensor signal for the test structures is bigger. This is due to the different
operation temperature and different sensor designs (meander structure, electrode distance,
etc.) that were significantly varied in the early generations. Especially for the first prepared Pt
sputtered test structures, a peel-off of the Pt layer was observed; that explains the low sensor
signals.
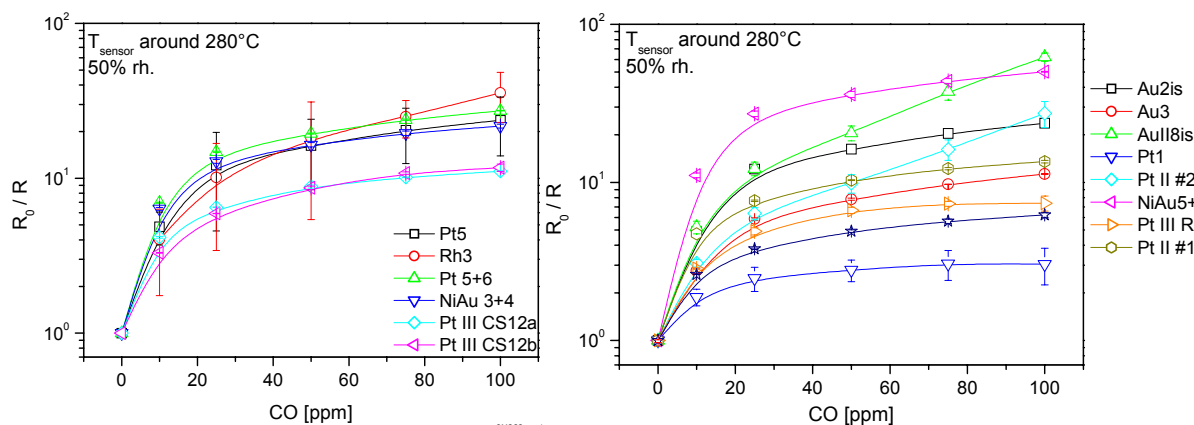
Figure 73: Sensor signal for different CMOSSens chips exposed to 0 – 100 ppm CO. The sensor temperature was around 280°C and they were operated in 50% r.h. The left graph shows CMOSSens chips with circuitry and the right test structures.

4.3.6 Summary

The different CMOS sensors showed good sensitivity to all test gases. The processing of the sensitive layer was performed in an reproducible manner and differences only occurred due to material variation. The 0.2% w.t. Pd doped SnO_2 thick film layer showed especially good sensitivity to polar test gases like propanal, propanal, CO and ethylacetate as well as to higher hydrocarbons like octane, toluene and methylcyclohexane. That is related to the lower activation energy and increased number of the C—H bonds of higher hydrocarbons or to lone pair electrons of oxygen atoms which act as donors.

The Au sputtered or NiAu plated sensors showed reversed signals upon CO exposure in the absence of humidity. If the effect is confirmed for other sensor generations it use will improve the discrimination power of a sensor array.

The hydrocarbons can be easily discriminated from the polar compounds by varying the sensor temperature and humidity. Different sensitive layers with different doping (like Pt) will also improve the discrimination ability and sensitivity towards special gases.

The stability of the temperature sensor of the test structures was quite poor. The temperature sensor of the CMOS micromachined sensor with circuitry, which successfully provides a constant sensor temperature, did not show any failure.

For some CMOS sensors, it was not possible to read out the sensor resistance at the highest operation temperature (350°C). It is suggested that the same problem occurred for the temperature sensors: an overheating could lead to a break in the conducting pads.

5 Summary

Three main topics were investigated within this work: the basic of sensing mechanism of SnO_2 thick film sensor in special conditions; the investigation of the potential of a sensor array based on conventional thick film sensors for the solving of a relevant application and the gas sensing performance of an innovative microsensor system based on a combination of standard CMOS and non-standard post processing technologies.

- It was shown that CO and C_3H_8 sensing is possible even in the presence of very low concentrations of O_2 and H_2O. The sensing characteristics, derived from conductivity measurements depend strongly on the amount of O_2 and H_2O and the kind of sensor doping. Pd and undoped sensors show no qualitative dependence on O_2 concentration for C_3H_8 sensing; only the presence of H_2O decreases the values of the sensor signal for the Pd doped. For C_3H_8, Pt doped sensors show a sensor signal decrease with increasing O_2 concentration. The differences can be related to a differently controlled sensing mechanism (different ratio between spill-over and Fermi level control mechanisms). In the case of CO in the absence of H_2O, a similar O_2 dependency was observed for all sensors: the sensor signal decreases with increasing O_2 concentrations. In the presence of water, the Pd doped sensors show an increased sensitivity if compared to the one measured the absence of H_2O. For Pt doped sensors, the opposite behaviour was found. This indicates that the CO sensing is different for Pd and Pt catalyst in the presence of H_2O. High O_2 and H_2O concentration, in which sensor measurements are usually performed, smoothen the differences.

- The discrimination power of a SnO_2 thick film sensor array consisting of 5 differently doped sensors was evaluated. The target gases were CO and CH_4, individually and combined, in varying humidity background. Conventional methods like PCA showed that a good discrimination of CO and CH_4 was possible at all humidity levels and mixtures. Linear regression methods carried out to determine the test gas concentration showed good results for CO, CH_4 and their mixtures as long as the humidity background did not change. For the case of changing H_2O concentrations, better results were obtained by using non-linear regression methods. With the help of multivariate data analysis the most suitable sensor for the problem could be identified (low concentration of Pd doping) as well as an optimum operation temperature. Reducing the number of sensor without loosing performance will later reduce the instrument size and power consumption.

- A microsensor system realised by a combination of CMOS technology and non-CMOS post processing was characterised from the point of view of gas sensing. The characterisation was performed at different humdities and operation temperatures. Good signals were obtained for the different test gases like CO, propanol, propanal, ethylacetate, methane, methylcyclohexane, octane and toluene. It was proved that the on-chip electronic successfully regulates the membrane temperature of the sensing layer so that no influence of changing humidity, gas exposure and flow was observed. The regulation parameters can also be used as additional feature for subsequent data evaluation methods, because they monitor the gas interaction processes (endothermic or exothermic interactions). The temperature sensors on test structures showed only a poor stability but improvements can be realised without much effort by small changes in the design or a careful choice of supply instruments/electronics. The overall device stability at high temperatures (350°C) still requires improvements.

6 Outlook

The influence of O_2 and H_2O concentration on C_3H_8 and CO sensing was investigated by conductance measurements and it was pointed out that there is a major need for detailed mechanistic studies for improving the sensing characteristics of semiconductor sensor and open up new fields of application. Conductance measurements reflect free electron a transfer related processes and no information is obtained about how the reaction intermediates and educts look like. Measurements with spectroscopic methods like IR related methods combined with MS or XPS, ESR will provide additional information about how the sensing takes place, who are the main reaction partners, in what proportions they occur and how the doping material influences the sensing characteristics. Work function measurements will help to clarify the electronic interaction at the SnO_2 surface and the additional the influence of different dopants on the conductivity mechanism. Impedance measurement will also provide more detailed information about this electronic conductance mechanism.

The discrimination of CO and CH_4 and their mixtures in the presence of humidity is an important application. The methods established here will help to optimize the number of sensors, which leads to a reduction of instrument size and power consumption. If one already think of using the effective sensor coating on CMOS micromachined sensor it is even possible to contemplate batteries driven instruments.

The CMOS micromachined sensor brings good prospects for a lot of new applications because of its low cost, low size and low power consumption. On the basis of the results presented here, the improvement of the on-chip electronics already started. Actually, the operation of microsensors is supported by a board that establish the possibilities of signal processing, self-functioning test, auto-calibration routines, data evaluation etc. The next CMOS microsensor generation will also offer a three sensors array on one chip. The membranes will be coated with differently doped or undoped SnO_2 based sensing layer. At the chip level decreasing the size of the heated membrane, optimizing the electrode geometry covered by the sensitive layer, which will result in a decrease of power consumptions already started.

7 Literature

[ABB]   www.abb.com

[Adv80]   G.N. Advani, A.G. Jordan, Thin Films of SnO_2 as Solid State Gas Sensor, Journal of Electronic Materials, 9 (1980) p. 29-49.

[Air]   http://www.airsens.com

[All93]   F. Allegretti, N. Butta, L. Cinquegrani, S. Pizzini, A tin oxide semiconductor sensor for oxygen determination in the sub-ppm range, Sensors and Actuators B, 10 (1993) p. 191-5.

[Alp]   http://www.alpha-mos.com

[Amb93]   V. Ambrazeviciene, A. Galdikas, S. Grebinskij, A. Mironas, H. Tvardauskas, Sens. Actuators B, 17 (1993) p. 27-33.

[App]   http://www.appliedsensor.com

[Ari97]   K. Ariga, M. Onda, Y. Lvov, T. Kunitake, Alternate layer-by-layer assembly of organic dyes and protesins is facilitated by pre-mixing with linear polyions, Chemistry Letters (1997) p. 25-26

[Bal01]   H. Baltes, O. Brand, CMOS-based microsensors and packaging, Sensors and Actuators A, 92 (2001) p. 1-9.

[Bal99]   H. Baltes, O. Brand (plenary invited paper), CMOS integrated chemical microsensors and the electronic nose, Proc. ESSDERC (1999) p. 29-37.

[Bâr01]   N. Bârsan and U. Weimar, Conduction model of metal oxide gas sensors, Journal of Electroceramics, 7 (2001) p. 143-167.

[Bâr89]   N. Bârsan, R. Grigorovici, R. Ionesc, M. Motronea, A. Vancu, Mechanism of gas detection in polycrystalline thick film SnO_2 sensors, Thin solid films, 171 (1989) p. 53-63.

[Bar93]   M.A. Barteau, Journal of Vacuum Science Technology, 11 (1993) p. 2162

[Bâr93]   N. Bârsan, R. Ionescu, The mechanism of the interaction between CO and a SnO_2 surface: the role of water vapour, Sensors and Actuators B, 61 (1993) p. 71.

[Bâr94]   N. Bârsan, Conduction models in gas-sensing SnO_2 layers: Grain-size effects and ambient atmosphere influence, Sensors and Actuators B, 17 (1994) p. 241.

[Bar97]   P. Barbarat, S.F. Matar, G. Le Blevennec, First-principles investigations of the electronic, optical and chemical bonding properties of SnO_2, Journal of Material Chemistry, **7** (12) (1997) p. 2547-2550.

[Bat75]   G.E. Batley, A. Ekstrom, D.A. Johnson, Studies of topochemical heterogeneous catalysis, J. Catal., 36 (1975) p. 285-290.

[Bau97]   M. Bauer, N. Bârsan, K. Ingrisch, A. Zeppenfeld, I. Denk, B. Schuman, U. Weimar, W. Göpel, Influence of measuring voltage, geometry and electrodes on the characteristics of thick film SnO_2 gas sensors, Proc. of the 11th European Microelectronic Conference, Venice, Italy, May 14-16 (1997).

[Ber96]   F. Berger, E. Beche, R. Berjoan, D. Klein, A. Chambaudet, An XPS and FTIR study of SO_2 adsorption on SnO_2 surfaces, Applied Surface Science, 93 (1996) p. 9.

[Bia75]   D. Bianchi, G.E. Garder, G.M. Pajonk, S.J. Teichner, Hydrogenation of ethylene on alumina after hydrogen spillover, Journal of Catalysis, 38 (1975) p. 135-146.

[Boy77]   J.F. Boyle, K.A. Jones, The effects of carbon monoxide, water vapor and surface temperature on the conductivity of a tin(IV) oxide gas sensor, Journal of Electronic Materials, 6 (6) (1977) p. 717-33.

[Bri00]   D. Briand, A. Krauß, B. van der Schoot, U. Weimar, N. Bârsan, W. Göpel, N.F. de Rooij, Design and fabrication of high-temperature micro-hotplates for drop-coated gas sensors, Sensors and Actuators B, 68 (2000) p. 223-233.

[Bri99]   D. Briand, B. van der Schoot, N.F. de Rooij, High temperature micro-hotplates for drop coated gas sensors, Proceedings of the 13th European Conference on Solid State Transducers, EUROSENSORS XI, The Hague, The Netherlands, September 12-15 (1999) p. 703-704.

[Byt86]   W. Bytyn, M. Baerns, Supported PbO catalysts for the oxidative coupling of methane- the effect of surface acidity of the support on C2+ selectivity, Applied Catalysis, 28 (1986) p. 199-207.

[Cal96]   M. Caldararu, D. Sprinceana, V.T. Popa, N. I.. Ionescu, Surface dynamics in tin dioxide containing catalysts II, Sensors and Actuators B, 30 (1996) p. 35-41.

[Can97]   C. Canevali, N. Chiodini, P. Di Nola, F. Morazzoni, R. Scotti, C.L. Bianchi, Revealed by Electron Paramagnetic Resonance Sprectroscopy, Journal of Material Chemistry, 7 (1997) p. 997-1002.

[Cap01]   S. Capone, Metal oxide based gas sensors for applications in "electronic nose", PhD thesis, University of Lecce, Italy (2001).

[Car00]   G. Carbajal-Franco, A. Tiburcio-Silver, J.M.M. Domínguez, A. Sánchez-Juárez, Thin film tin oxide-base propane gas sensors, Thin solid films, 373 (2000) p. 141-144.

[Car87]   J.A.S.P. Carreiro, M. Baerns, Catalytic conversion of methane by oxidative coupling to C_{2+} hydrocarbons, Reaction Kinetic Catalytic Letters, 35 Iss 1-2 (1987) p. 349-360.

[Cha80]   S.C. Chang, Oxygen chemisorption on tin oxide: Correlation between electrical conductivity and EPR measurements, Journal of Vacuum Science Technology, 17 (1980) p. 366.

[Chi94]   S. Chiu, Fuzzy model identification based on cluster estimation, Journal of Intelligent and Fuzzy Systems, Vol. 2 (1994) p. 267-278.

[Chu 94] I.S. Chuprakov, A.R. Kaul, SnO_2 and Pd/SnO_2 based thin film gas sensors obtained by MO CVD, Conference Proceedings of the 5th International Meeting on Chemical Sensors, Rome (1994) p. 683-686.

[Cit]   http:\\www.citytech.com

[Cli82]   P.K. Clifford, D.T. Tuma, Characteristics of semiconductor gas sensors I: Steady state gas response, Sensors and Actuators, 3 (1982/83) p. 233-254.

[Col91]   G.S.V. Coles, S.E. Bond, G. Williams, Selectivity studies on tin oxide-based semiconductor gas sensors, Sensors Actuators B, 4 (1991) p. 485-491.

[Cox94]   E. Cox, The Fuzzy Systems Handbook, AP Professional 1994, Boston.

[Cox98]   D.E. Cox, T.B. Fryberger, S. Semancik, Oxygen vacancies and defect electronic states on the SnO_2 (110) 1x1 surface, Physical Reviews B, 38 (1998) p. 335-344.

[Dem93]   V. Demarne, A Grisel, Sensors and Actuators B 15-16 (1993) p. 63-67.

[Duk87]   Duk-Dong Lee, Byung-Ki Sohn, Low power thick film carbon monoxide gas sensors, Sensors and Actuators, 12 (4) (1987) p. 441-447.

[Dun79]   I. A. Duncan, A. Harriman, G. Porter, Detection of small quantities of photochemically produced oxygen by reaction with alkaline pyrogallol, Analytical Chemistry, 51 Iss. 13 (1979).

[Ega81]   M. Egashira, M. Nakashima, S. Kawasumi, Change of thermal desorption behaviour of adsorbed oxigen with water coadsoption on Ag+-doped tin(IV) oxide, Journal Chemical Society Chemical Communications (1981) p. 1047-1049.

[Ega81a] M. Egashira, M. Nakashima, S. Kawasumi, T. Selyama, Temperature programmed desorption study of water adsorbed on metal oxides, Journal of Physical Chemistry 85 Iss. 26 (1981) p. 4125-30.

[Ega83]   M. Egashira, M. Nakashima, S. Kawasumi, Influence of coadsorbed water on the reactivity of oxygen adsorbates on noble metal-doped tin(IV) oxides, Conference Proceedings IMCS Fukuika (Japan) (1983).

[Ega87]   M. Egashira, An overview on semiconductor gas sensors, Proceedings of the Electrochemical Society and Proceedings of the Symposium on Chemical Sensors), 87-9 (1987), p. 39-48.

[Ega96]   M. Egashira, Y. Shimizu, Y. Takao, Y. Fukuyama, Hydrogen-sensitive breakdown voltage in the I-V characteristics of tin dioxide based semiconductors, Sensors and Actuators B, 33 (1996) p. 89-95.

[Eja01]   S.G. Ejakov, J. Visser Preliminary Study of Porter/Bronkhorst evaporation systems, Ford internal report 2001.

[Fig]   http://www.figarosensor.com

[Fig00]   Figaro Products Catalogue, Figaro gas sensors 2000-series, Figaro Engineering Inc., European Office, Oststrasse 10, 40211 Düsseldorf, Germany.

[Fig95]   Figaro Engineering Inc.: Figaro gas sensor, Products Catalogue (1995).

[Fis]   http://www.fisinc.co.jp

[FIS99]   FIS, Product list (specifications: Sb/sp series), FIS incorporated, May 1999.

[Fle97]   M. Fleischer, H. Meixner, Fast gas sensors based on Metal oxides which are stable at high temperatures, Sensors and Actuators B, 43 (1997) p. 1-10.

[Fon71]   C.G. Fonstad, R.H. Rediker, Electrical properties of high-quality stannic oxide crystals, Journal of Applied Physics, 42 (1971) p. 2911-2918.

[Fra92]   A.W. Francis (Ed.), Oxygen in McGraw-Hill Encyclopaedia of Science & Tehcnology, Vol. 7, McGraw-Hill, New York 1992, p. 632-635.

[Gai00]   M. Gaidi, H.L. Hazemann, L. Matko, B. Chenevier, M. Rumyantseva, Gaskov, M. Labeau, Role of Pt aggregates in Pt/SnO_2 thin films used as gas sensors - Investigations of the catalytic effect, Journal of the Electrochemical Society, 147 (2000) p. 3131-3138.

[Gal95]   A. Galdikas, A. Mironas, A. Setkus, Copper-doping level effect on sensitivity and selectivity of tin oxide thin-film gas sensor, Sensors and Actuators B, 26-27 (1995) p. 29-32.

[Gen86]   S.J. Gentry, T. A. Jones, The role of catalysis in solid-state gas sensors, Sensors and Actuators 10(1-2) (1986) p. 141-163. .

[Geo65]   P. George, The fitness of oxygen, in Oxidase and related redox systems, T.E. King, H.S. Mason, M. Morrison (Ed.), John Wiley & Sons, New York 1965, p. 3-36.

[Gib94]   J. Giber, I.V. Perczel, J. Gerblinger, U. Lampe and M. Fleischer, Coadsorption and cross sensitivity on high temperature semiconduction metal oxides: water effect on the coadsorption process, Sensors and Actuators B, 18-19 (1994) p. 113-118.

[Gil76]   B. Gillot, C. Fey, D. Dalafosse, Study of the oxidation kinetics of finely-divided magnetites. II. Influence of chromium substitution, Material Research Bulletin, 11 (7) (1976), p. 843-849.

[Glo99]   P.Y. Glorennec, Algorithmes d'apprentissage pout systèmes d'inférence floue, Hermes, Paris (1999).

[GM]   http://www.generalmonitors.com

[Gmi]   http://www.gmiuk.com/

[Gos01]   J. Goschnick, An electronic nose for intelligent consumer products based on a gas analytical gradient microarray, Microelectronic Engineering 57-58 (2001) p. 693-704.

[Gra02]   M. Graf, D. Barrettino, S. Taschini, A. Hierlemann, H. Baltes, S. Hahn, N. Bârsan, U. Weimar, CMOS micro-hotplate with MOS-Transistor heater for integrated metal oxide microsensors, Proceedings of Eurosensors XVI, Prag 2002.

[Gue85]   A. Guest, PhD Thesis, University of Nottingham, (1985).

[Hag99]   C. Hagleitner, A. Koll, R. Vogt, O. Brand, H. Baltes, CMOS capacitive chemical microsystem with active temperature control for discrimination of organic vapors, Technical Digest TRANSDUCERS 2 (1999) p. 1012-1015.

[Hah99]   S. H. Hahn, N. Bârsan, U. Weimar, Impact of different feature extraction methods on signal evaluation of sensors coated with differently doped SnO_2, Proceedings of Eurosensors XIV, Copenhagen, Denmark, August 27-30 (1999) p. 61-62.

[Har85]   P.G. Harrision, B. Maunders, Tin oxide surfaces: Part 16. – Infrared study of the adsorption of formic acid, acrylic acid and acrolein on tin(IV)oxide, tin(IV) oxide-silica and tin(IV)oxide-palladium oxide, Joournal of Chemical Society Faraday TransactinI, 81 (1985) p. 1345-1355.

[Hei88]   G. Heiland and, D. Kohl in T Seiyama (ed.), Chemical Sensor Technology, Vol. 1 Kodansha, Tokyo, p. 1-35.

[Hei97]   A. Heilig, N. Bârsan, U. Weimar, M. Schweizer-Berberich, J. Gardner, W. Göpel, Gas identification by modulating temperatures of SnO_2-based thick film sensors, Sensors and Actuators B, 43 (1997) p. 45-51.

[Hei99]   A. Heilig, Selektivitätssteigerung von SnO_2-Gassensoren, PhD thesis, University of Tübingen (1999).

[Hen94]   V.A. Henrich and P.A. Cox, The Surface Science of Metal Oxides, University Press, Cambridge (1994), p. 312-316.

[Hin84]   W. Hinsen, W. Bytyn, M. Baerns, Oxidative dehydrogenation and coupling of methane, Proceedings of the 8th International Congress of catalysis, Berlin July (1984), Vol. 8 Verlag Chemie, Weinheim, p. 581-592.

[Hoe95]   U. Hoefer, K. Steiner, and E. Wagner, Contact and sheet resistances of SnO_2 thin films from transmission-line model measurements, Sensors and Actuators B 26-27 (1995) p. 59-63.

[Hol95]   A.F. Holleman, E. Wiberg, N. Wiberg, Lehrbuch der anorganischen Chemie, de Gruyter Berlin (1995).

[Hon94] T. Honglin, Z. Yaohua, Y. Zhimei, L. Minqiang, Pd-doped tin(IV) oxide-based thin-film gas sensors, 5th International meeting on chemical sensors, Rome (1994) p. 605.

[Hue89] H.-P. Hübner, E. Obermeier, Reactively sputtered tin oxide thin-film gas sensors: correlation between fabrication parameters and CO-sensitivity, Sensors and Actuators 17 (1989) p. 351-354.

[Ing95] K. Ingrisch et al., Chemical sensors for CO/NO detection in automotive climate control systems, SAE technical paper series, 960692 (1995).

[Ion94] R. Ionescu, A. Vancu, Time-dependence on the conductance of SnO_2:Pt:Sb in atmospheres containing oxygen, carbon monoxide and water vapour I, Applied Surface Science, 74 (1994) p. 297-212.

[Ion99] R. Ionescu, A. Vancu, C. Moise, A. Tomescu, Role of water vapour in the Interaction of SnO_2 Gas Sensors with CO and CH_4, Sensors and Actuators B, 61 (1999) p. 39-42.

[Ipp90] M. Ippomatsu, H. Sazaki, H. Yanagida, Sensing mechanism of tin dioxide gas sensors, Journal of Material Science, 25 (1990) p. 259-262.

[Jae99] M. Jaegle, J. Wöllenstein, T. Meisinger, H. Böttner, G. Müller, T. Becker , C. Bosch-v.Braunmühle, Micromachined Thin film SnO_2 gas sensors in temperature-pulsed operation mode, Sensors and Actuators B, 57 (1999) p. 130-134.

[Jaf49] B. Jaffe, Crucibles: the Story of Chemistry, 3rd ed., Hutchinson's London 1949.

[Jai97] A. Jain, D. Zongker, Feature selection: Evaluation, application and small sample performance, IEEE Transactions on Pattern Analysis and Machine Intelligence, Vol 19, Iss. 2 (1997) p. 153-158.

[Jar87] Z.M. Jarzebski, Physical properties of SnO_2 materials: 1. Preparation and defect structure, Journal of the Electrochemical Society, 123, Iss. 7 (1976) p. 199-205.

[Jol86] J.P. Joly, L. Gonszalez-Cruz, Y. Arnaud, Bulletin de la Société Chimique de France (1986) p. 11-17.

[Kan]   http://www.kane.co.uk/cd100a.htm

[Kap01] J. Kappler, Characterisation of high-performance SnO_2 gas sensors for CO detection by in situ techniques, PhD Thesis University of Tübingen (2001), Shaker Verlag (D) ISBN 3-8365-9040-6.

[Kap99] J. Kappler, N. Bârsan, U. Weimar and W. Göpel, Influence of water vapour on nanocrystalline SnO_2 to monitor CO and CH_4, Conf. Proc. EUROSENSORS XI, Warschau (P) (1999), ISBN 83-908335-0-6, 9/1997, p. 1177-1180.

[Kaw00] T. Kawabe, S. Shimomura, T. Karasuda, K. Tabata, E. Suzuki, Y. Yamaguchi, Photoemission study of dissociately adsorbed methane on a pre-oxidized SnO_2 thin film, Surface Science, 448 (2000) p. 101-107.

[Ker00] N. Kerness, A. Koll, A. Schaufelbühl, C. Hagleitner, A. Hierlemann, O. Brand, H. Baltes, N-well based CMOS calorimetric chemical sensors, Proc. IEEE MEMS (2000) p. 96-101.

[Kim07] J.C. Kim, H.K. Jun, J.-S. Huh, D.D. Lee, Tin oxide-based methane gas sensor propmoted by alumina-supported Pd catalyst, Sensors and Actuators B, 45 (1997) p. 271-277.

[Koe95]   L. Kövér, G. Moretti, Zs. Kovács, R. Sanjinés, I. Cserny, G. Margaritondo, J. Pálinkás, and H. Adachi, High resolution photoemission and Auger parameter studies of electronic structure of tin oxides, Journal of Vacuum Science Technology A 13(3) (1995) p. 382-1388.

[Koh89]   D. Kohl, Surface processes in the detection of reducing gases with SnO_2-based devices, Sensors and Actuators 18 (1989) p. 71-118.

[Koh92]   D. Kohl, Oxidic semiconductor gas sensors, G. Sberveglieri (ed.), Gas sensors, p. 43-88.

[Kol99]   A. Koll, CMOS Capacitive chemical microsystems for volatile organic compounds, PhD Thesis No. 12360, ETH Zurich,Schwitzerland, 1999.

[Lan98]   V. Lantto, T. Rantala, T. Rantala, Experimental and theoretical studies on the receptor and transducer function of SnO_2 gas sensors, presented at SGS' 98 International Seminar (1998) Ustron, Poland.

[Lan99]   D. Lange, C. Hagleitner, O. Brand, H. Baltes, CMOS resonant beam gas sensor with integrated preamplifier, Technical Digest TRANSDUCERS 2 (1999) p. 1020-1023.

[Lee87]   D.D. Lee, B.K. Sohn, Lee, Low power thick film CO gas sensor, Sensors and Actuators, 12 (1987) p. 441-447.

[Lee99]   A.P. Lee, B.J. Reedy, Temperature Modulation in Semiconductor Gas Sensing, Sensors and Actuators B, 60 (1999) p. 35-42.

[Len95]   S. Lenaerts, J. Roggen, G. Macs, FTIR characterization of tin dioxide gas sensors materials under working conditions, Spectorchimica Acta Part A, 51 (1995) p. 883-894.

[Lieb53] O. Liebknecht, W. Katz, S. Kahan, F. Tödt, Handbuch der Analytik: Elemente der sechsten Hauptgruppe I, Springer-Verlag, Berlin 1953, p. 45-93.

[Llo99]   E. Llobet, E.L. Hines, J.W. Gardner, P.N. Bartlett, T.T. Mottram, Fuzzy ARTMAP electronic nose data analysis, Sensors and Actuators B, 61 (1999) p. 183-190.

[Lu00]   F. Lu, Y. Liu, M. Dong, X. Wangs, Nanosized Tin oxide as the novel material with simultaneous detection, Sensors and Actuators B, 66 (2000) p. 225-227.

[Mad97]   A.G. Maddock, Mössbauer spectroscopy, principles and applications, Horwood chemical science series, Chister 1997, ISBN 1-898563-16-0.

[Mae93]   M. Maeda, H. Ishida, K.K.K. Soe, I. Suzuki, Preparation and properties of $PbTiO_3$ films by sol-gel processing, Japanese Journal of Applied Physics Part 1-Regular Papers Short Notes & Review Papers 32 (1993) p. 4136-4140.

[Man86]   B.F.J. Manly, Multivariate statistical analysis, Chappman and Hall, London (1986).

[Mas65]   W.F. Massy, Journal of the American Statistical Association, 60 (1965) p. 234-246.

[Mat88a] S. Matsushima, Y. Teraoka, N. Miura, N. Yamazoe, Electronic interaction between metal additives and tin dioxide-based gas sensors, Japanese Journal of Applied Physics, Vol. 27, No. 10, October (1988) p. 1798-1802.

[Mat88b] Y. Matsuura, K. Takahata, K. Ihokura, Mechanism of gas sensitivity change with time of SnO_2 gas sensors, Sensors and Actuators, 14 (1988) p. 223-232.

[Mat92]   S. Matsushima, T. Maekawa, J. Tamaki, N. Miura, N. Yamazoe, New methods for supporting palladium on a tin oxide gas sensor, Sensors and Actuators B, 9 (1992) p. 71-78.

[May00]   M. Mayer, O. Paul, D. Bolliger, H. Baltes, Intergrated temperature microsensors for characterization and optimization of thermosonic ball bonding process, IEEE trans. Camp. Pack. Technol. 23 (2000) p. 393-398.

[McA87]   J.F. McAleer, P.T. Moseley, J.O.W. Norris and D.E. Wiliams, tin oxide gas sensors Part 1, Journal of the Chemical Society, Faraday Transaction Part 1, 83 (1987) p. 1323-1346.

[Mic]   http://www.microchemical. com

[Miz93]   J. Mizsei, Activating technology of SnO_2 layers by metal particles from ultrathin metal films, Sensors and Actuators, B 15-16 (1993) p. 328-333.

[Mor01]   L. Morris, D.E. Williams, Pt(II) as an electronically active surface site in the room temperature CO response of Pt modified gas sensitive resistors, Journal of Physical Chemistry B, 105 (2001), p. 7272-7279.

[Mor86]   Morrison/Boyd, Lehrbuch der organischen Chemie, 3. Auflage, VCH Weinheim (1986) p. 129.

[Mor87]   S.R. Morrison, Mechanism of semiconductor gas sensor operation, Sensors and Actuators, 11 (1987) p. 283-287.

[Mor90]   S.R. Morrison: The chemical physics of surfaces, 2nd (edn.), Plenum Press, New York (1990).

[Mos00]   T. Moser, F. Stanglmeier, B. Schumann, S. Thiemann-Handler, Sensor in planarer Dickschichttechnik zur Messung von Kohlenwasserstoffen im Abgas von Kraftfahrzeugen, VDI-Berichte. 1530 (2000) p. 159–167.

[Mun87]   S. Munnix, M. Schmeits, Electronic structure of tin dioxide surfacws, Physical Review B, 27 (1987) p. 7624-7635.

[Nag99]   Y. Nagasawa, T. Choso, T. Karasuda, S. Shimomura, F. Ouyang, K. Tabata, Y. Yamaguchi, Photoemission study of the interaction of a reduced thin film SnO2 with oxygen, Surface Science 433 (1999) p. 226-229.

[Nan82]   L. Nanis, G. Advani, Effect of sorbed oxygen on tin oxide conduction, Journal of electronic Materials, 52 (4) (1982) p. 345-349.

[Opi88]   N. Opitz, H.J. Graf, D.W. Luebbers, Oxygen sensor for the temperature range 300 to 500 K based on fluorescence quenching of indicator-treated silicone rubber membranes, Sensors and Actuators, 13(2) (1988) p. 159-63.

[Ott86]   M. Otto, Chemometrics Intell. Lab. Syst. 1 (1986) p. 71.

[Pad94]   P. De Padova, M. Fanfoni, R. Larciprete, M. Mangiantini, S. Priori, and P. Perfetti, A synchroton radiation photoemission study of the oxidation of tin, Surface Science, 313 (1994) p. 379-391.

[Pin80]   H. Pink, L. Treitinger, L. Vite, Preparation of fast detecting SnO_2 gas sensors, Japanese Journal of Applied Physics, 19 (1980) p. 513-517.

[Pri]   www.romgaz.com/English/esm1279.htm

[Rkt]   http://www.rkiinstruments.com/pages/eagle.htm

[Rob67]   J.J. Robillard, Electrocatalytic photographic process, patent (GB) 1063029 (1967).

[Rob84] J. Robertson, Defect levels of SnO_2, Physical Reviews B, 30 (1984) p. 13520-3522.

[Röm95] Römpp Chemilexikon, ed. 1995.

[Ron00] L. Rong, W. Ping, H. Wenlei, A novel method of wine analysis based on sensor fusion technique, Sensors and Actuators B 66 (2000) p. 246-250.

[Rts] http://www.rts-rostock.de

[Saf02] O. Safonova, I. Bezverkhy, P. Fabrichnyi, M. Rumyantseva and A. Gaskov, Mechanism of sensing CO in nitrogen by nanocrystalline SnO_2 and SnO_2 (Pd) studied by Mössbauer spectroscopy and conductance measurements, Journal of Materials Chemistry, 12 (2002) p. 1174-1178.

[Sam73] S. Samson, C.G. Fonstad, Defects structures and electronic donor levels in stannic oxide crystals, Journal of Applied Physics, 44 (1973) p. 4618-4621.

[San71] K.M. Sancier, Hydrogen migration on alumina/palladium catalysts for benzene hydrogenation, Journal of Catalysis, 20 (1971) p. 106-109.

[Sbe91] G. Sberveglieri, S. Groppelli, P. Nelli, A. Camanzi, A new technique for the preparation of highly sensitive hydrogen sensors based on SnO2 (Bi2O3) thin films, Sensors and Actuators B 5 (1991) p. 253-255.

[Sbe93] G. Sberveglieri, S. Groppelli, P. Nelli, C. Perego, G. Valdre, A. Camanzi, Detection of sub-ppm H_2S concentrations by means of SnO_2(Pt) thin films, grown by the RGTO technique, Sensors and Actuators B, 15-16 (1993) p. 86-9.

[Sch77] C.W. Scheele, Chemische Abhandlung von Luft und Feuer 1777.

[Sch98] M. Schweizer-Berberich, Gas sensors based on stannic oxide, PhD Thesis, University of Tübingen (1998), Shaker Verlag (D), ISBN 3-8265-4182-0.

[Scha01] A. Schaufelbühl, N. Schneeberger, U. Münch, M. Waelti, O. Paul, O. Brand, H. Baltes, C. Menolfi, Q. Huang, M. Loepfe, E. Loering, Uncooled low-cost thermal imager based on micromachined CMOS integrated sensor array, IEEE Journal of Microelectromechanical Systems 10 (2001) p. 503-510.

[Schi91] K.D. Schierbaum, U. Weimar, W. Göpel, Conductance, work function and catalytic activity of SnO_2 based gas sensors, Sensors and Actuators B, 3 (1991) p. 205-214.

[Sem01] S. Semancik, R.E. Cavicchi, M.C. Wheeler, J.E. Tiffany, G.E. Poirier, R.M. Walton, J.S. Suehle, B. Panchapakesan, D.L. DeVoe, Surface state trapping models for SnO_2-based microhotplate sensors, Sensors and Actuators B, 77 (2001) p. 579-591.

[Ser73] P.A. Sermon and G.C. Bond, Hydrogen Spillover, Catalysis Review, 8 (1973) p. 211-239.

[Sey62] T. Seiyama, A. Kato, K. Fujisishi, M. Nagatoni, A new detector for gaseous components using semiconductive thin film, Analytical Chemistry, 34 (1962) p. 1052-1052.

[Sim01] I. Simon, N. Bârsan, M. Bauer, Udo Weimar, Micromachined metal oxide gas sensors: Opportunities to improve sensor performance, Sensors and Actuators B, 73 (2001) p. 1-26.

[Som99 P. Somol, P. Pudil, J. Novovicová and P. Paclík , Adaptive floating search methods in feature selection, Pattern Recognition Letters, Volume 20, Issues 11-13, November (1999) p. 1157-1163.

[Sta74]   D. Staschewski, The stable Isotopes of oxygen in research and technical applications, Angewandte Chemie Industrie Edition, 13 (1974) p. 357-370.

[Ste25]   W. Steuer, Chemische Zeitung, 49 (1925) p. 713.

[Str83]   S. Strässler, A. Reis, Simple models for n-type metal oxide gas sensors, Sensors and Actuators, 4 (1983) p. 465-472.

[Sue93]   J. Suehle, R. Cavicchi, M. Gaitan, S. Semancik, Tin oxide gas sensor fabricated using CMOS micro-hotplates and in situ processing, IEEE, Electron. Dev. Letts. 12 (3) (1993) p. 118-120.

[Sun02]   T. Sundic, S. Marco, A. Perera, A. Pardo, S. Hahn, N. Bârsan, U. Weimar, Fuzzy Inference System for sensor array calibration: Prediction of CO and CH_4 levels in variable humidity condition, Chemometrics and Intelligent Laboratory Systems, in press.

[Tag62]   N. Taguchi, Japanese Patent 45-38200 (1962).

[Tag70]   N. Taguchi, UK patent 1280809 and US patent 3631436 (1970).

[Tak85]   T. Takagi, M. Sugeno, Fuzzy identification of systems and its application to modelling and control, IEEE Trans. Syst. Man. Cyber, 15 (1985) p. 116-132.

[The]   http://www.gastech-inc.com/scripts/shopplus.cgi?DN=gastech-inc.com&CARTID=%CARTID%&FILE=/portable/innova.htm

[The92]   J.M. Themlin, M. Chtaïb, L. Henrard, Ph. Lambin, J. Darville, J.M. Gilles, Characterization of tin oxides by x-ray-photoemission spectroscopy, Physical Review B, 46 (4) (1992) p. 2460-2466.

[Tho75]   E.W. Thornton, P.G. Harrison, Tin oxide surfaces Part I: Surface hydroxyl groups and the chemisorption of carbon dioxide and carbon monoxide on tin(IV)oxide, Journal of the Chemical Society, Faraday Transaction I, 71 (1975) p. 461-472.

[Tok]   http://www.tokyo-gas.co.jp/techno/stp/97d2_e.html

[Tou99]   G. Tournier, C. Pijolat, Influence of oxygen concentration in the carrier gas on the response of tin dioxide sensor under hydrogen and methane, Sensors and Actuators B, 61 (1999) p. 43-50.

[Tsa95]   P.P. Tsai, I.-C. Chen, M.H. Tzeng, Tin oxide (SnOx) carbon monoxide sensor fabricated by thick-film methods, Sensors and Actuators B, 24-25 (1995) p. 537-539.

[Udr01]   F. Udrea, J.W. Gardner, D. Setiadi, J.A. Covington, T. Dogaru, C.C. Lua, W.I. Milne, Design and simulations of SOICMOS micro-hotplate gas sensors, Sensors and Actuators B, 8 Iss 1-3 (2001) p. 180-190.

[UST99]   UST, Product information, Umweltsensortechnik GmbH, Gewerbegebiet Geschwenda Süd Nr. 3, D-98716 Geschwenda, 1999.

[Vin01]   D. Vincenzi, M.A. Butturi, V. Guidi, M.C. Carotta, G. Martinelli, V. Guarnieri, S. Brida, B. Margesin, F. Giacomozzi, M. Zen, G.U. Pignatel, A.A. Vasiliev, A.V. Pisliakov, Development of a low-power thick-film gas sensor deposited by screen-printing technique onto a micromachined hotplate, Sensors and Actuators B, 77 Iss 1-2 (2001) p. 95-99.

[Vla93]   D.S. Vlachos, P.D. Skafidas, J. N. Avaritsiotis, Transient effects of tin oxide CO sensors in the presence of water vapour, Applied Physics Letters, 63 (1999) p. 39-42.

[Voh86]   J.M. Vohs, M.A. Barteau, Conversion of methanol, formaldehyde and formic acid on the polar faces of zinc oxide, Surface Science, 176 (1986) p. 91-114.

[Vol81]   A.M. Volodin, A.E. Cherkasin, ESR studies of nitrous oxide interaction with photoinduced centers on zinc oxide and magnesium oxide, Reaction Kinetic Catalytic Letters, 17 (1981) p. 221-224.

[Wan00]   J. Wang, Analytical electrochemistry, Wiley-VCH Maine, USA (2000), p. 87.

[War]   http://www.warensortiment.de/messtechnik/messgeraete/gasdetektoren.htm

[Wei53]   P.B. Weisz, Effects of electronic charge transfer between adsorbate and solid on chemisorption and catalysis, Journal of Chemical Physics, 21 (1953) p. 1531-1538.

[Wei01]   U. Weimar, Gas Sensing with Tin Oxide: Elementary Steps and Signal Transduction, Habilitation thesis, Tübingen 2001.

[Wie97]   P.R. Wiederhold, Water vapor measurements: Methods and instrumentation, New York (1997).

[Wil91]   M.J. Willett, Spectroscopy of surface reactions, in P.T. Moseley, J. Norris, D.E. Williamjs, Techniques and mechanisms in gas sensing, vol. 3, Adam Hilger, Bristol (1991) p. 61.

[Wil99]   M.J. Willet, N.V. Burganos, C. Tsakiroglou, A.C. Pyatakes, Gas Sensing and structural properties of variously pretreated nanopowder, Sensors and Actuators B, 53 Iss. 1-2 (1999) p. 76-90.

[Win79]   H. Windischmann, P. Mar, A model for operation of thin-film SnO_x conductance modulation carbon monoxide sensor, Journal of electrochemical Society: Solid-State Science Technology, 126 (1979) p. 627-633.

[Xu91]   C. Xu, J. Tamaki, N. Miura, N. Yamazoe, Grain size effects on gas sensitivity of porous SnO_2-based elements, Sensors and Actuators B, 3 (1991) p. 147-155.

[Yam79]   N. Yamazoe, J. Fuchigami, M. Kishikawa, T. Seiyama, Interactions of tin oxide surface with O_2, H_2O and H_2, Surface Science, 86 (1979) p. 335-344.

[Yam91]   N. Yamazoe, New approaches for improving semiconductor gas sensors, Sensors and Actuators B, 5 (1991) p. 7-19.

[Yea99]   B. Yea, T. Osaki, K. Sugahara, R. Konishi, Sensors and Actuators B, 56 (1999) p. 181-188.

[Yoo95]   K. H. Yoon, D. J. Nam, Photoelectrochemical behaviour of SnO_2 thin-film electrodes prepared by ultrasonic spray pyrolysis, Journal of Materials Science, 30 (1995) p. 3415-3420.

8   Appendix

8.1   Review of oxygen and water detection

In the field of semiconductor sensor investigation and application, oxygen and water play important roles. Generally, O_2 is combusted and H_2O influences the selectivity and sensitivity of the material. The adsorption species of H_2O, e.g. hydroxyl groups, can additionally serve as reaction partners. Monitoring the O_2 and H_2O concentration can help to identify the sensing mechanism of the applied test gas. Their initial concentration in air determines the number of adsorbed species and their kind the reaction mechanism.

There is a great variety of oxygen measurement instruments based on different detection methods. At the beginning, the chemical properties of oxygen respectively water are mentioned shortly, which are used for detection. A small number of different instruments are mentioned later.

8.1.1   Oxygen detection

8.1.1.1   Properties of oxygen (O_2)

Oxygen is the most abundant element in the Earth's crust (approximately 49.5% by weight). It is believed that Carl Wilhelm Scheele, a Swedish pharmacist, discovers O_2 first around 1774. He observed that heating silver carbonate produced a gas which would support respiration [Sch1777]. The name "oxygen", meaning acid-former, was given by Antoine Laurent Lavoisier, who believed at that time that all acids contained oxygen [Jaf49]. Oxygen, in the form of dioxygen, is widely used in industry in the production of: steel and other metals, the manufacture of chemicals, rocket propulsion, the production of stone- and glass containing products [Fra92], etc. Oxygen is also one of the most important elements in biology because the reactions of dioxygen provide the principal thermodynamic driving force for the metabolism of all higher organisms [Geo65].

The most abundant form of elemental oxygen is the gaseous diatomic molecule O_2 (properly called "dioxygen" but primarily called "oxygen"), which accounts for approximately 21% by volume of dry air. The oxygen atoms in the atmosphere are composed of three isotopes: oxygen-16 (^{16}O), which makes up 99,750%, oxygen-17 (^{17}O), 0.037% and oxygen-18 (^{18}O), 0.204% [Sta74].

To understand the chemical reactivity of oxygen, it is necessary to discuss first the electronic configuration of oxygen. It ground state electronic (term symbol $^3\Sigma_g^-$) configuration is $1s^2\ 2s^2$

$2p^4$. From Hunds "maximum multiplicity, minimum energy" rule the state of maximum multiplicity lies lowest in energy. Therefore, the ground state molecular oxygen will have a bond order of two and be a triplet state (3S). The next two states in order of increasing energy are singlet oxygen ($^1\Delta_g$) and $^1\Sigma_g^+$.
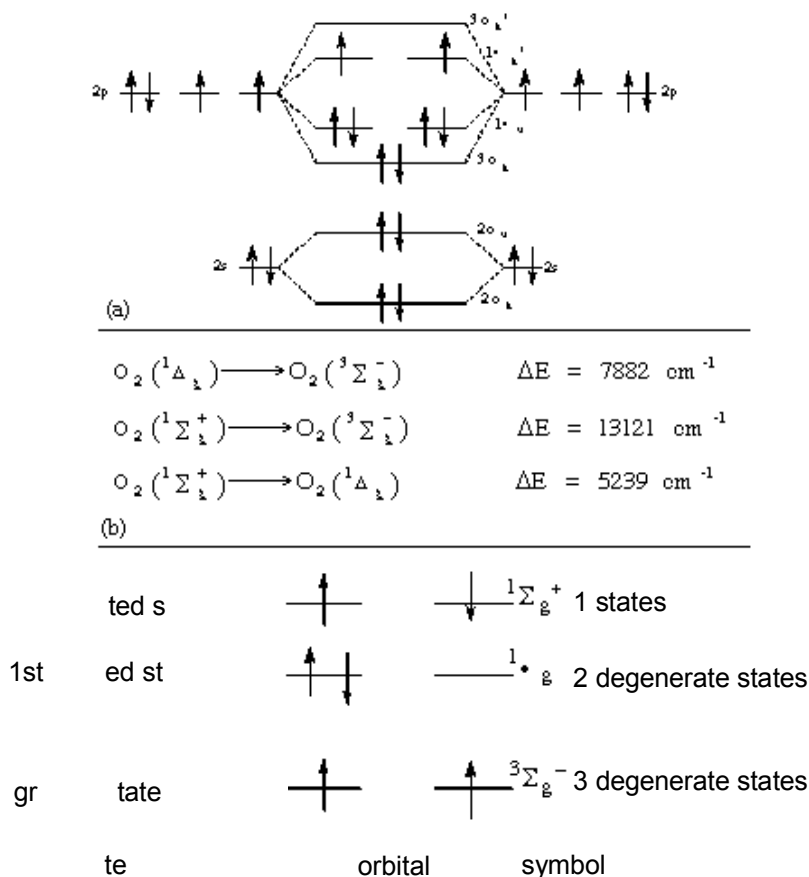
Figure 74: Electronic configuration of molecular oxygen showing:
(a) Molecular orbital diagram for ground state (3S);
(b) Energy difference for each of the energy levels.

8.1.2 Detection instruments

There are a variety of different methods to detect gaseous O_2:

- Gas volumetric methods: O_2 is adsorbed on special adsorbents like pyrogallol, ammoniacal copper(I) saline solution, etc. which results in a volume decrease [Lie53].

- Combustion methods: e.g. mixture with H_2 (detonation gas), which forms H_2O [Ste25].

- Calorimetric methods: oxidation of a dye by bubbling oxygen through a solution of indigo carmine, pyrogallol, copper(I) saline solutions, etc.

- Physical and physical-chemical methods

The first three methods are based on the chemical properties of O_2 but they cannot be used for online measurements. Therefore, the following methods based on physical properties are mostly used O_2 measurements:

- Magnetic susceptibility

- Heat conductivity

- Thermal methods

- Electrochemical methods: polarography, EMF (ElectroMotive Force) of galvanic cells and amperometric measurements

- Optical methods

- Semiconductor materials/sensors

They will be mentioned shortly in the following.

By measuring the *magnetic susceptibility,* one makes use of the paramagnetic properties of oxygen [Hol95]. The instrument works as follows: A heating filament in an inhomogeneous magnetic field produces a temperature gradient. In this magnetic field arises additionally a thermal convection because of a magnetic wind. This magnetic wind is a gas flow caused by the paramagnetic oxygen molecules. The cold gas is stronger driven in the magnetic field due to its higher density resulting in higher susceptibility than the heated gas, whose susceptibility decrease with the square of the temperature (law of Curie). The strength of the magnetic wind and the resulting temperature decrease of the heating filament are proportional to the oxygen concentration. A Wheatstone bridge measures the resistance change of the heating filament. Interfering gases are components with a noteworthy paramagnetic susceptibility like NO, NO_2, ClO_2 and ClO_3. They can cause an error up to 0.02% in a measurement range of 1% O_2. An advantage of this detection principle is the small number of interfering gases, which are hardly present in typical applications of gas sensors. Because of this, a paramagnetic oxygen analysator was chosen in the later experiments for referencing the oxygen concentration.

The oxygen concentration can be determined by changes in *heat conductivity* of a gas. Therefore, a platinum wire is heated with constant current and the resistance is measured which increase by decreasing heat conductivity of the gas [Lie53].

In the case of *thermal methods,* catalysts convert the gas mixture and a thermo couple measures the resulting reaction heat.

There are a number of *electrochemical methods* to determine the O_2 in gases. Polarography provides a limiting diffusion current that is proportional to the concentration. Thus, the solubility of oxygen in an electrolyte is determined. Under the terms of the Henry law, the

concentration of oxygen solved in the electrolyte is proportional to the concentration in the gaseous phase.

A well-known and million times used electrochemical O_2 sensor is the λ-probe whose working principle is based on an *electrochemical cell*. The λ-probe is a *potentiometric* sensor operated at high temperatures. It is used in the automotive industry for controlling the ratio of air/fuel. It consists of an Y_2O_3-doped ZrO_2 disk with porous platinum electrodes. The measurement is based on the coupling of an oxygen reduction process and the preferential transport of the oxide ion product through vacancies in the doped crystal. For this purpose, one of the platinum electrodes is exposed to the unknown gas while the second one is exposed to the reference gas.

Another important oxygen probe is based on *amperometric* measurements. The sensor consists of a pair of electrodes immersed in an electrolyte solution that is separated from the test solution by a gas-permeable hydrophobic membrane (Clark et al. [Cla62]). The membrane is usually made of Teflon, silicon rubber, or polyethylene, while the electrolyte is a solution of potassium chloride and buffer [Wan00]. Oxygen diffuses through the membrane and is reduced at the surface of the sensing electrode. The resulting electrolytic current is proportional to the rate of oxygen diffusion to the cathode, and hence to the partial pressure of oxygen in the sample. Such an electrode displays a linear response in contrast to the logarithmic dependence of most gas sensors.

One kind of an optical *oxygen sensor* is based on the detection of *fluorescence quenching* of a metal organic fluorescent dye solved in a hydrophobic polymer mixture [Opi88]. Often used fluorescent reagents for oxygen detection are porphyrin complexes, which can be excited by green and yellow light emitting diodes (LEDs). Its fluorescence can be detected with inexpensive Si photodiodes. The intensity of the fluorescence signal of the dye will decrease, if the signal is quenched by the presence of molecular oxygen. The relation as well as the recovery time of the fluorescence in the absence (I_0, t_0) and the presence (I, t) of oxygen can be described by the Stern-Volmer-Equation (equation 16). KSV as the Stern-Vollmer constant, which includes a lifetime dependent term of the excited state:

$$\frac{I_0}{I} = \frac{t_0}{t} = 1 + KSV[O_2] \qquad\qquad (34)$$

Specific control of the dye to optimise the resolution and sensitivity can be achieved using alternate electrostatic charge self-assembly [Ari97].

A type of *semiconductor sensor* used for O_2 detection is based on a ZnO thin film. The sensor resistance increase with increasing O_2 concentration and regeneration is done by heating. Zircon is mostly found four-valent and builds with oxygen an electrical neutral lattice. By doping the zircon oxide with e.g. yttrium, one obtains a corresponding number of oxygen vacancies. With the help of these vacancies, the oxygen can migrate as soon as a slope of oxygen partial pressure is drawn.

8.1.3 Water detection

One faces main problem in gas sensor applications: the semiconductor sensors are quite sensitive to changing water vapour concentration or more commonly called humidity. Because of this, the gas sensor performance has to be tested in different humidities to find an appropriate material or operation parameters where changing humidity does not influence the quality of the sensor response. Therefore, the influence of humidity is still a point of investigation and up to now it is not completely understood how water influences the sensing mechanisms of different gases. In this thesis, the humidity was monitored online in some measurements in regard of identifying the role of water in the sensing mechanism.

In this chapter, the properties of water a briefly mentioned and afterwards a short summary is given about the different types of hygrometers.

8.1.3.1 Properties of water (H_2O)

About 71% of the earth's surface is covered by water but its stake in the first 16 km of the earth's crust is small. The outstanding characteristic of H_2O is the higher volume of its solid state of aggregation compared to the liquid one that enables the survival of numerous species. This anomaly is attributed to its molecular structure that is determined by the different electro-neutrality values of oxygen and hydrogen atoms resulting in high polar bonding [Hol95]. This polar bonding leads to intramolecular hydrogen bond that increases the density of water. It is also responsible for the good solubility behaviour.

Its usage is manifold. Water serves as food, detergent, solvent, cooling agent, heat transfer, winning of energy, irrigation, means of transport, etc. [Röm95]

8.1.4 Humidity detection instruments

In 1450, Nicolas Cryfts described the first hygroscope: "If someone should hang a good deal of wool, tied together on one end of a large pair of scales, and should balance it with stones at the other end in a place where the air is temperate, it would be found the weight of the wool would increase when the air becomes more humid, and decrease when the air tends to

dryness". The device was improved by Leonardo da Vinci in his Codes Atlanticus, substituting a sponge for the wool [Wie97].

Despite the increase in research and development activities in the past time to improve humidity sensors, the present state of the art is still such that humidity measurements require more care, more maintenance, and more calibration than other analytical measurements. Furthermore, there is no sensor available that can even come close to cover the full dynamic range of water vapour levels. For this reason, many different measurements methods and sensors have been developed through the years. Each having certain advantages and limitations and suit for some, but not all, applications.

The number of humidity detection instruments is big and depend on different measurement principles. Some of them are listed in Table 13. The different instrumentation advantages the whole variety of chemical and physical/electrical properties.

Table 13: A selection of humidity detection instruments (hygrometers) and their detection principle. For a detailed description see [Wie97] and the references therein.

| Instrument	Measurement principle
Chilled mirror hygrometers	Determination of the dewpoint
Displacement (mechanical) Hygrometers	Strain gauge, expansion/contraction measurement
Bulk polymer humidity sensor: • Resistive polymer sensor • Capacitive polymer sensor	Hygroscopic macro polymer • Resistance measurement. • Capacitance measurement
Ceramic humidity sensors: • Aluminum oxide hygrometers • Silicon oxide hygrometers • Impedance-based ceramic sensors	• Capacitance measurement • Capacitance/Impedance measurement • Impedance measurement of ion conductors
Piezoelectric sensor	Vibration frequency change of a hygroscopically-sensitive quartz crystal
Electrolytic hygrometer	Water electrolysis
Optical absorption hygrometers • Infrared hygrometer • Lyman-alpha hygrometer	Adsorption in the IR range Adsorption in the UV range
Saturated salt ($LiCl_2$) sensor	Dew point based on equilibrium in $LiCL_2$ salt
Fog Chamber	Adiabatically cooling
Colour change	E.g. cobalt chloride

Acoustic	Transmission of sound air
Dry/wet-bulb psychrometer	Thermal

In the following, the two main detection principle will be introduced. First the chilled mirror hygrometer which have the advantage of selectivity but expensive in cost and second different sensor principles which stand out for low cost but have a partly low selectivity.

8.1.4.1 Chilled mirror hygrometer

The chilled mirror hygrometer, sometimes called optical condensation hygrometer, is the most accurate, reliable, and fundamental hygrometer commercially available. It is therefore widely used as a calibration standard. The chilled mirror hygrometer measures the dew/frost point of a gaseous component. The dew point is detected by cooling a reflective condensation surface (mirror) until water begins to condense. The condensed fine water droplets are detected optically by an electro-optic detection system (see Figure 75). The signal is fed into an electronic feed back control system to control the mirror temperature, which maintains a certain thickness of dew at all times.
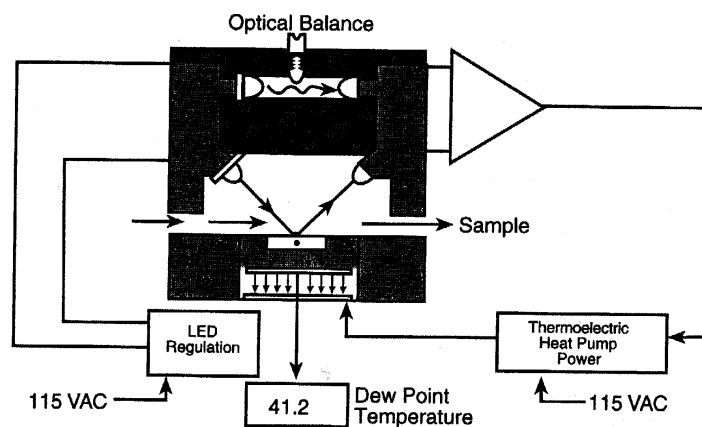
Figure 75: Operation of the basic optical dew point hygrometer. The surface temperature of a small gold or rhodium-plated copper mirror is controlled by a thermoelectric cooler (heat pump). A high intensity light-emitting diode (LED) illuminates the mirror. A phototransistor or optical detector detects the quantity of reflected light from the mirror surface.

The dew point measurement range of a chilled mirror sensor is dependent on the type of Peltier cooler, the mode of operation, the gases to be monitored, and the ambient or sensor body temperature.

The advantages of the chilled mirror hygrometers are that it measures the absolute humidity. It can be made very compact by using solid-state optics and thermoelectric cooling, and offer many capabilities using microprocessors.

The disadvantages are that it is more expensive than most other types, and requires maintenance by skilled personnel, monitoring, and care of installation (such providing a proper sample flow, cleaning of the mirror, etc.). The largest source of error in a condensation hygrometer is the difficulty of accurately measuring the condensation surface temperature (0.1°C – 1°C). However, the condensation hygrometer is a fundamental instrument; it cannot distinguish between water vapour and other gaseous vapours. When the mirror is cooled, in most cases it is water vapour which is the first to saturate and condense on the mirror surface, and it is usually assumed that the instrument will sense and control on water or ice.

8.1.4.2 Sensors

The *bulk polymer sensors* are now the most advanced humidity sensors on the market. They consist of a miniature electrode base plate coated with a hygroscopic macro polymer. An electrical grid structure is vapour deposited upon the element and an electrical measurement is made which is a function of the relative humidity. The two most popular polymer sensors are the bulk resistance and the bulk capacitive sensors, depending on whether the sensor is designed for a change of resistance or change of capacitance measurement. The used polymers and manufacturing techniques are different for resistive and capacitive sensors. The sensors have somewhat different characteristics with advantages and limitations. One of the advantages is that by the use of different polymers, sensitivity to contaminants for resistive and capacitive sensors is different, i.e., some cause greater adverse effects on resistive sensors while others affect capacitive sensors more. Hence, the type of contaminants that are present often dictates the choice of sensor.

In a typical *resistive (polymer) sensor*, the sensitive material is prepared by polymerising a solution of quaternary ammonium bases and subsequent reaction of its functional base with a polymer resin. This produces a three-dimensional thermosetting resin, which is characterised by its excellent stability in extreme conditions. Humidity is measured by the change in resistance between anode and cathode. If the electrodes contain quaternary ammonium salt, mobile ion changes are created in the presence of humidity and one can measure a change in the ion conductivity. A Wheatstone bridge using the variation in impedance caused by the cell measures the movement of such ions.

The *capacitive (polymer) sensors* use either polyamide or cellulose acetate polymer thin films (film thickness typically 1 to 10 μm) deposits between conductive electrodes. The film, acting as a dielectric capacitor with interjected surface metal as electrodes, changes its dielectric constant as moisture is adsorbed or desorbed by the thin film. Because of the high permittivity

of water molecules ($\varepsilon = 81$), the sensor is less influenced by interfering atmospheric gases. An alternative construction design uses a porous top metal layer that allows moisture transmittance.

The advantages of a bulk resistance sensor are a fast response (but slower than capacitive sensors), virtually no hysteresis or aging, low temperature constant, stable and repeatable operation in many applications, inexpensive and low power consumption. The capacitive sensors show a better linearity and hence higher accuracy in the low r.h. range (minimum 2%, resistance polymer sensor 15%). It can be also used in higher ambient temperatures up to 185°C.

The limitations include that it is a secondary measurement device which must be periodically re-calibrated. It is not suitable in the presence of certain contaminants, it needs temperature compensation if used over a brad temperature range, modes temperature and humidity range.

The first widely used *ceramic humidity sensor* was the aluminium oxide sensor. The aluminium is oxidised anodically in an acidic solution to form a porous oxide film, sometimes less than 1 µm thick that displays the necessary hygroscopicity. Adsorption of water molecules causes a decrease in resistance and an increase in capacitance, which is reversed by subsequent desorption. Other materials are also used in humidity sensors, including ZnO, V_2O_5, colloidal Fe_3O_4, α-Fe_2O_3, mixed oxides of TiO_2 and SnO_2, $MgCr_2O_4$-TiO_2, TiO_2-$V_{32}O_5$, $ZnCr_2O_4$-$LiZnVO_4$, $MgAl_2O_3$, $MgFe_2O_4$, or H_3PO_4-$ZrSiO_{32}$, as well as $PbCrO_4$ with added alkali oxide [Wie97]. Sometimes the signal of such a sensor is subject to drift because of changes in the surface structure or contamination of other adsorbed gases. Nevertheless, heat cleaning can restore reproducibility.

To ensure adequate sensitivity and response, a sensor of this type should consist of a very thin film of porous ceramic with a porosity > 30%. The contacting electrodes may be interdigitated or porous sandwich-type structures made from noble metals (e.g., Pd, Pt, Au) and so constructed that they do not obstruct the pores of the oxide film. Humidity affects not only the resistance of a porous ceramic but also its capacitance by extending the surface area in contact with the electrodes.

Aluminum oxide is also used for another type of a ceramic sensor in essence as a capacitor, formed by depositing a layer of porous aluminum oxide of a conductive substrate, and then coating the oxide with a thin film of gold. The conductive base and the gold layer become the capacitor's electrodes, forming what is essentially an aluminum oxide capacitor. Water vapour penetrates the gold layer and is adsorbed by the porous oxide layer. The number of

water molecules absorbed determines the electrical impedance of the capacitor, which, in turn, is proportional to water vapour pressure. Aluminum oxide sensors are also suitable for measurements of water vapour in organic liquids. The pore wall openings are small compared to the size of organic molecules. Therefore admission into the pore cavity is limited to small molecules such as water.

The aluminum oxide sensors are free from interferences by gases, such as hydrocarbons, carbon dioxide and carbon monoxide, although the drift rate may vary for differing gases. Certain corrosive gases, such as ammonia, sulphur trioxide vapour, and chlorine, attack the sensing element and should be avoided.

The determing advantage of aluminum oxide sensors is the wide dynamic range form 1 ppm to 80% r.h.

Silicon oxide hygrometers use capacitive impedance type sensors that are in many ways similar to aluminum oxide sensors, but they employ silicon rather than aluminum as the humidity sensitive material. They have faster response than aluminium oxide, but they are more expensive.

The *piezoelectric sensor* measures moisture by monitoring the vibration frequency change of a hygroscopically-sensitive quartz crystal that is exposed alternatively to wet and dry gas. The sensitivity of a piezoelectric sensor can be affected by several variables including, cell pressure, cell temperature, coated polymer area, electronics, sample cycle.

List of publications

In chronological order:

1. S. Hahn, M. Frank, U. Weimar, Rancidity investigation on olive oil: A comparison of Multiple Headspace Analysis using an Electronic Nose and GC/MS; Proceedings of ISOEN 2000 Brighton (UK) (7/2000).

2. M. Frank, S. Hahn, P. Visani, N. Barsan, U. Weimar, Long-term investigations on sensor arrays: The necessity of re-calibrationConf. Proc. ISOEN 2000, Brighton (UK) (7/2000) p. 61-62.

3. S.H. Hahn, N. Bârsan, U. Weimar, Impact of different feature extraction methods on signal evaluation of sensors coated with differently doped SnO_2, Sensors and Actuators B78 (2001) p. 64-68.

4. S. Strathmann, S. Hahn, U. Weimar, "Food Investigation by an Electronic Nose with differential thermal desorption and GC-MS" Artificial Chemical Sensing: Proceedings of the eighth international symposium on olfaction and electronic nose (ISOEN 2001), edited by J.R. Stetter, W.R. Penrose, published by The Electrochemical Society, Inc, Pennington, New Jersey, USA, ISBN 1-56677-321-0 p 65-75.

In press:

5. D. Barrettino, M. Graf, Zimmermann, A. Hierlemann, H. Baltes, S. Hahn, N. Bârsan, U. Weimar, A smart single-chip microhotplate-based chemical sensor system in CMOS, accepted for ISCAS 200s2 (conferences on circuitry), paper number 2206.

6. M. Graf, D. Barrettino, M. Zimmermann, A. Hierlemann, H. Baltes, S. Hahn, N. Bârsan and U. Weimar, CMOS Single-Chip Metal Gas Sensing System Based on Microhotplates, Conference Proceedings IMCS Boston 2002.

7. S. H. Hahn, N. Bârsan and U. Weimar, Sally G. Ejakov, Jacobus H. Visser and Richard E. Soltis, Gas sensor measurements in low oxygen concentrations and high humidity, Conference Proceedings IMCS Boston 2002, paper number 248.

8. S. H. Hahn, Nicolae Bârsan, Udo Weimar, Sally G. Ejakov, Jacobus H. Visser and Richard E. Soltis "Oxygen and water interactions at the surface of SnO_2 based sensors, Conference Proceedings Eurosensors, Prague 2002

9. M. Graf, D. Barrettino, S. Taschini, A. Hierlemann, Henry Baltes, <u>S. Hahn</u>, N. Bârsan and U. Weimar, CMOS Micro-Hotplate with MOS-Transistor Heater for Integrated Metal Oxide Microsensors, Conference Proceedings Eurosensors, Prague 2002.

10. D. Barretino, M. Graf, M. Zimmermann, A. Hierlemann, H. Baltes, <u>S. Hahn</u>, N. Bârsan and U. Weimar "A system architecture of Micro-Hotplate-Bases Chemical Sensors in CMOS-Technology, Conference Proceedings Eurosensors, Prague 2002.

11. T. Sundic, S. Marco, A. Perera, A. Pardo, <u>S. Hahn</u>, N. Bârsan, U. Weimar, Fuzzy Inference System for sensor array calibration: Prediction of CO and CH_4 levels in variable humidity condition Chemometrics and Intelligent Laboratory Systems, in press.

Submitted:

12. R. Tauler, A. Pardo, T. Sundic, <u>S. Hahn</u> and S. Marco, Chemical sensing using electronic noses and chemometrics submitted to Biosensors and Biolectronics.

13. <u>S. H. Hahn</u>, N. Bârsan, U. Weimar, S.G. Ejakov, J.H. Visser and R.E. Soltis "Oxygen and water interactions at the surface of SnO_2 based sensors, submitted to Semiconductor Gas Sensors (SGS), Sep. 2002, Ustron, Poland.

Meine akademischen Lehrer waren:

K. Albert, E. Bayer, D. Christen, H. Eckstein. G. Gauglitz,F. Gönnenwein, W. Göpel, P. Grathwohl, G. Häfelinger, M. Hanack, V. Hoffmann, W. Jäger, G. Jung, S. Kemmler-Sack, W. Koch, B. Koppenhöfer, K.-A. Kovar, D. Krug, N. Kuhn, H. Liebich, E. Lindner, M.E. Mayer, H.-J. Meyer, U. Nagel, H. Oberhammer, D. Oelkrug, H. Pauschmann, H. Pommer, G. Reinhardt, V. Schurig, F.F. Seelig, B. Speiser, H. Stegmann, J. Strähle, W. Voelter, K.-P. Zeller, C. Ziegler.

Lebenslauf

Simone Hildegard Hahn

geboren am

25. Juni 1974

in Alzey/Rheinhessen

Schulbildung

1980- 1984	Grund-und Hauptschule Flonheim
1984 – 1993	Elisabeth-Langgässer-Gymnasium Alzey
1993	Abitur

Studium

Okt. 93- Aug. 99	Immatrikulation an der Eberhard-Karls-Universität in Tübingen im Fach Chemie-Diplom
Apr. 95	Abschluss der Diplomvorprüfungen
Feb. 99	Diplomhauptprüfungen
Feb. 99 – Aug. 99	Diplomarbeit im Arbeitskreis von Prof. Dr. W. Göpel mit Thema „Methoden zur Evaluierung der Qualität von Speiseölproben: Instrumentelle Analytik im Vergleich mit Sensorsystemen"
Apr. 99 – Jul. 01	Teilnahme am Graduiertenkolleg der DFG „Quantitative Analyse und Charakterisierung pharmazeutisch und biochemisch relevanter Substanzen".
Sep. 99 – Jul. 02	Anfertigung der Dissertation mit dem Thema: "SnO_2 thick film sensors at ultimate limits: Performance at low O_2 and H_2O concentrations; size reduction by CMOS technology" unter Anleitung von Privatdozent Dr. U. Weimar am Institut für Physikalische und Theoretische Chemie der Universität Tübingen.

Tübingen, den 3. Juli 2002